Numerical Modeling of the Metal Cutting Process in the Plasma Arc Cutting

A DISSERTATION
SUBMITTED TO THE FACULTY OF
UNIVERSITY OF MINNESOTA
BY

Hunkwan Park

IN PARTIAL FULFILLMENT OF THE REQUIREMENTS
FOR THE DEGREE OF
DOCTOR OF PHILOSOPHY

Dr. Emil Pfender and Dr. Terrence W. Simon, Advisers

November, 2015

Acknowledgements

First of all, I would like to express my sincere gratitude to the late Professor Joachim V.R. Heberlein for giving me the opportunity to work on this project and for his guidance and inspiration. I have a deep appreciation for his contributions to this work and to the plasma processing field in general. I would also like to thank my advisers, Professor Emil Pfender and Professor Terrence W. Simon, for their support and guidance after Professor Heberlein's absence.

Also, I am very grateful to David Osterhouse for his guidance and assistance in developing and debugging the plasma cutting process model code.

I would furthermore like to thank Professor Vaughan R. Voller, Professor Sean Garrick, and Professor Peter J. Bruggeman for serving on the committee and for their valuable comments. My thanks also go to John Lindsay, Yu Zhang, Soumya Mitra, and other employees of Hypertherm Inc. for valuable suggestions and discussions for this work.

I wish to thank my research colleagues and friends at the University of Minnesota for their friendship and help during the course of my Ph.D.

The financial support of this work was provided by Hypertherm Inc., and this work was carried out using computational resources from the University of Minnesota Supercomputing Institute (MSI).

Finally, I wish to express my deepest gratitude to my parents for their endless support during my entire life.

Abstract

The process of cutting metal with a plasma arc cutting tool is investigated and discussed. Focus is on the metal cutting process at the inside surface of the kerf. This is an important region that is not well documented due to the difficulty of experiments and the complexity of computation needed to characterize this process. In the present work, a three-dimensional numerical simulation using a plasma model combined with a melting process model is conducted and results are discussed, leading to a better understanding of the physical phenomena within the kerf region of a commercial plasma arc cutting tool. The modeling includes three different phenomena: 1) the plasma jet flow, 2) the Volume of Fluid (VoF) method in identify the gas to molten metal interface, and 3) the phase change model for computing the melting process. The model is implemented in the open source CFD software, OpenFOAM. Thermodynamic and transport properties, calculated by kinetic theory of gases and statistical mechanics, are implemented for accurate simulation in the high temperature regions. The simulation results show the transient cutting process including the physical phenomena for melting of the work piece as well as the plasma flow. The simulated kerf shape is compared to measured kerf under same operations. Additionally, the temperature, velocity, and current density distributions are discussed to understand the plasma characteristics during the cutting process. In an attempt to make a more reasonable kerf shape, the swirl component of the jet, the surface tension and the phase change model are investigated for improvement and discussed. Effects of metal vapor and oxidation reaction are also discussed. This work is a first attempt simulation of the plasma flow, melting, and molten metal flow in the plasma arc cutting process. As the model approaches physical reality, it gives increasingly useful insight into the relationships among operating conditions, providing very helpful directions to improve performance, and providing useful data for designing the plasma arc cutting process.

Table of Contents

List of Tables

List of Figures

Nomenclature

Name	Description
$\vec{A}$	Magnetic potential [Tm]
A	Sparse matrix
$\vec{B}$	Self-induced magnetic field [T]
b	Array of source terms
C_D	Large constant value
c	Constant for the width of the profile
D_{O_2}	Mass flow rate [kg/s]
e	Charge of an electron, $e = 1.6022 \times 10^{-19}$ [C]
$\vec{E}$	Electric field [V/m]
F	Flow direction
F_p	Darcy force [N]
F_s	Surface tension force [N]
h	Specific enthalpy [J/kg]
ΔH	Heat of reaction for $2\text{Fe}+\text{O}_2 \rightarrow 2\text{FeO}$, $\Delta H = 549.2$ [kJ/mol]
$I_{b\eta}$	Black body intensity
$\vec{j}$	Current density [A/m^2]
j_0	Maximum current density at the center of the cathode [A/m^2]
k_b	Boltzmann constant, $k_b = 1.381 \times 10^{-23}$ [J/K]
k_η	Absorption coefficient
L	Latent heat of fusion [kJ/kg]
m_i	Mass of species i [kg]
m_e	Mass of electrons [kg]

M_{O_2}	Molar mass of oxygen [g/mol]
n_i	Number density of species i [1/m^3]
p	Pressure [Pa]
$\vec{q}$	Diffusive heat flux [W/m^2]
$\dot{Q}_{eh}$	Energy transfer from the electrons to the heavy particles [W/m^3]
$\dot{Q}_{melt}$	Amount of energy transfer to the melt [W]
$\dot{Q}_{oxy}$	Total power released from oxidation [W]
$\dot{Q}_r$	Radiation heat loss [W/m^3]
R	Radius of the hafnium insert [m]
R_{eff}	Effective radius of the net emission coefficient model [m]
S_p	Surrounding surface of V_p [m^2]
$S_\varphi(\varphi)$	Source term [W/m^3]
T	Temperature [K]
T_l	Solidus temperature [K]
T_s	Liquidus temperature [K]
T_m	Mean value of the solidus and liquidus temperature $(T_s + T_l)/2$ [K]
$\vec{u}$	Velocity [m/s]
U_c	Cutting speed [m/s]
u_{axial}	Axial velocity for the gas inlet boundary [m/s]
u_{radial}	Radial velocity for the gas inlet boundary [m/s]
V_p	Control volume [m^3]

Greek symbols

α	Metal phase(melt, solid metal)
γ	Liquid phase
Γ	Diffusivity
δ_{ei}	Inelastic collision factor
ε	Net emission coefficient [W/m^{3}sr]
ε_n	Small number for the calculation to avoid the denominator becoming zero
η	Wavelength [m]
θ	Angle of the swirl component
κ	Thermal conductivity [W/mk]
κ_c	Curvature of the interface [1/m]
κ_r	Reactive thermal conductivity [W/mk]
κ_t	Translational conductivity [W/mk]
μ	Dynamic viscosity [kg/ms]
μ_0	Permeability of free space [H/m]
ν_{ei}	Collision frequency [1/s]
ρ	Mass density [kg/m^3]
σ	Electrical conductivity [S/m]
σ_t	Surface tension coefficient [N/m]
ϕ	Electric potential [V]
φ	Dependent variable
$\mathbf{\Phi}$	Array of unknown variables
ψ	Compressibility (ρ / p) [s^2/m^2]
ψ_f	Flux limiter

Subscripts

e	Electrons
g	Plasma gas phase
h	Heavy particles
m	Metal phase

Chapter 1

Introduction

1.1. Plasma

A plasma is described as the fourth state of matter, with the other three states of matter being solid, liquid, and gas. A state of matter can go through a phase transition to another state of matter by heat transfer. For example, when a solid obtains enough energy to reach the melting point, it becomes a liquid. Similarly, a liquid can change to gas with the addition of energy.

Similar to the melting or boiling process, adding energy can change a gas to another state of matter through an ionization process. An electron is removed from the atom or molecule of a gas in the ionization process, and the gas transforms to an ionized gas, which is called plasma. A plasma is composed of a mixture of ions, electron, atoms and molecules, which is unlike a gas. Thus, a plasma has much higher electrical conductivity than a gas because the plasma has free charge carriers. This is an important characteristic of a plasma and makes it distinct from a gas, which is known to be an electrical nonconductor.

Plasmas have different types, as shown in figure 1.1. Generally, plasmas can be classified into thermal plasmas and non-thermal plasmas. A thermal plasma is generated by an electric arc at high pressures (> 10 kPa). A thermal plasma satisfies Local Thermal Equilibrium (LTE) when chemical, thermal, and radiative equilibrium are probably present [1]. Under LTE, the temperature of heavy species such as ions, atoms and molecules equals the temperature of electrons in a plasma. However, a thermal plasma does not always achieve LTE when the collision frequency is insufficient to equilibrate with the heavy species and electrons, such as in the vicinity of an arc. The density of the heavy species is several orders of magnitude higher than the density of the electrons, and thus, the temperature of the heavy species can be lower than the temperature of the electrons when the collision frequency is not sufficient to equilibrate with the heavy species and electrons. There is a plasma model that deals with the temperature deviation between heavy species and electrons, and it will be discussed in Chapter 3.

Non-thermal plasmas are generated under low-pressure conditions (< 10 kPa) and have a temperature difference between heavy species and the electrons. There is also a strong chemical non-equilibrium. In some cases, the electron distribution function is non-Maxwellian, so the concept of an electron temperature is meaningless.

Thermal plasmas and non-thermal plasmas are used differently in industrial applications due to their respective advantages and limitations. Considerable research has been done to meet the various challenges of both thermal plasmas and non-thermal plasmas. Thermal plasmas are used in industrial applications such as welding, plasma

spraying, vapor deposition, and waste treatment. For these applications, high heat flux, high species density, and strong radiation are the most important characteristics of thermal plasmas. Non-thermal plasmas are not discussed here, as only thermal plasmas are involved in plasma arc cutting, which is the topic of this thesis.

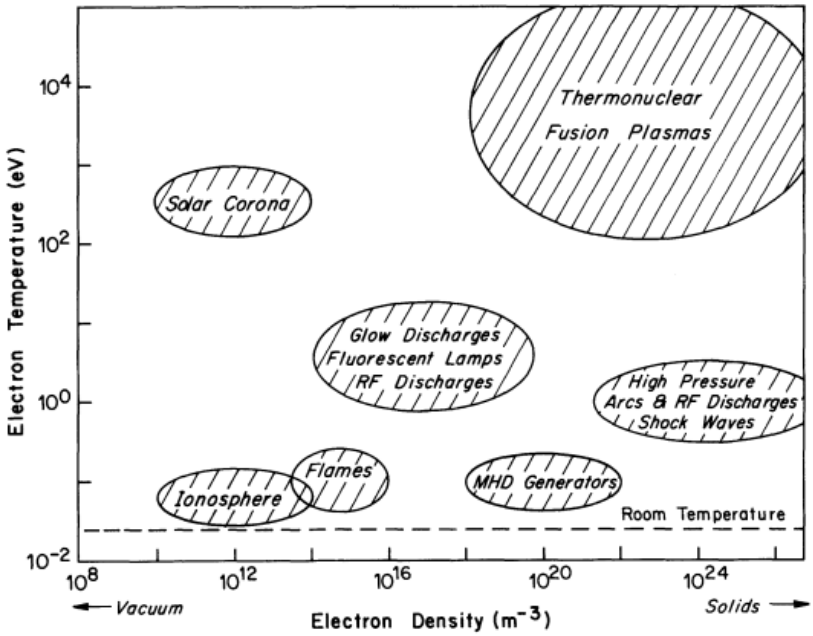

Figure 1.1. Different types of plasmas [1]

1.2. Comparison of primary cutting processes

There are various metalworking methods such as cutting, forming, and joining processes that are used to make basic structures and complex assemblies in industry. Most importantly, the cutting process plays an important role in manufacturing, and it is widely used in manufacturing industries. Cutting processes are classified according to several characteristics, with four major types: oxyfuel, laser, water jet and plasma arc.

Each process has its own distinct advantages and disadvantages, which serve as important criteria for choosing a process when a cutting process is used in various manufacturing applications.

First, oxyfuel cutting is a conventional type of process that uses fuel gases and oxygen to cut metal with oxidation. The advantage of oxyfuel cutting lies in its simplicity and low cost, and it can also cut very thick metal. Disadvantages include a very slow cutting speed and a relatively inferior cut quality compared to that produced by other processes. Oxyfuel cutting is also only used for carbon steel and some alloys because a reaction of oxygen with iron is required to produce the heat for cutting.

Second, laser cutting produces extremely precise cuts, and has a very fast cutting speed. Disadvantages include high cost and an inability to cut thick metal. Therefore, laser cutting is used only for precision manufacturing processes for thin metal or nonmetallic materials.

Third, water jet cutting uses the high pressure of a water jet that includes an abrasive to cut the work piece. Water jet cutting is able to cut any material and produce a good cut quality with no heat-affected zone. The cutting cost is relatively lower than that of laser cutting. However, water jet cutting has a slower cutting speed than both plasma and oxyfuel cutting processes.

Lastly, the Plasma Arc Cutting (PAC) process uses a high temperature plasma arc. When a gas obtains sufficient energy, it becomes ionized, and has the characteristics of an electrical conductor. With proper gas flow and a power supply, the electrical characteristic of plasma allows plasma arc cutting to produce a high temperature plasma

arc and high velocity gas flow for cutting. The speed of this process is faster and the cut is of better quality than that of the oxyfuel cutting process, as shown in figure 1.2. Additionally, the heat-affected zone is relatively small due to the faster cutting speed compared to oxyfuel, as shown in figure 1.3. Although it is more expensive than oxyfuel cutting, plasma arc cutting guarantees a high quality cut, close to that of laser cutting, and is able to cut thick metal plates of up to 10 cm (4 inches). Moreover, it has the advantages of lower costs and higher cutting speed than those of laser cutting. Thus, plasma arc cutting is extremely advantageous when fast production with reasonable cost and good cut quality is important.

30 mm (1.18 in) plate cut with a plasma torch

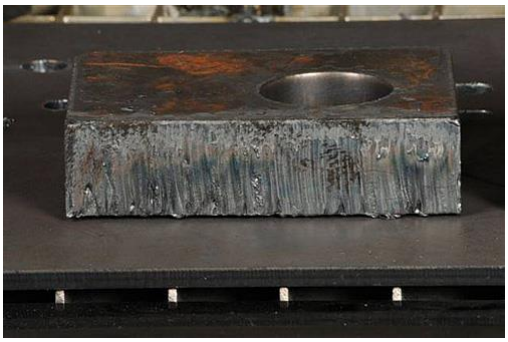

30 mm (1.18 in) plate cut with an oxyfuel torch

Figure 1.2. Comparison of cut quality [2]

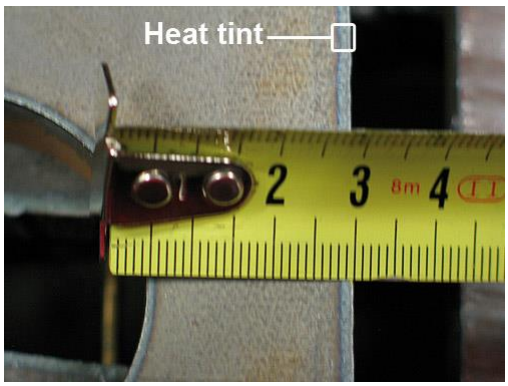

Only 2 mm heat tint with plasma

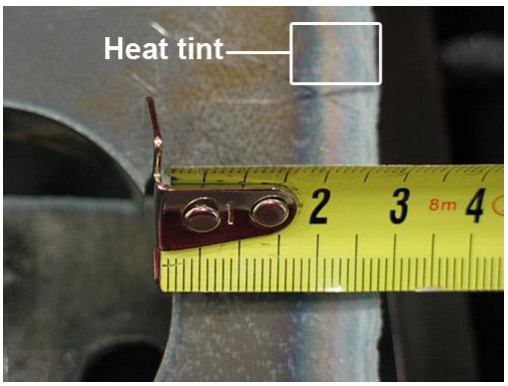

More than 10 mm heat tint with oxyfuel

Figure 1.3. Comparison of heat-affected zone [2]

1.3. Plasma cutting process

The plasma arc cutting system is composed of a torch, a power supply, a gas supply and a high frequency starter (see figure 1.4(a)). In the actual cutting process, the metal to be cut (work piece such as mild steel) is used as the anode. The power supply provides DC power, the gas supply provides a proper mass flow rate of gases for plasma flow and shield flow (see figure 1.4(b)), and the high frequency starter is required to produce a high voltage at a high frequency. This voltage is used to create a high intensity arc that breaks down the gas for the plasma start phase.

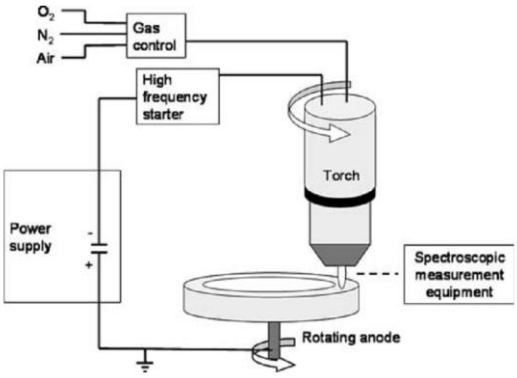

(a)

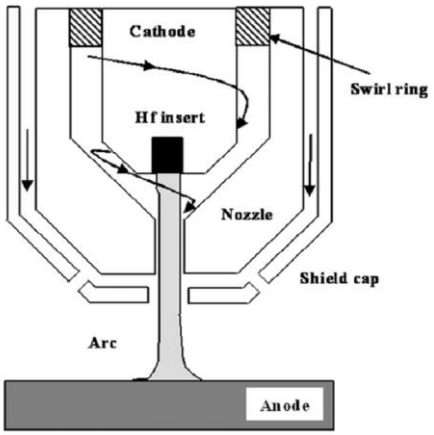

(b)

Figure 1.4. (a) Components of plasma arc cutting system; (b) components of plasma torch [3]

The cutting torch includes the electrode, nozzle, swirl ring and shield cap (see figure 1.4 (b)). A swirl component on the incoming gas is generated by a swirl ring that forces the plasma gas to flow inside a nozzle with swirl to constrict the arc. The shield gas flows outside the nozzle to protect the cutting process from entraining ambient gas. The electrode consists of copper with a hafnium insert. The hafnium insert provides electron emission at high temperatures and is generally used as a cathode for the plasma cutting with oxygen because it can endure erosion that occurs when oxygen is used.

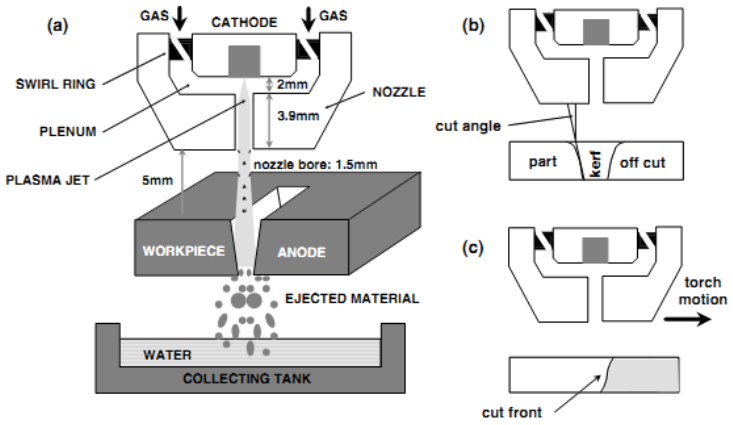

Figure 1.5. (a) Schematic of plasma arc cutting; (b),(c) details of cut-angle and cut front [4]

At the start phase, the high frequency with a high voltage breaks down the region between the cathode and the nozzle inside the torch in order to initiate the arc. Subsequently, the working gas becomes ionized by passing through this arc. After the plasma start phase, the created plasma arc moves from the nozzle to the work piece to make it the anode. Finally, the actual cutting process entails rapid melting at the anode

arc root. Plasma flow is constricted by a very narrow path in the nozzle that increases its temperature by increasing Joule heating, as the narrow bore creates higher electrical resistance. Furthermore, the plasma gas passing through the narrow nozzle bore accelerates to reach a mildly supersonic speed [5].

As the plasma gas leaves the plasma torch, the speed of the plasma gas decreases to a subsonic condition through a shock. The plasma gas passes through a very short distance between the plasma torch and the work piece, which is called the standoff distance. Finally, the plasma gas arrives at the work piece. The amount of heat that is transferred by conduction and convection from the plasma gas and radiation from the plasma is extremely high because the electric arc attaches to the work piece surface, the anode. This heat flux can sufficiently increase the temperature of the metal to the melting point and then molten metal is blown out by the drag force of the high-speed gas flow. The kerf in the work piece is produced by the cutting process (see figure 1.5.b), and is determined by the amount of heat flux and drag force.

In the case of mild steel, oxygen or air is mainly used for cutting because the reaction of oxygen and iron is a powerfully exothermic process, and it can generate extra heat source for melting. Moreover, the surface tension of molten metal becomes smaller when oxygen is used since metal oxide on the surface of the molten metal has small surface tension. This also causes an increase of melt flow and a decrease of dross formation. Dross is re-solidified molten metal that is not removed from the work piece and is attached on the surface of the work piece. Thus, oxygen has several advantages for

melting and dross removal. For these reasons, oxygen or air is widely used for plasma arc cutting.

1.4. Motivation

Improving cut quality and cut speed is directly connected to productivity which is the main goal of this plasma arc cutting research. However, it is very difficult to improve both of these processes at once, because they are interdependently connected. For example, increasing the cut speed causes productivity improvement; however, it also leads to poorer cut quality due to insufficient heat transfer, resulting in more extensive post-processing such as grinding to remove the dross that decreases productivity and incurs additional costs. Thus, the cut speed presents limitations in terms of cut quality. In other words, sufficient cut time is necessary in order to provide high quality cuts.

To better understand the relationship between cut speed and cut quality in plasma arc cutting, it is necessary to understand the factors that determine cut quality. These factors are the dross remaining on the work piece, squareness of the cut, and cut striations. First, there are two types of dross generated during cutting: low-speed dross and high-speed dross. They are classified by cut speed. Low-speed dross formation is a very thick, globular accumulation of the molten metal due to sufficient heat transfer, but high-speed dross formation is a very thin and linear bead of the molten metal due to insufficient heat transfer [2]. These different dross formations are influenced by the cutting speed, and, thus, plasma arc cutting should operate in an optimal cut speed range. Secondly, good cut quality means squareness of the cut, but the actual cut shape has a

beveled angle. The angle measuring the wall from the vertical is called the bevel angle (see figure 1.6). This is related to the uneven heat flux from the plasma arc or molten metal. Lastly, cut metal shows striations on the surface. The striations are a result of a periodicity in heat flux or melt removal (see figure 1.2). Thus, cut quality is influenced by a combination of operation conditions, and this makes it difficult to accomplish optimal conditions. Therefore, research of the kerf is very important for improving understanding about the physical phenomena of the cutting process and to determine optimal conditions to improve cut quality and cut speed.

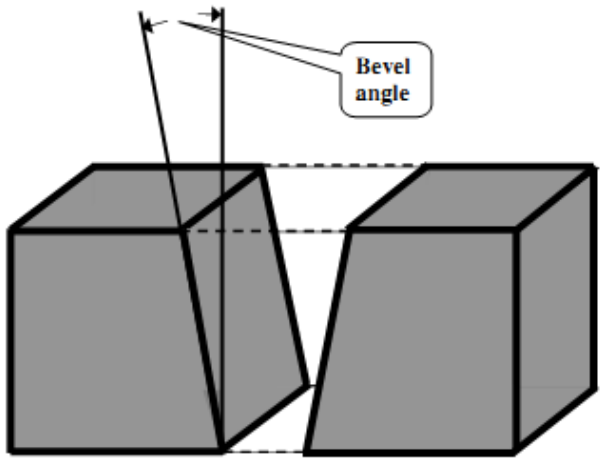

Figure 1.6. Schematic of a cut showing bevel angle [6]

Previous experimental research, however, has not focused on the kerf region because of extremely high temperatures and the enclosed geometry in this region. For this reason, numerical research for studying the kerf region is inevitable. Although

computational fluid dynamics (CFD) has been used for thermal plasma modeling, most previous numerical work in plasma arc cutting focused only on the plasma flow and inside the plasma torch, and, thus, the melt and the melt removal are not captured in the previous work.

The goal of this research is to make a self-consistent, three-dimensional model including the physical phenomena for melting of the work piece as well as the plasma flow. This numerical simulation is a first attempt for plasma arc cutting with kerf formation, and thus the examination of the correlation between simulation results and operation conditions will ultimately help in developing ideas to improve plasma arc cutting.

1.5. Scope of research

To achieve the goal of this work, it is important to choose the appropriate physical phenomena for modeling the cutting operation. Modeling of the physical phenomena is broken down into four approaches: 1) modeling the plasma flow inside the torch and the kerf, 2) modeling heat transfer from the plasma to the melt and solid behind it, 3) modeling removal of the melt from the kerf, and 4) modeling oxidation chemistry and metal vapor near the surface of the melt and their effects on heat transfer, melt properties and electrical properties. Modeling the plasma flow gives the temperature and velocity distributions near the kerf. The heat transfer rate as well as the drag force can be calculated using the plasma model. Subsequently, the melting rate and the kerf shape can be estimated. During this process, oxidation and the metal vapor affect the melting rate

by increasing heat flux and changing plasma properties near the work piece. Other than the oxide effort on surface tension, this last approach is beyond the scope of this work, thus it is postponed. More details of oxidation and vaporization effects are discussed in chapter 3.

Chapter 2 reviews thermal plasma modeling and plasma arc cutting. First, previous plasma modeling and plasma arc cutting literature are discussed, and relevant metallurgy papers are considered to develop the plasma cutting process model in the thesis.

Chapter 3 describes the mathematical formulations of the plasma cutting model. The modeling includes three different phenomena: modeling for the plasma jet flow; the Volume of Fluid (VoF) method in order to determine the location of the liquid interface with the plasma; and the phase change model for the melting process. Assumptions are explained in order to derive the mathematical formulation, which includes the three approaches for the plasma cutting process. Finally, thermodynamic and transport properties are also discussed.

Chapter 4 includes a numerical method to solve the governing equations for a plasma cutting process model using a Finite Volume method. The partial differential equations are converted into a system of algebraic equations using a discretization method. Subsequently, a sparse matrix solver is used to solve the system of equations. The algorithm for connection of the governing equations is given in the last part of the chapter.

Chapter 5 gives a simulation set up for the plasma cutting process. The computational domain, boundary conditions, and initial treatment for the cutting process model will be discussed.

In chapter 6, two different cases are considered for validation. Firstly, a phase change case is considered. Additionally, a compressible two-phase solver, including a plasma phase, is considered for validation.

Chapter 7 shows three-dimensional simulation results for the metal cutting process. The simulation results with different torch flow swirl components, different surface tension values, and different Darcy term values are discussed. The Darcy term gives a flow resistance to hold the solid metal in place, as will be discussed later. The rest of the chapter is reserved to discuss the numerical method changes made in order to improve the simulation results.

Finally, the concluding remarks are presented in chapter 8, summarizing the numerical model developed in the present thesis. Recommendations for future research are also discussed.

Chapter 2

Background and literature review

2.1. History of plasma arc cutting

The key goal of research into the plasma arc cutting process is to improve cut quality and productivity. A plasma arc constricted by a nozzle was first put forth in Gage's patent [7] . This constricted plasma arc leads to an increase in plasma temperature, the arc voltage, and the electric power, making it possible to use for a cutting process. After the first patent, plasma arc cutting was continuously improved, and there were several major development milestones [8]:

- In 1964, air was first considered as a plasma gas, and this improved the cutting speed and the cut quality for steel. However, a tungsten cathode was replaced by zirconium due to fast erosion when using air as the plasma gas.
- In 1970, nitrogen plasma with water-injection (see figure 2.1.a) was introduced, and this made an extremely square cut without rounding on the top edge and improved cooling for nozzle and work piece.
- In the 1980s, oxygen plasma with water-injection was introduced to improve the cut quality for mild steel. Also, when Alternating Current (AC) power is

converted to Direct Current (DC) for the cutting process, the low-amplitude oscillation component of the arc (current ripple) which decreases the electrode life is generated. Thus, low ripple power supplies, and elimination of current overshoot and sloping the current led to an increase in consumable life such as nozzle and electrode. Lastly, hafnium replaced the zirconium cathode. This improved electrode life, making it possible to increase productivity.

- In the 1990s, a dual gas system (air, nitrogen, and carbon dioxide) (see figure 2.1.b), which was first developed in 1960s, was improved, and led to better cut quality and a longer torch life. Selection of shield flow depends on the work piece and plasma gas.

With each milestone, plasma arc cutting became an increasingly powerful cutting process capable of good cut quality and high productivity. However, there is still much room for improvement in plasma arc cutting. For these reasons, research must continue, both experimentally and numerically.

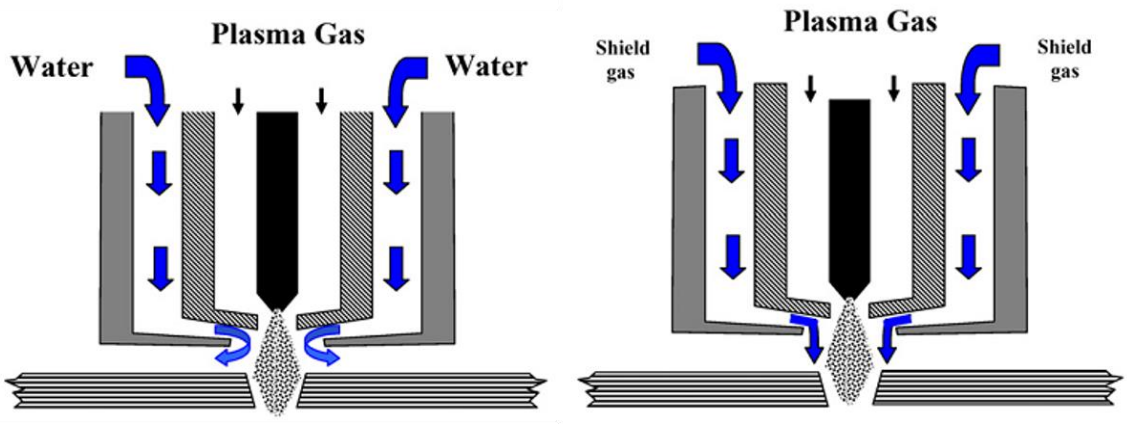

(a) (b)

Figure 2.1. Schematic of water injection (a) and Dual gas (b) plasma arc cutting [8]

2.2. Thermal plasma modeling

Plasma arc cutting is one of the applications of thermal plasmas, and its modeling method is very similar to other thermal plasma applications such as arc welding and plasma spraying. Thermal plasma modeling has been developed to improve the productivity of applications and to understand plasma physics, as documented in [9] . Thermal plasma modeling can be broken into two major components: Computational Fluid Dynamics (CFD) [10] and plasma properties.

CFD is the method used to investigate fluid flow problems using a numerical method. Thermal plasmas can be described by continuum equations, and the governing equations can be discretized using a Finite Volume (FVM) or Finite Element Method (FEM) [10]. These continuous differential equations can be converted into matrix form of discrete difference equations, and solved by a sparse matrix solver. Each governing equation coupled by a CFD algorithm is solved using an iterative method to reach a pre-determined convergence condition. Transport and thermodynamic properties are also required for numerical simulation of thermal plasmas. Due to the high temperature, plasma properties have a strong nonlinear relationship with temperature variation and it is very difficult to measure them experimentally. Instead, properties are calculated using statistical mechanics and gas kinetics [11–13].

2.2.1. Non-equilibrium phenomena in thermal plasmas

In thermal plasma modeling, understanding non-equilibrium phenomena is important, but much is still unclear. The Local Thermodynamic Equilibrium model

(LTE) and the two-temperature model are widely used in thermal plasma modeling. In the LTE model, it is assumed that the energy of the heavy species quickly equilibrate with the energy of the electrons through sufficient collisions among them. However, in a two-temperature model, the heavy species do not equilibrate with the electrons when collisions frequency is insufficient to reach equilibrium. Hsu et al. [14,15] describe the improvement of two-temperature modeling over LTE modeling considering the arc fringes in a free burning arc. A significant difference between heavy species and electron temperature is observed in the arc fringes, The hsu et al. model is in good agreement with experimental results.

Deviations from LTE are also found in the non-transferred arc, which is formed between the cathode and the water cooled nozzle (anode), described by Trelles et al. [16–19]. They developed a three-dimensional transient model for a plasma spray torch. The computational domain for the plasma flow was expanded to the substrate region [19]. Their simulation results with the two-temperature assumption are in better agreement with the experimental data. Also, the LTE model requires a reattachment model to overcome the low electrical conductivity and low temperature near the nozzle wall. Freton at al. [20] studied four different cases about the attribution of the ionization term and the components of thermal conductivity in the two-temperature energy equation. Unlike the LTE model, it is still unclear whether the reactive thermal conductivity should be included in the heavy species or the electron energy equation. Furthermore, there are other simulations using a two-temperature model. Boselli et al. [21] did simulation work for an arc welding process using both LTE and two-temperature models. There was a

large difference in heavy species and electron temperatures observed in the arc fringes and the upstream flow. A two-temperature model was considered in [22–24], however, these investigations consider also chemical non-equilibrium.

When chemical non-equilibrium is considered, the plasma model is much more complex compared to a plasma model with chemical equilibrium. For chemical non-equilibrium, solving the dynamic species conservation equations is essential, and the reaction rates of each species are required. Moreover, a two-temperature assumption is required to consider chemical non-equilibrium. Baeva at al. [22] and Park et al. [24] developed models for argon plasma, and Ghorui et al. [23,25] developed oxygen plasma models for a cutting torch. Although chemical non-equilibrium may be closer to the physical phenomena, it is computationally very expensive.Thus, LTE or a two-temperature model with the assumption of chemical equilibrium are widely used in thermal plasma modeling due to the high computational cost of models that assume chemical non-equilibrium.

2.2.2. Interface of plasma and electrode

The plasma sheath, a thin layer, is placed at the interface between the plasma and the electrode. It can’t be captured by the discretized LTE or two-temperature equations due to imbalance between the number of electrons and positive ions. The number of positive ions is greater than the number of electrons in the plasma sheath, and quasi-neutrality can’t be used for this region. Thus, an additional interface model or assumption, for model simplification, is required to describe the interface near the

electrode. Lowke et al. [26] developed a sheath model for the electrode regions, which includes a simplified unified treatment for sheath effects. Sheath effects are generally neglected due to the relatively small effect on results of the plasma model. However, when an LTE model is used, a method is required to deal with the low electrical conductivity near the electrode surface due to the much lower temperature of heavy species compared to electron temperatures in that region. Initially, ambipolar diffusion was considered near the electrode region [27–29]. The ambipolar diffusion term is included in a general equation using Ohm's law for current density ($\vec{j} = \sigma \vec{E}$), and resolves the electrical conductivity of the problem near the electrodes by increasing the electrical conductivity at a low temperature. Lowke and Tanaka [30] used a large mesh size near the electrodes, resulting in reasonable electrical conductivity due to the relatively high temperature. A thin layer with an artificially high electrical conductivity was included near the electrodes to increase electrical conductivity in the low temperature regions near the electrodes [31,32]. Lastly, the two-temperature model can resolve the low electrical conductivity problem using separate electrons and heavy species temperature, as done in the work by Trelles et al. [16]. Electrons maintain a high temperature with high electrical conductivity in the two-temperature model.

2.3. Plasma arc cutting

Nemchinsky and Severance [33] briefly provide a general review of modeling, heat and mass transfer in plasma arc cutting, and related experimental and numerical results. Hypotheses are proposed regarding important processes in plasma arc cutting,

including cathode erosion, double arcing, dross formation and the shape of the kerf. Their work points out that the cut process and kerf research are very important considerations regarding performance, but currently there are only a limited number of research efforts about the cut-slot region. The problem of dross and squareness of the cut in plasma arc cutting is discussed in [4,6,34,35]. Two types of dross are classified as high-speed dross and low-speed dross, thus maximum and minimum cutting speeds are found experimentally, and a calculation model is utilized to find a dross-free speed using a Weber number, which relates surface tension to drag force, as described by Nemchinsky [34]. The Weber number determines the relative importance of inertial forces and surface tension in a flow. For example, when $We > We_{crit}$, the role of surface tension is insignificant in the flow, and there is no dross formation on the surface. The energy balance of oxygen plasma cutting was investigated for various operating conditions and the two-dimensional temperature distribution of the mathematical heat transfer model was compared to experimental results by Teulet et al. [35], with the results being similar between the model and experiment. This model suggested that kerf width is uniform and doesn't consider the real geometry of the cut, and thus it is limited in describing the kerf region.

Ramakrishnan et al. [4] investigated the influence of three kinds of gas composition on the plasma arc: nitrogen, oxygen and air. Experimental results for different gas compositions in the cut region show that the exothermic reaction of oxygen has an advantage in melting steel. Firstly, the exothermic oxidation reaction with the iron generates additional heat, making the melting process relatively easy. Moreover, it

significantly decreases the surface tension of molten metal, and this reduced surface tension helps to smoothly remove the molten metal. Nemchinsky et al. [6] conducted research about cut speed, cut quality and operation conditions by using a mathematical model, and compared this to experimental results. The results apply to kerf variation (bevel angle) and neglect plasma deflection (plasma jet deflected from the vertical). Plasma deflection, however, is also important at the maximum cutting speed. Therefore, this paper shows that it is difficult to simultaneously describe both effects (kerf variation and plasma deflection).

Spectroscopic measurements are popular experimental methods to investigate the region between the nozzle and the work piece in plasma arc cutting [3,21,36–40]. Ramakrishnan et al. [36,37] first investigated the arc column using spectroscopic measurements, and oblique shock patterns were found at the nozzle exit. Pardo et al. [38] also captured shocks at the nozzle exit in air plasma arc cutting. Spectroscopic measurements by Girard et al. [39] were used to obtain the temperature, the electron number density of each oxygen and nitrogen plasma, and the pressure. Peters et al. [3,40] measured radial and axial distributions of oxygen plasma properties, including temperature.

Although spectroscopic investigation can easily measure time-averaged parameters, they can't be used to capture transient processes such as gas fluctuation. In contrast, high-speed camera imaging (HSC) is widely used to capture transient phenomena in plasma arc cutting. High-speed camera images with good time resolution can be used to investigate the plasma arc including the pilot arc, start-up transition,

cutting phase, and shut-down [41,42]. These papers mention that recent HSC imaging and flow visualization techniques are very good diagnostic techniques for transient processes and arc attachment measurements. Images of HSC, for various operation conditions can be helpful in understanding some basic phenomena.

Bemis and Settles [43,44] visualized the plasma cutting process, taking pictures of the arc attachment with an ultraviolet filter and dross formation with Schlieren imaging. They found that the arc may be attached to the bottom of a work piece when operating with a low cutting speed. Colombo et al. [45] observed different arc attachment behaviors with different cutting speeds. A moving arc attachment was observed only at low cutting speeds.

Arc voltage measurements can also be used to determine arc attachment on the work piece. Osterhouse et al. [46] used this method, and found a stationary arc attachment on the upper region of the kerf. Plasma cutting torch design can also influence cut results. Research about the relationship of the nozzle design, fluid-dynamic arc instabilities and cut quality were conducted experimentally by Kim et al. [47]. The use of micro-jets, jet flow from the micro-channel for the shield gas, leads to reduced arc instabilities and good cut quality, and Kim's paper shows that nozzle design can be an important factor for cut quality.

Along with these experimental and mathematical research studies, computational studies have been continuously conducted with the development of computing technology. Gonzalez-Aguilar et al. [48] developed a simplified model for a cutting torch using CFD for a two-dimensional, LTE model, with laminar flow. Freton et al. [5,49]

used, by means of the commercial code FLUENT a two-dimensional turbulent plasma model applied to an oxygen plasma arc cutting. The numerical simulation was in good agreement with experimental data in terms of the shock wave patterns and temperature and pressure distributions. Ghorui et al. [23,25] developed a model which includes chemical and thermal non-equilibrium effects for the arc inside the nozzle of a plasma arc cutting torch. This research discussed results showing that LTE is not valid for the fringe of the arc. Colombo et al. [50] did numerical simulation research on various geometries of the torch and several operation conditions in plasma arc cutting. This research includes the effects of shield gas flow, torch design, and k-ε modeling of turbulence with an assumption of LTE. Zhou et al. [51] conducted simulations for various swirl gas conditions. High swirl gas constricted the plasma arc; however, it also accelerated cathode erosion due to an increase in plenum pressure and an increase in the plasma flow to the cathode. Long et al. [52,53] developed a model that includes a cathode evaporation model with different cathode holder shapes and different swirl gas angles to investigate cathode evaporation in oxygen plasma cutting.

These numerical studies demonstrate that CFD modeling for plasma cutting is very useful in that CFD modeling can dynamically change the nozzle design, and make it easy to obtain calculational results, such as temperature and velocity distributions. These results are important components for determining cut quality and cut speed. Changing nozzle design and operation conditions are critical, but entail high costs if done in experimental research. CFD modeling makes it possible to obtain specific results for various operational conditions at substantially lower developmental cost.

2.4. Modeling in relevant metallurgy

CFD modeling is a very powerful tool for research into plasma arc cutting without physical experimentation. Previous CFD modeling studies were limited since they only focused on the plasma torch region. As mentioned above, a review paper [33] has emphasized the need for kerf research, but currently there is very little research on this specific topic. However, models that include the solid metal phase, the molten phase, as well as the gaseous phase can be found in relevant metallurgical studies, such as in arc welding, laser welding, and laser cutting processes.

2.4.1. Interface of molten metal and solid

Phase change models are required to capture the melting and solidification of the work piece in the arc welding model, including the welding pool, or in the cutting model, including the melting process. Generally, an interface capturing method is widely used in order to capture the complex interface of the solid and the liquid phase in welding or cutting processes [54–57]. Both solid and molten metal are considered to be present in the computational domain, and the solid state includes the Darcy force term or artificially high viscosity to maintain a solid phase. The Darcy force term is required to treat solid as fluid with high flow resistance. Solid or liquid is defined by temperature, and in the case of metal alloys, the partially solidified region is located by liquidus and solidus temperature. The latent heat of fusion is also considered for the melting process. This

approach is based on the work by Voller et al. [58,59]. Murphy [60,61] developed a self-consistent three-dimensional model of the arc welding process to describe the arc, electrode and weld pool. Including vaporization of metal leads to reasonable results by decreasing temperature and changing plasma properties.

2.4.2. Interface of metal and gaseous phase

Volume of Fluid (VoF) is widely used to capture the interfaces in immiscible two-phase flows [62]. This method can be easily applied to cutting or welding process models; however, a very small time step and a fine mesh are required to obtain accurate results. Additionally, the interface between the plasma gas and the work piece has a sharp gradient of properties and variables, and, thus, including the VoF method has considerable computational cost. In arc welding modeling, there are alternative methods to obtain the interface of the solid and the liquid. This is the equilibrium surface method, developed by Kim et al. and Wu et al. [63,64]. The interface of the weld pool is determined by the minimum total surface energy, including surface tension energy, gravitational potential energy and pressure work. An equilibrium surface method, however, is not used for the laser cutting process model. Thus, the VoF method is generally used to capture the surface deformation of the work piece in the cutting process [54,65] .

Chapter 3

Mathematical formulation of the model

3.1. Introduction of numerical models

This chapter presents the numerical models for the plasma cutting process and the related mathematical formulations for each numerical model. As shown in the figure 3.1, the plasma cutting process includes complex phenomena, including melting by the plasma flow. A plasma flow of high temperature and high speed melts and blows out the molten material. This process involves four phases, plasma, a solid work piece, molten metal, and metal vapor. Thus, all of these should be considered to make a more accurate model. Also, phase change between the molten metal and the solid work piece is necessarily included, as well as the electro-magnetic effects needed for describing the thermal plasma. Although the entirety of physics should be considered to truly reflect reality, it is difficult to develop a model that includes all the physics in the cutting process. The important point of modeling is that simplifications are necessary and can be done by capturing just the relevant physics.

In the present work, essential physical phenomena are roughly categorized into three sub-models, as shown in figure 3.2. These are a model of the plasma flow, a model

of heat transfer to the melt from the plasma, and a model for removing the melt from the kerf. In this chapter, each sub-model is discussed and the mathematical formulation is explained. Then, the final plasma cutting process model, which is developed by combining each of the sub-models, is discussed.

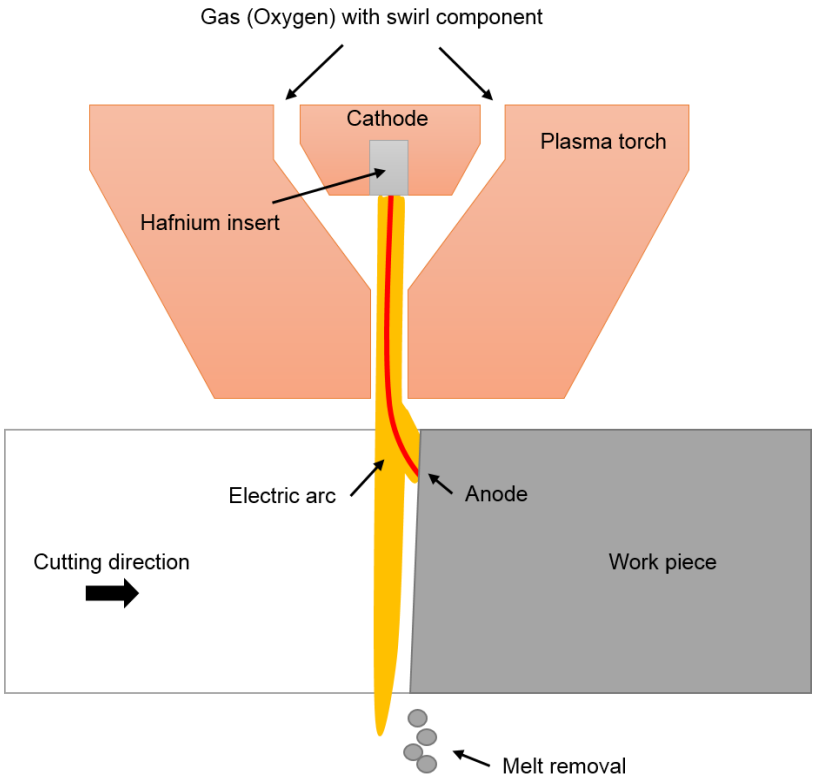

Figure 3.1. Schematic of the plasma arc cutting process (Shield gas components are neglected)

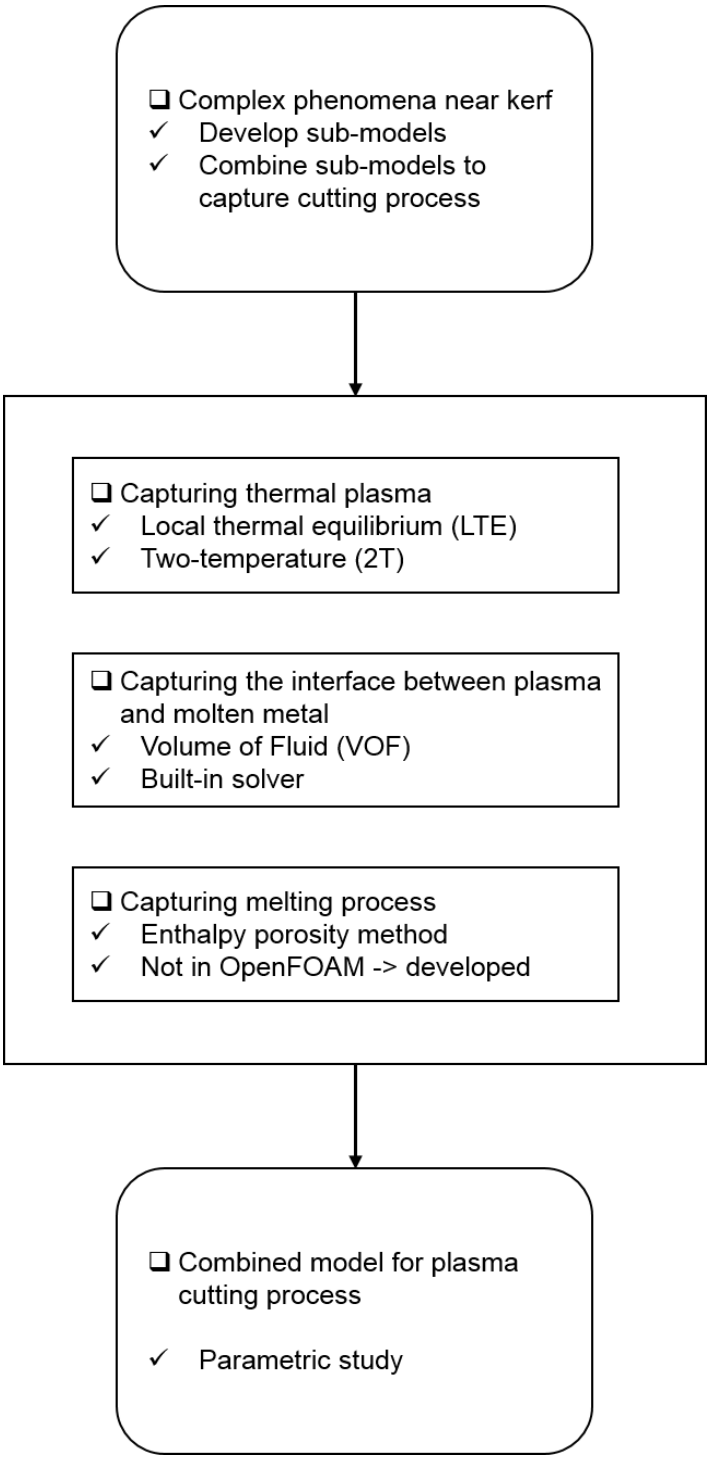

Figure 3.2. Methods to model relevant physics in plasma arc cutting

3.2. Assumptions

The molten metal, as well as the plasma, are considered as a continuum fluids to be implemented in computational fluid dynamics (CFD). When the mean free path of a fluid is much less than the length scale of a problem, this fluid is assumed to obey the continuum assumption. Thus, the continuum assumption allows the use of standard governing equations, including continuity, momentum, and energy equations for fluid flow. Also, CFD methods solving the governing equations can be used for numerical simulation of this work.

Local thermodynamic equilibrium (LTE) and two-temperature assumptions are used to capture the plasma phenomena. The LTE model assumes that the heavy species temperature is equal to the electron temperature and the plasma is described by a single energy equation. However, the two-temperature model considers that the heavy species and the electrons follow two separate Maxwellian distributions. Thus, the heavy species temperature is not equal to the electron temperature and the plasma is described by both the heavy species energy equation and the electron energy equation. That is, the two species are not in thermal equilibrium.

Only a pure oxygen plasma is considered in the plasma model. The oxygen plasma flow passes through a space filled with pure oxygen and the work piece. Air is not included in the model in order to simplify the cutting process model for this early step because the inclusion of air necessitates additional reactions, properties and species transport equations, and, thus, this is computationally very expensive. While this might

improve the simulation results, air is neglected for the simplification of the cutting process model.

Metal vapor is not included in the model. Physically, metal vapor is generated near the anode region during the plasma cutting process due to the high thermal energy brought from the plasma arc in the region. The inclusion of metal vapor reduces temperature near the work piece by increasing electrical conductivity and radiative emission, and this would lead to a more accurate model. [61]. Similar to the inclusion of air, it is very difficult to include generation of metal vapor into the model. Also, in this work, the region of vaporization is not at a boundary, but is inside of the computational domain; thus, it is not easy to determine vaporization on the interface between the plasma gas and the molten metal. This is beyond the scope of the thesis, and thus, the effect of metal vapor is not included in the model.

The plasma is considered to be in chemical equilibrium with the LTE model and, thus the chemical composition of the species is determined only by pressure and, heavy species temperature. With the two-temperature model, the chemical composition is also a function of electron temperature.

Quasi-neutrality of the plasma is used for this model. In this assumption, the numbers of positive ions and electrons are equal within the same space, and charge does not build up or collect anywhere in the domain. Thus, a plasma sheath effect near the electrode is neglected in the model.

Oxidation of the metal is not included in the model. When oxidation is considered, an exothermic process creates a heat source in the melting zone and a heat

flux calculation is needed at the interface between the plasma and the molten metal flow. Oxidation not only increases thermal energy transport to melt the work piece, but affects the viscosity and surface tension of the molten metal. This is directly related to molten metal flow on the work piece, and thus it represents a significant effect on the simulation results. Although inclusion of oxidation in the model would be more reasonable, it is very difficult to develop this model. Thus, it is beyond the scope of this work and so oxidation is not considered.

It is assumed that molten metal and plasma gas are immiscible fluids, and thus a sharp interface occurs between them due to incapable of mixing. The Volume of Fluids (VoF) method is used to capture this sharp interface. In the VoF method, a source term for surface tension is considered for only the constant surface tension coefficient. For example, a temperature gradient term can be included for the thermal Marangoni effect, and generally surface tension reduces with the increase of temperature. Thus, this affects the interface location between two phases. However, only a constant value for the surface tension coefficient is selected to be applied for the interface between the plasma gas and the metal phase in this thesis due to the model simplification. This method will be discussed in section 3.5

In order to describe the melting of the work piece, the solid is considered as a fluid having high flow resistance. Thus, there are three different fluids in the modeling: the plasma gas, the molten metal, and the solid (treated as fluid with high flow resistance). Also, the mushy zone, which is a partially solidified region, is included in the model because the work piece (mild steel) does not consist of a pure metal but a

composite of different materials. Thus, the work piece has a different liquid temperature and solid temperature and a region between them, where both solid and liquid states exist during melting are considered. To capture the solid state and the melting process, the enthalpy-porosity method [66] is used. This will be discussed in section 3.6.

The net emission coefficient model is used to capture the radiation heat loss. In this case, the radiative heat flux to the kerf is not captured. This will be discussed in section 3.4.4.

Turbulence effects are neglected, and thus no turbulence model is used. The plasma gas is considered to be laminar flow. This assumption would be reasonable to the plasma torch and the kerf [25,67], but the turbulence effects can be found in the region between the torch and the kerf. However, the present work is mainly focused on the melting process in the kerf, and thus, the inclusion of turbulence is neglected.

Viscous dissipation is neglected because it is not a significant energy term compared to other heat generation processes, such as Joule heating or radiation.

3.3. Governing equations

The same set of governing equations is used for the three different phases, and, thus, a volume fraction is required to represent the each phase. Two separate volume fractions are used in the VoF method and phase change model. The volume fractions of the plasma gas and the work piece are expressed by (3.1). The volume fractions of the fluid and the solid states are expressed by (3.2). By using a combination of these two

kinds of the volume fractions, this model can capture three different phases: plasma gas, melt, and solid metal, as shown in figure 3.3.

$$\begin{cases} \alpha = 0 & \text{plasma gas} \\ 0 < \alpha < 1 & \text{region consisting of plasma and metal} \\ \alpha = 1 & \text{metal (melt, solid metal)} \end{cases} \tag{3.1}$$

$$\begin{cases} \gamma = 0 & \text{solid} \\ 0 < \gamma < 1 & \text{mushy zone} \\ \gamma = 1 & \text{liquid} \end{cases} \tag{3.2}$$

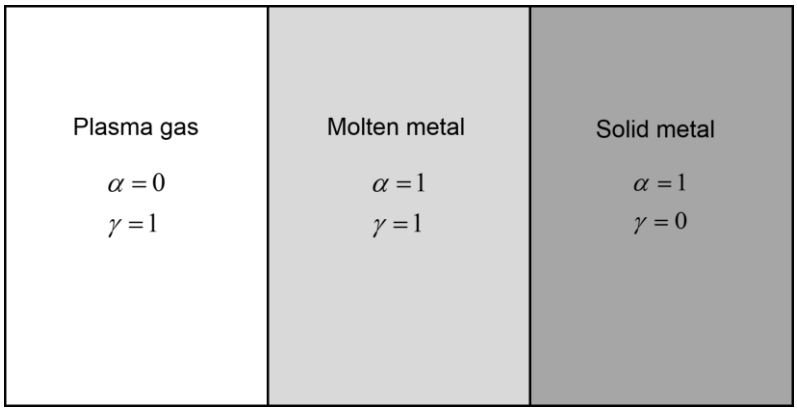

Figure 3.3. Three different phases in the model

The governing equations include all of the assumptions in section 3.2. In other words, the plasma flow, the interface of the plasma flow, the molten metal, and the melting process are described by the governing equations throughout the whole computational domain. The following are the governing equations for the plasma arc cutting process. The continuity equation is

$$\frac{\partial \rho}{\partial t} + \nabla \cdot \left(\rho \vec{u} \right) = 0 \tag{3.3}$$

where ρ is the density, $\vec{u}$ is the velocity of the plasma or the molten metal.

The phase transport equation for each of the fluids of the VoF method is

$$\frac{\partial \left(\alpha_i \rho_i \right)}{\partial t} + \nabla \cdot \left(\alpha_i \rho_i \vec{u} \right) = 0 \tag{3.4}$$

where α is the volume fraction of the metal, while subscript i stands for the metal (1) or the plasma (2).

The momentum equation is

$$\frac{\partial}{\partial t}\left(\rho \vec{u} \right) + \nabla \cdot \left(\rho \vec{u} \vec{u} \right) = -\nabla p + \nabla \cdot \left(\mu \nabla \vec{u} \right) + \vec{j} \times \vec{B} + \rho g + F_p + F_s \tag{3.5}$$

where p is the pressure, μ is the dynamic viscosity, $\vec{j}$ is the current density, $\vec{B}$ is the self-induced magnetic field, g is the acceleration due to gravity, $\vec{j} \times \vec{B}$ is the Lorentz force, F_s is the surface tension force, F_p is Darcy force. Forces F_s and F_p will be discussed in section 3.5 and 3.6, respectively.

The energy equation with the LTE assumption is

$$\frac{\partial}{\partial t}\left(\rho h \right) + \nabla \cdot \left(\rho \vec{u} h \right) = \nabla \cdot \vec{q} + \frac{Dp}{Dt} + \left(1 - \alpha \right) \frac{5}{2} \frac{k_b}{e} \left(\vec{j} \cdot \nabla T \right) + \vec{j} \cdot \vec{E} - \left(1 - \alpha \right) \dot{Q}_r \tag{3.6}$$

where h is the specific enthalpy, $\vec{q}$ is the diffusive heat flux, k_b is the Boltzmann constant, e is the charge of an electron, $\vec{j}$ is the current density, $\vec{E}$ is the electric field, $\vec{j} \cdot \vec{E}$ is the

Joule heating, Q_r is the radiation heat loss. Enthalpy, h, of the metal phase includes the latent heat of fusion, as will be discussed in section 3.6. The second and third terms on the right side of the energy equation with the LTE assumption (3.6) are the pressure work and the transport of energy by electron diffusion, respectively.

The energy equation with the two-temperature assumption is

$$\frac{\partial}{\partial t}\left(\rho_h h_h\right)+\nabla\cdot\left(\rho_h \vec{u} h_h\right)=\nabla\cdot\vec{q}_h+\frac{Dp_h}{Dt}+\left(1-\alpha\right)\dot{Q}_{eh} \tag{3.7}$$

$$\begin{aligned}&\frac{\partial}{\partial t}\left(\rho_e h_e\right)+\nabla\cdot\left(\rho_e \vec{u} h_e\right)\\&=\nabla\cdot\vec{q}_e+\frac{Dp_e}{Dt}+\left(1-\alpha\right)\frac{5}{2}\frac{k_b}{e}\left(\vec{j}\cdot\nabla T_e\right)+\vec{j}\cdot\vec{E}-\left(1-\alpha\right)\dot{Q}_r-\left(1-\alpha\right)\dot{Q}_{eh}\end{aligned} \tag{3.8}$$

where the subscripts e and h represent electrons and heavy particles, respectively. The source term Q_{eh} is the energy transfer from the electrons to the heavy particles due to elastic collision with each other. The electric and magnetic potential equation to be discussed are required for the Lorentz force and Joule heating.

The electric potential equation is

$$\nabla\cdot\left(\sigma\nabla\phi\right)=0 \tag{3.9}$$

where σ and ϕ are the electrical conductivity and the electric potential, which are related to the electric field and the current density. For the joule heating term in the energy equation, $\vec{j}$ and $\vec{E}$ are used. They are defined by the equations.

$$\vec{j}=\sigma\vec{E}=-\sigma\nabla\phi \tag{3.10}$$

$$\vec{E}=-\nabla\phi \tag{3.11}$$

The magnetic potential equation is

$$\nabla^2 \vec{A} = -\mu_0 \vec{j} \tag{3.12}$$

where $\vec{A}$ is the magnetic potential and μ_0 is the permeability of free space. The magnetic field is defined by the calculation of the magnetic potential using (3.12). For the Lorentz force in the momentum equation, $\vec{B}$ and $\vec{A}$ are used.

$$\vec{B} = \nabla \times \vec{A} \tag{3.13}$$

Both enthalpy and temperature are included in the energy equation, and the energy equation with only one independent variable, such as temperature or enthalpy is required in order to solve this equation using the CFD methods. In the present work, the enthalpy is changed to temperature by using the relationship between enthalpy and temperature. For the LTE case, the relationship between enthalpy and temperature for the plasma gas is given by [68],

$$dh = C_{p,g} dT \tag{3.14}$$

And metal phase has a latent heat term, and the relationship between enthalpy and temperature is given by,

$$h = \int_{T_{ref}}^{T} C_{p,m} dT + \gamma L \tag{3.15}$$

where C_p is the constant pressure specific heat, L is the latent heat of fusion, γ is the liquid fraction, and the subscripts m and g represent the metal and plasma gas phase,

respectively. Using these relationship between enthalpy and temperature, the energy equation (3.6) can be written as,

$$\begin{aligned}&\frac{\partial}{\partial t}\left(\rho C_p T\right)+\nabla\cdot\left(\rho\vec{u}C_p T\right)\\&=\nabla\cdot\vec{q}+\left(1-\alpha\right)\frac{5}{2}\frac{k_b}{e}\left(\vec{j}\cdot\nabla T\right)+\vec{j}\cdot\vec{E}-\left(1-\alpha\right)\dot{Q}_r-\alpha L\left(\frac{\partial}{\partial t}\left(\rho\gamma\right)+\nabla\cdot\left(\rho\vec{u}\gamma\right)\right)\end{aligned} \tag{3.16}$$

The last term in the right hand side will be discussed in section 3.6. For the two-temperature case, the relationship between enthalpy and temperature is more complex because heavy species temperature, electron temperature, and pressure should be considered [68]. A cutting process model using a two-temperature model was also developed with additional terms in an energy equation. However, the simulation results can't be obtained by using a two-temperature model due to an unresolved numerical problem. Thus, governing equations for the cutting process model using a two-temperature model are not included in this thesis. Instead, the possibility of using a two-temperature model will be discussed in the chapter 7.

As described in section 3.1, the plasma cutting process model includes three different sub-models. Each of these has related source terms in the governing equations. The explanations for the sub-model source terms will be given in the next three sections. The plasma model will be discussed in detail in section 3.4. Also, the VoF method will be discussed in section 3.5 and the phase change will be discussed in section 3.6. Lastly, the phase-weighted thermodynamic and transport properties used for the governing equations will be discussed in section 3.7.

3.4. Thermal plasma models

In order to accurately capture thermal plasma phenomena, modeling the plasma flowing from a plasma torch to the kerf of a work piece is required. Both the local thermodynamic equilibrium (LTE) and the two-temperature models are considered in this work and details of these models are found in [68]. The LTE assumption has one energy equation, but the two-temperature assumption has two separate energy equations, as shown in section 3.3. In the two-temperature assumption, energy is carried by both electrons and heavy species, and thus the pressure work and the thermal conductivity in the energy equation with the two-temperature assumption are more complicated than those of the energy equation with the LTE assumption. Also, the energy exchange term $\dot{Q}_{eh}$ is included in the two-temperature assumption to make a connection between the two energy equations.

3.4.1. Thermal conductivity

The conduction term with the LTE assumption is easily defined from Fouriers' law as follow:

$$\vec{q} = -\kappa \nabla T \tag{3.17}$$

where κ is the thermal conductivity, which is the sum of the translational and reactive thermal conductivities ($\kappa = \kappa_t + \kappa_r$). However, thermal conductivity is more complex for the two-temperature assumption. In this case, the thermal conductivity is divided into four components. The translational thermal conductivity of the heavy species, the

translational thermal conductivity of the electrons, the reactive thermal conductivity regarding the heavy species temperature gradient, and the reactive thermal conductivity regarding the electron species temperature gradient. Translational thermal conductivity of the heavy species and the electrons are included in the conduction term of the heavy species energy equation and the electron energy equation, respectively. However, dealing with the reactive thermal conductivity for the heavy species and the electrons is more difficult because the reactive thermal conductivity depends on both the heavy species and the electrons. This is discussed in [20]. In this work, it is assumed that the reactive thermal energy is stored in the heavy species. Thus, the diffusive heat flux of the two temperature analysis is defined as

$$\vec{q}_h = -\kappa_h \nabla T_h - \kappa_{rh} \nabla T_h - \kappa_{re} \nabla T_e \tag{3.18}$$

$$\vec{q}_e = -\kappa_e \nabla T_h \tag{3.19}$$

where κ_h is the translational thermal conductivity of the heavy species, κ_e is the translational thermal conductivity of the electrons, κ_{rh} is the reactive thermal conductivity of the heavy species and κ_{re} is the reactive thermal conductivity of the electrons.

3.4.2. Pressure work

In the two-temperature assumption, the pressure work term should be divided into the partial pressure work for heavy species and the partial pressure work for electrons. Thus, the pressure work is expressed as

$$\frac{Dp}{Dt} = \frac{Dp_h}{Dt} + \frac{Dp_e}{Dt} \tag{3.20}$$

With

$$p_h = \sum_{i \neq e} n_i k_b T_h \tag{3.21}$$

$$p_e = n_e k_b T_e \tag{3.22}$$

where n_i is the number density of species i and k_b is the Boltzmann constant.

3.4.3. Energy exchange between electrons and heavy species

The term Q_{eh} represents the energy exchange between electrons and heavy species in equations (3.7) and (3.8), and is given as [68].

$$\dot{Q}_{eh} = \sum_{i \neq e} 3k_b \frac{m_e}{m_i} n_e \nu_{ei} \left(T_e - T_h\right) \delta_{ei} \tag{3.23}$$

where m_i is the mass of species i, m_e is the mass of electrons, ν_{ei} is the collision frequency, δ_{ei} is the inelastic collision factor in order to describe the inelastic effects. Energy of electrons is transferred to heavy species by elastic or inelastic collisions. When electrons collide with monatomic species, it seems to be elastic collisions. However, for the diatomic species, electron energy is transferred to the molecules for vibrational and rotation energy by inelastic collisions, and inelastic effects should be considered in (3.23) . Thus, for the diatomic species, the inelastic collision factor is much larger (10-1000) than 1, and for the monatomic species, the inelastic collision factor is generally 1. The effect of the inelastic collision is discussed in [68] for plasma flow using oxygen.

3.4.4. Radiation heat transfer

The Q_r term represents radiation heat transfer in the energy equations (3.6) and (3.8). Radiation is part of the significant heat transfer to the kerf because of the high temperature of thermal plasma. Therefore, radiation models are used in the plasma modeling. The purpose of the radiation models is to obtain accurate distributions of temperature and heat flux to the kerf in the plasma model. In previous research, three types of radiation models have been used: the net emission coefficient model [69], the P1 model [49], and the discrete ordinates model [50]. The latter two will be discussed later in this section.

The net emission coefficient model is the simplest of these three. This model assumes that radiation in an isothermal sphere which has an effective radius R_{eff} (approximately the radius of the plasma arc). Radiation is emitted and then some of the radiation is reabsorbed by the surrounding sphere. Radiation which is not absorbed by the surrounding sphere is considered as radiation lost to the ambient air. Radiation scattering is neglected. Thus, the net emission coefficient is calculated from differences between emission in a particular solid angle and absorption by the surrounding sphere. As shown in figure 3.4, the net emission coefficient for oxygen is calculated in [70], and where it is calucated as,

$$\varepsilon = \int_0^\infty I_{b\eta} k_\eta \exp\left(-R_{eff} k_\eta\right) d\eta \tag{3.24}$$

where $I_{b\eta}$ is the black body intensity, η is the wavelength, and k_{η} is the absorption coefficient. The black body intensity and the absorption coefficient are functions of the wavelength and temperature. Thus, the net emission coefficient is a function of only temperature and effective radius. By integrating the net emission coefficient for all solid angles, the total radiation loss is calculated as,

$$\dot{Q}_r = 4\pi\varepsilon \tag{3.25}$$

The net emission coefficient model allows determination of the temperature distribution without expending much time on calculation. However, a weakness of this model lies in its inability to calculate heat flux in the computational domain, thus, heat flux to the kerf wall can't be calculated. Despite this disadvantage, this model is widely used in plasma research due to its recognized accurate temperature distribution and its computational efficiency.

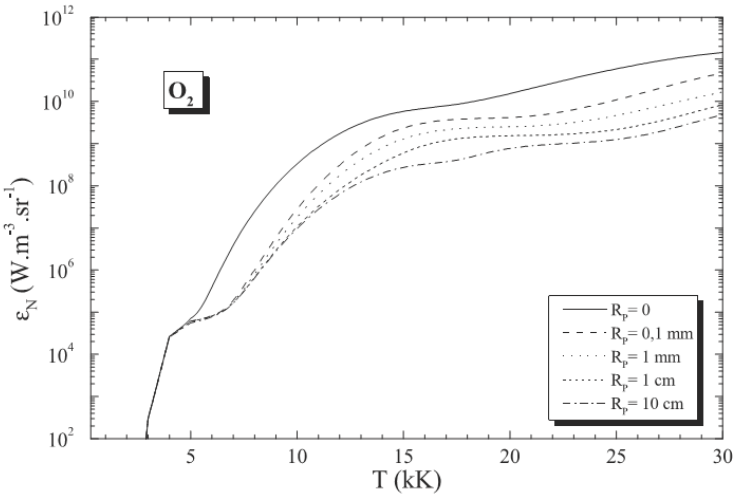

Figure 3.4. Net emission coefficient of oxygen plasma [70]

The P1 and discrete ordinates models allow one to obtain the radiative heat flux at every point in the geometry. Therefore, they can be used to calculate heat flux to the kerf. The P1 model gives an approximation of the solution to the radiative transfer equation using spherical harmonics. Radiation intensity can be broken down into a series of the special functions for the surface of a sphere. Thus, this model has the advantage of simplifying the equation. The discrete ordinates model allows solving the radiative heat transfer equation for a discretized finite direction of radiation. Since the discrete ordinates model solves the equation of each finite direction, it is computationally very intensive. Both the P1 and discrete ordinates models, despite having different methods to solve the radiative transfer equation, can be used to find accurate heat flux to the kerf wall. However, these models are computationally expensive, thus these models are not considered.

3.4.5. Thermodynamic and transport properties

Thermodynamic and transport properties are very significant in modeling of thermal plasmas because the change of properties with temperature shows strong non-linearity. However, it is not easy to obtain these properties from experimental measurements due to the extremely high temperatures. Instead, thermodynamic and transport properties are calculated using statistical mechanics and gas kinetics. First, the equilibrium chemical composition of the plasma should be calculated by using the mass action laws of statistical mechanics, as shown in figure 3.5. Second, the thermodynamic properties can be obtained using statistical mechanics. Last, the transport properties are calculated using the Chapman-Enskog method [11–13].

The calculation of the properties is not included in this document, it is beyond the scope of this work. Rather, the thermodynamic and transport properties are obtained from [68] for both the LTE and two-temperature assumptions, as shown in figure 3.6.

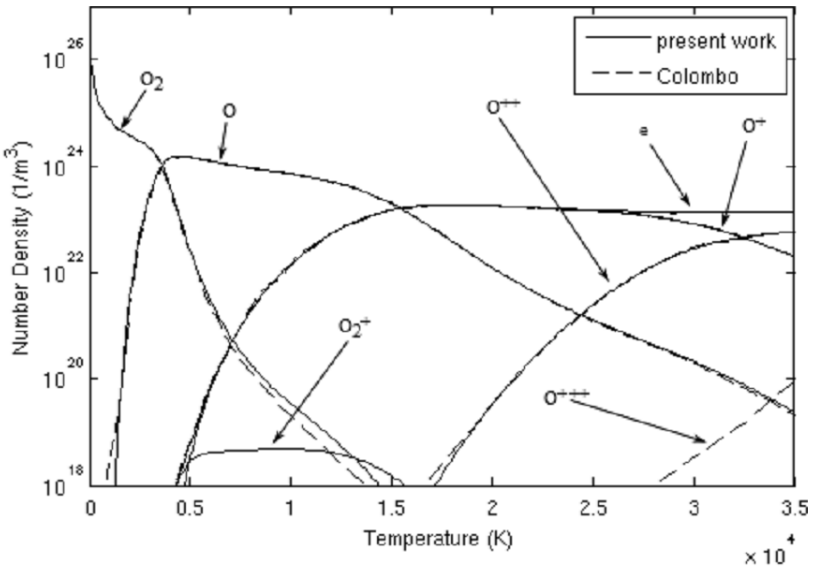

Figure 3.5. Chemical composition of a pure oxygen plasma [68]

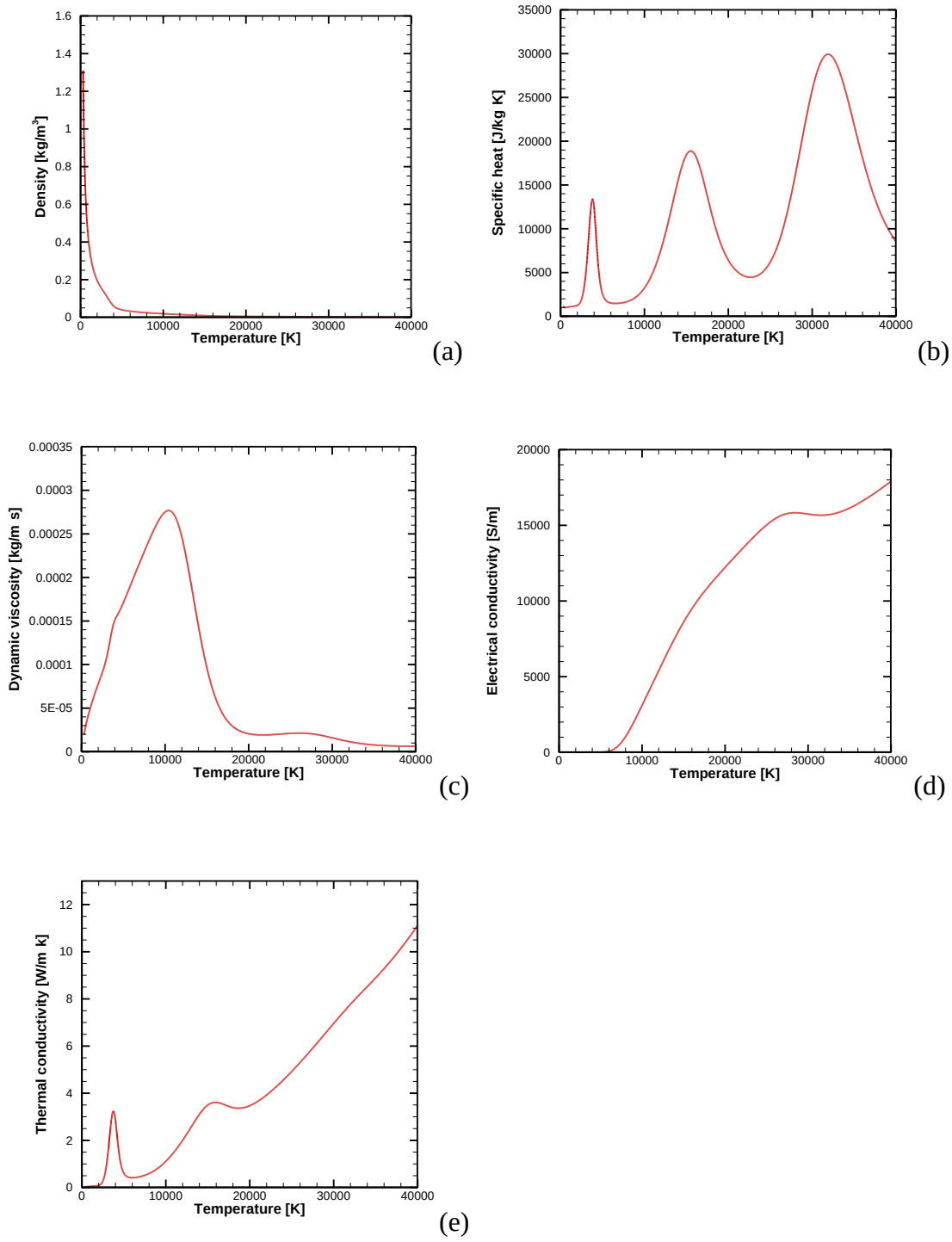

Figure 3.6. Plasma properties for LTE model (a) density (b) specific heat (c) dynamic viscosity (d) electrical conductivity (e) thermal conductivity [68]

3.5. Plasma gas and molten metal model

3.5.1. Volume of fluid

Plasma gas and molten metal flow are considered as an immiscible two-phase flow. In this case, plasma and molten metal flow are not a mixture and they have a sharp interface in order to separate the immiscible flows. Generally, the interface shape is very complex and it is not easy to predict. Thus, capturing the interface is a key point of the two-phase flow model and three models have been developed in order to accurately determine the interface location (see figure 3.7).

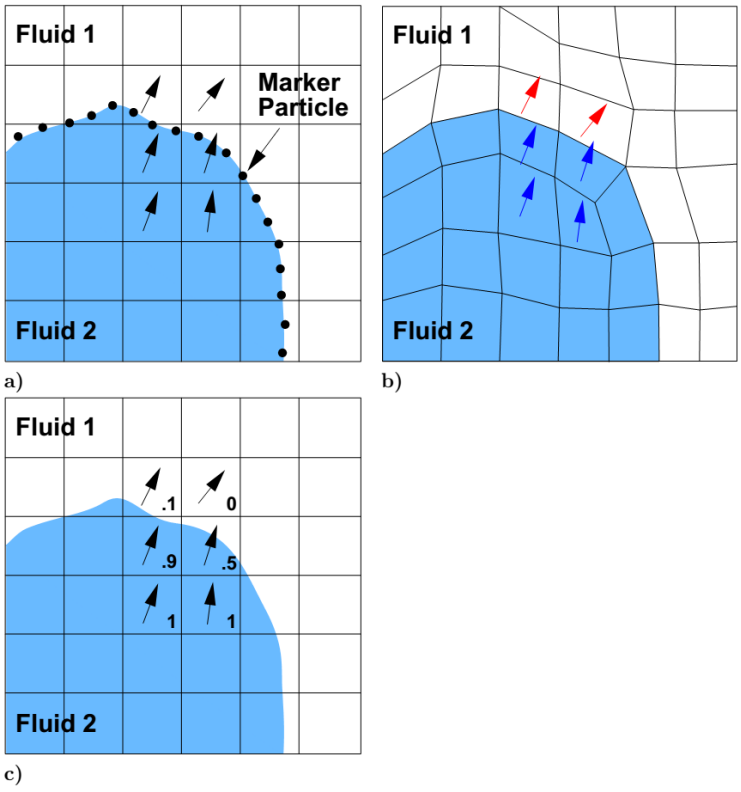

Figure 3.7. Free surface modeling: a) interface tracking with special marker; b) interface tracking with moving mesh; c) interface capturing with volume fraction [71]

In numerical analyses, there are two popular approaches for the interface prediction of an immisicible two-phase flow. The first approach is the interface tracking method. In this method, the interface is explicitly described by special marker points or a moving mesh, as shown in figure 3.7 (a) and (b). These two interface prediction methods have a slight difference between them, but they are considered to be Lagrangian methods and are nearly identical.

The interface tracking method results in a reasonable interface for simple cases, such as a single droplet. However, this method is usually not used for complex interfaces. The interface between the plasma gas and the molten metal flow near the kerf has a very complex geometry due to melting and dross generation, and, thus, the prediction of the interface using the interface tracking method would be computationally expensive. And, thus, is not used in this report.

The other approach is the interface capturing method. The interface is captured implicitly by a fraction for each phase in a fixed mesh. Thus, in contrast with the interface tracking method, the interface capturing method has no limitations on complexity of the interface due to the following implicit capturing methods. The Volume of Fluid (VoF) [62] and Level Set (LS) [72] methods are two famous methods for interface capturing. Firstly, VoF introduces an additional volume fraction transport equation and volume fraction gamma is used to represent each phase. As seen in figure 3.3 (c), the volume fraction range is from 0 to 1 with the gaseous phase and liquid phase represented as 0 or 1, respectively. If both phases exist in a computational cell, the value is determined by the volume fraction of each phase. Secondly, the Level Set method uses

positive values, negative values, and 0 for capturing the interface. The first phase, second phase, and the interface are represented by positive values, negative values, and 0, respectively. Although VoF causes numerical smearing of the fluid interface, it has an advantage for mass conservation. In this work, VoF was selected for capturing the interface of plasma gas and molten metal flow for several reasons. OpenFOAM [73] already has the built-in solver OpenFOAM version called (compressibleInterFoam) based on the VoF method. It is possible to save time for solver development by using the VoF method. Second, a VoF method in OpenFOAM is implemented in the solver and this method gives better predictions of the interface location than the conventional VoF method [74]. In VoF method in openFOAM, an additional convective term, "compression term" for the weighted average velocity in order to accurately capture the sharp interface. Validation based on a VoF solver in openFOAM has been done in various ways by Deshpande et al. [75] and the results good agreement with the literature. Thus, the VoF method can easily capture droplet formation and separation. A large number of molten metal droplets are generated during cutting, and it is more complex and necessitates larger computational effort to describe droplets using the interface tracking method. Lastly, VoF is easily compatible with a phase change model. Both the phase change model and VoF are fixed-grid methods, and combining both models is relatively easy.

3.5.2. Surface tension

Surface tension forces affect the interface between two phases, plasma gas and molten metal in the case of this study. The VoF method doesn't locate the interface

explicitly and the exact shape and location are not easily found. Also, the source term F_s in equation (3.5), which is the surface integral due to surface tension, is not calculated directly. In order to solve this problem, the Continuum Surface Force model (CSF) of Brackbill et al. [76] is introduced.

$$F_s = \sigma_t \kappa_c \nabla \alpha \tag{3.26}$$

Where σ_t is the surface tension coefficient, κ_c is the curvature of the interface, and the curvature is calculated as,

$$\kappa_c = \nabla \cdot \left(\frac{\nabla \alpha}{|\nabla \alpha|} \right) \tag{3.27}$$

For a variable surface tension force, an additional term should be considered. It should be noted that this source term for surface tension (equation (3.27)) is considered for only the constant surface tension coefficient. The results regarding the different surface tension coefficients for the iron and the iron oxide will be discussed in chapter 7.

3.6. Molten metal and solid work piece model

3.6.1. Phase Change model

The model for plasma and the model for the interface between the plasma gas and molten metal flow are discussed in sections 3.4 and 3.5, respectively. Another model is needed to capture the interface between the solid work piece and the molten metal during the melting process. When plasma cutting begins, part of the work piece starts melting near the arc attachment through absorption of latent heat due to heat transfer from the high temperature plasma to the work piece. In other words, this melting process is a phase change from the solid to the liquid and is the reverse process of solidification. Thus, the liquid and the solid states of the work piece should also be included in the model. Similar to the model for capturing the interface location between the plasma gas and molten metal flow in section 3.5, capturing the melt front is of primary importance for developing the melting process model. However, unlike the interface between the plasma gas and the molten metal flow, melting of the metal alloys, either including mild steel and stainless steel is not clear and sharp. It is called a ‘mushy zone’, defined as a partially solidified region between entirely solid and entirely liquid regions. The work piece exists as both liquid and solid in this region.

The mushy zone can be observed only for the melting or solidification of metal alloy because the temperature of phase change for a metal alloy is not a specific value as it would be in the case for temperature of phase change of a pure metal. The temperature range for phase change of metal alloy is described in terms of solidus temperature and liquidus temperature. The solidus temperature is the highest temperature at which the

metal alloy is entirely solid. Likewise, the liquid temperature is the lowest temperature at which the metal alloy is entirely liquid. In the case of pure metal, the solidus and liquidus temperatures are the same; however, a metal alloy has separate solidus and liquid temperatures due to the composition of different materials of the alloy. Thus, the mushy zone should be considered in the modeling of the melting process for reasonable simulation results.

Similar to the modeling of two immiscible flows in chapter 3.5, there are two kinds of modeling approaches for phase change with different ways of describing the interface. These methods are the front tracking method and the fixed grid method. A comparison of the two methods is presented in [59]. The front tracking method can be used in situations where the solid/liquid interface is distinct. However, in the case of metal alloy, the mushy zone is generated between the solid and liquid during phase change, and, thus, considerable computational effort is required to describe a distinct interface in the mushy zone using the front tracking method. On the other hand, the fixed grid method is more suitable for developing the phase change model with the mushy zone. The fixed grid method uses a fixed grid and a volume fraction of phases in one computational cell to describe phase change, thus it can easily express a complex interface as a fraction.

For these reasons, the fixed grid method is used in this research. The major fixed grid formulations and solution methods for phase change problems have been previously categorized by Voller et al.[59]. Although there are some differences among fixed grid methods, all of the methods consider the absorption of the latent heat in the energy

equation and the description of solid in the momentum equation in order to capture the phase change. In this thesis, the enthalpy-porosity method [77] is chosen to describe the melting process. In this method, latent heat is included in the enthalpy value for the work piece in the energy equation. Also, the mixture of solid and liquid states is described as a pseudo porous medium, and, thus, the Darcy force term is included in the momentum equation. This term allows making the solid phase become a fluid of very high flow resistance (large Darcy term). The details follow below in the explanation of phase change terms in the governing equation.

3.6.2. Liquid fraction

The isothermal phase change occurs at a certain temperature and it appears in only pure metal. However, in the case of a metal alloy, the solidus temperature and the liquidus temperature are not the same, and, thus, the liquid fraction should be considered as a temperature interval between the solidus and liquidus temperatures during the melting process. The general profile for phase change is not linear, as shown figure 3.8.

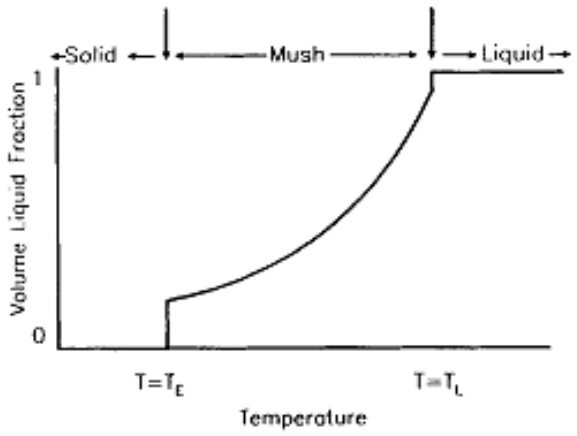

Figure 3.8. General liquid fraction-temperature curve [59]

Also, if the kinetics of the transformation are important during phase change, it is increasingly difficult to calculate the liquid fraction. There are several approaches for the liquid fraction in the mushy zone. In this thesis, the linear profile approach was selected for the liquid fraction, as shown equation (3.28). This simple linear liquid fraction is a function of only temperature and widely used for conduction-dominated phase change, including arc welding or laser cutting.

$$\begin{cases} \gamma = 0 \quad if \quad T < T_s & \text{solid} \\ \gamma = 1 \quad if \quad T_l < T & \text{liquid} \\ \gamma = \dfrac{T - T_s}{T_l - T_s} \quad if \quad T_s < T < T_l & \text{mushy zone} \end{cases} \tag{3.28}$$

In this thesis, a continuous profile is also applied for the liquid fraction [78], and is given by,

$$\gamma = 0.5 \operatorname{erf}\left(\frac{4\left(T - T_m\right)}{\left(T_l - T_s\right)} \right) + 0.5 \tag{3.29}$$

where $T_m = \left(T_s + T_l\right)/2$, and is a mean value of the solidus and liquidus temperature.

3.6.3. Energy equation for the metal phase

The energy equation for the metal phase is derived from (3.16) and $\alpha = 1$,

$$\frac{\partial}{\partial t}\left(\rho C_{p,m} T\right) + \nabla \cdot \left(\rho \vec{u} C_{p,m} T\right) = \nabla \cdot \vec{q} + \frac{Dp}{Dt} + \vec{j} \cdot \vec{E} - L\left(\frac{\partial}{\partial t}\left(\rho\gamma\right) + \nabla \cdot \left(\rho \vec{u} \gamma\right) \right) \tag{3.30}$$

In this equation, the last term in the right hand side includes the liquid fraction term for the metal phase. In order to solve this term with a linear profile of liquid fraction, an iterative method is required to obtain reasonable solutions [58]. Thus, if the residual of liquid fraction is less than the prescribed tolerance, an iteration is finished. For a continuous profile of liquid fraction, the last term in the right hand side can be written in terms of temperature as [78]

$$-L\left(\frac{\partial}{\partial t}(\rho\gamma)+\nabla\cdot(\rho\vec{u}\gamma)\right)=-\rho L\frac{4\cdot\exp\left(\left(\frac{4(T-T_m)}{(T_l-T_s)}\right)^2\right)}{(T_l-T_s)\sqrt{\pi}}\left(\frac{\partial T}{\partial t}+\vec{u}\cdot\nabla T\right) \quad (3.31)$$

Both approaches give reasonable simulation results where the conduction is the primary heat transfer. The energy equation, including the linear profile, requires iterations. However, the continuous profile would reduce the number of iteration because this enables direct coupling of liquid fraction and the energy equation. Thus, the continuous approach was chosen in the plasma arc cutting simulation.

3.6.4. Darcy force for a solid work piece

The Darcy force in equation (3.5) is calculated as,

$$F_p=-A(\gamma)(\vec{u}-U_c) \quad (3.32)$$

And

$$A(\gamma)=\frac{C_D(1-\gamma)^2}{\gamma^3+\varepsilon_n} \quad (3.33)$$

where γ is the liquid fraction, U_c is the cutting speed, which is used to capture the moving work piece, $A(\gamma)$ is the porosity function and C_D is a constant, which is a very large number from 10^4 to 10^8 and is related to the permeability of the porous media. The value ε_n is a small number for the calculation to avoid the denominator from becoming zero. In short, the solved results of the porosity function are classified for three cases. First, the $A(\gamma)$ is a very large constant for the solid state, and the source term F_p is $A(\gamma)$ multiplied by $\vec{u}$. To balance the momentum equation, the velocity $\vec{u}$ should be a very small number, making this phase the solid state. Second, $A(\gamma)$ is zero and the source term F_p is also zero for the liquid state. With $A(\gamma) = 0$, we have the general momentum equation. Lastly, the velocity depends on the liquid fraction for the mushy zone.

3.7. Properties for three phases

Metal properties are given in table 3.1. Constant properties are considered for the model simplification.

Table 3.1. Metal properties for work piece [35,55,56,79]

Properties	
Density of solid phase	7000 kg/m^3
Density of liquid phase	7000 kg/m^3
Specific heat of solid phase	710 J/kgK
Specific heat of liquid phase	710 J/kgK
Thermal conductivity of solid phase	46.1 W/mK
Thermal conductivity of liquid phase	46.1 W/mK
Dynamic viscosity	0.0046 kg/ms
Electrical conductivity	7.7×10^5 S/m
Surface tension coefficient of iron oxide	0.585 N/m
Surface tension coefficient of iron	1.2 N/m
Solidus temperature	1750 K
Liquidus temperature	1800 K
Latent heat	2.47×10^5 J/kg

In this model, the existence of plasma gas, molten metal, and a solid work piece demands phase weighted properties in the governing equations. Thus, the density, the

dynamic viscosity, the thermal conductivity, the electrical conductivity, and the enthalpy are calculated based on the volume fraction of each phase.

$$\rho = \alpha\rho_m + (1-\alpha)\rho_p \tag{3.34}$$

$$\mu = \alpha\mu_m + (1-\alpha)\mu_p \tag{3.35}$$

$$\sigma = \alpha\sigma_m + (1-\alpha)\sigma_p \tag{3.36}$$

$$\kappa = \alpha\kappa_m + (1-\alpha)\kappa_p \tag{3.37}$$

$$h = \frac{\alpha\rho_m h_m + (1-\alpha)\rho_p h_p}{\alpha\rho_m + (1-\alpha)\rho_p} \tag{3.38}$$

where the subscripts m and p represent the metal and plasma gas phase, respectively.

The properties of the plasma gas are already considered in section 3.4 and those are calculated using statistical mechanics and gas kinetics. The properties of the metal phase are calculated using the volume fraction of the molten metal and the solid work piece. The metal phase depends on the melting temperature of the metal, and thus the enthalpy of the metal phase includes the latent heat of fusion.

$$h_m = \frac{\gamma\rho_l h_l + (1-\gamma)\rho_s h_s}{\gamma\rho_l + (1-\gamma)\rho_s} \tag{3.39}$$

$$h_l = c_s T_s + c_l (T_m - T_s) + L \tag{3.40}$$

$$h_s = c_s T_m \tag{3.41}$$

where the subscripts s and l represent the solid and liquid phase, respectively.

Chapter 4

Numerical methods

In chapter 4, numerical methods are discussed in detail in order to solve the mathematical formulations presented in chapter 3. The results obtained from solving these formulations can reflect the physical phenomena of the plasma cutting process; however, it is very difficult or impossible to obtain an exact solution because of the nonlinearity of the general governing equations for fluid flow. In other words, the analytical solution can be obtained for special cases with assumptions to simplify the governing equations like the Stokes flow problem [80]. However, obtaining the analytical solutions from formulations that include electromagnetic equations is much more complex. Therefore, a numerical method is used to obtain the numerical or approximate solutions instead of analytical solutions. In addition, Computational Fluid Dynamics (CFD) [10,81], the numerical analysis for solving the fluid flow problem, was selected to achieve quite accurate solutions in many applications. In this thesis, the Finite Volume Method (FVM), which is one of the methods used to solve partial differential equations using discretization, was chosen for the numerical solution. Moreover, OpenFOAM provides FVM solutions, and the numerical schemes needed, to save time by not

developing codes for FVM. The details follow, as well as an explanation of FVM. Also, the numerical schemes required to obtain solutions from the discretized forms of equations will be discussed. An explanation of every numerical scheme is beyond the scope of this thesis, and, thus, only selected numerical schemes are explained. In addition, a solution procedure will be discussed for coupling the governing equations.

4.1. Finite volume method

The Finite Volume Method (FVM) is a method to approximately solve the partial differential equations, such as the governing equations for fluid flow, by converting them to algebraic equations [10]. The Finite Difference Method (FDM) and Finite Element Method (FEM) are similar to the finite volume method in terms of solving the problem by discretization; however, in the case of the finite volume method, each computational cell has a finite volume, as shown in figure 4.1; thus, the integral form of the partial differential equations is required. For steady simulations, only the spaces of the integral form are divided into a finite number of computational cells. However, for unsteady simulations, like the plasma cutting process in this thesis, both time and space in the integral form are divided into a finite number of time steps and computation cells.

A schematic diagram of the spatial discretization is shown in figure 4.1. The two adjacent cells in the computational domain share one cell face, and thus the cell face values are required for discretization. In this figure, P is the cell center of interest, N is the cell center of the adjacent cell to P, d is the shortest distances between the cell centers P and N, f is the shared cell face between P and N, and S is the surface normal vector of f.

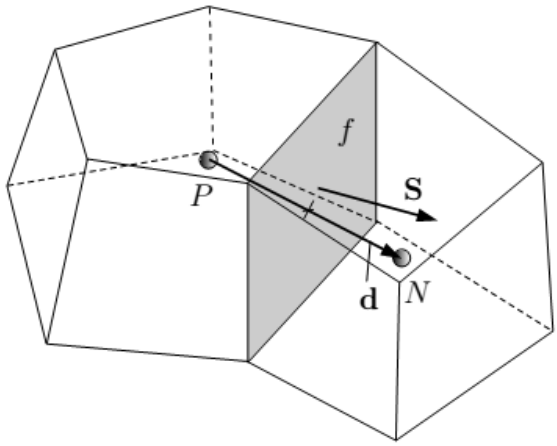

Figure 4.1. Discretization of the computational domain [71]

Also, the Finite Volume Method (FVM) is required to discretize the integral form of the governing equations. The governing equations (3.3)-(3.13) in chapter 3 can be rewritten in the standard form, as follows:

$$\underbrace{\frac{\partial \rho\varphi}{\partial t}}_{Transient} + \underbrace{\nabla\cdot\left(\rho\vec{u}\varphi\right)}_{Convection} = \underbrace{\nabla\cdot\left(\Gamma\nabla\varphi\right)}_{Diffusion} + \underbrace{S_{\varphi}\left(\varphi\right)}_{Source} \tag{4.1}$$

where φ is the dependent variable, Γ is the diffusivity, and $S_{\varphi}\left(\varphi\right)$ is the source term. This standard equation is transformed to the integral form for discretization, and the integral form of the standard equation is

$$\begin{aligned}&\int_{t}^{t+\Delta t}\left[\frac{\partial}{\partial t}\int_{V}\rho\varphi dV + \int_{V}\nabla\cdot\left(\rho\varphi\vec{u}\right)dV\right]dt \\ &= \int_{t}^{t+\Delta t}\left[\int_{V}\nabla\cdot\left(\Gamma\nabla\varphi\right)dV + \int_{V}S_{\varphi}\left(\varphi\right)dV\right]dt\end{aligned} \tag{4.2}$$

The convection and diffusion terms can be converted, using the Gauss's theorem [14], from the volume integral into the surface integrals with surrounding surfaces of the finite volume.

$$\int_{V_p} \nabla\varphi \mathrm{dV} = \int_{S_p} \mathrm{dS}\varphi \approx \sum_f \mathrm{S}_f \varphi_f \tag{4.3}$$

$$\frac{\partial}{\partial t}\int_V \rho\varphi dV \approx \frac{(\rho\varphi)_{(t+\Delta t)} - (\rho\varphi)_t}{\Delta t} V_P \tag{4.4}$$

$$\int_{V_p} \nabla\cdot(\Gamma\nabla\varphi)\mathrm{dV} = \int_{s_p} \mathrm{dS}\cdot(\Gamma\nabla\varphi) \approx \sum_f \Gamma_f \mathrm{S}_f \cdot(\nabla\varphi_f) \tag{4.5}$$

where V_p is the control volume, S_p is the surrounding surface of V_p , dS is the differential of the normal vector of the cell face. (4.3),(4.4), and (4.5) are the discretization form with a gradient, a divergence, and a second order spatial derivative, respectively. For discretization, the cell face values are required, and these are calculated from values of cell center P and values of its surrounding cell using numerical schemes. There are numerous schemes that can be used in OpenFOAM [73]. All of these schemes, however, are not covered in this thesis because it is beyond the scope of the present work, and, thus, only selected discretization schemes will be discussed in section 4.2.

4.2. Discretization schemes

4.2.1. Convection term

The integral form of the convection term needs the cell face values or flux values, but the dependent variables like velocity, pressure, and temperature are stored at the cell center point. By using discretization schemes, the cell face values are obtained from the

cell center values. Then these cell face values or fluxes are used to obtain the dependent values in the next time step through a selected CFD algorithm and calculated values are stored in the cell center point [71,82]. Generally, the convection term is most significant for determining numerical stability. To ensure numerical stability, the upwind differencing scheme is used for most convection calculations, except for some terms in the VoF equation and for the pressure equation. The upwind differencing scheme has first order accuracy, and the cell face values are obtained from the upstream values, as follows:

$$\varphi_{f(F,\text{Upwind differencing})} = \begin{cases} \varphi_P & \text{for} \quad F \geq 0 \\ \varphi_N & \text{for} \quad F < 0 \end{cases} \tag{4.6}$$

where F is the flow direction, φ_f is determined by F. The upwind scheme is numerically very stable and prevents obtaining oscillatory values, but it has numerical diffusion problems. This can result in physically unreasonable results for values with a sharp gradient. Thus, the higher order schemes without numerical instabilities are required for the interface between two fluids or for transonic flows that have extremely sharp interfaces. For this work, the Total Variation Diminishing (TVD) scheme [83], which has second order accuracy and is designed to prevent oscillatory values in higher order schemes, was chosen, and is given by [82].

$$\varphi_f = \varphi_{f(\text{UD})} + \psi_f \left(\varphi_{f(HO)} - \varphi_{f(\text{UD})} \right) \tag{4.7}$$

where ψ_f is the flux limiter, and is a function of consecutive gradient of φ. This scheme is the combination of the upwind and higher order scheme, and the flux limiter. There are several schemes in terms of dealing with flux limiter for preventing the spurious numerical oscillation in OpenFOAM, and above all, the Van Leer and limitedLinear schemes were selected for the convection term in the VoF equation and the pressure equation, respectively. These schemes use a slight different flux limiter, but both schemes have the advantage of TVD-based schemes. By applying these TVD schemes, the interface between the plasma and the molten metal becomes more reasonable.

4.2.2. Diffusion term

Similar to discretization of the convection terms, the discretization scheme is required for the diffusion term. All of the diffusion terms were discretized using a Gaussian linear corrected discretization. This is a second order discretization scheme with a correction for a non-orthogonal mesh.

4.2.3. Source term

For discretization of the source term, the flux or cell face values are not required, and thus the cell center values alone are used for computation. However, when the source term includes dependent variables, the implicit method is used for the source term in order to prevent numerical instability.

4.2.4. Transient term

The transient term in equation (4.2) can be discretized using the Euler explicit, Euler implicit, or Crank-Nicholson method. The Euler implicit and Crank Nicholson schemes are a better discretization methods than the explicit scheme in terms of numerical stability. The Euler implicit method has first-order accuracy and the Crank-Nicholson method has second-order accuracy. The Crank- Nicholson scheme might be better than the Euler implicit scheme due to its second-order accuracy; however, this method has numerical stability issues with the plasma solver in this work. Therefore, the Euler implicit method was chosen for the transient discretization scheme, as follows:

$$\frac{\partial}{\partial t}\int_V \rho\varphi dV \approx \frac{(\rho\varphi)_{(t+\Delta t)} - (\rho\varphi)_t}{\Delta t} V_P \tag{4.8}$$

4.2.5. Multidimensional Universal Limiter for Explicit Solutions (MULES)

For the compressive velocity fields in the phase fraction equation, the multidimensional universal limiter for explicit solutions (MULES) was used in order to guarantee a bounded-solution in OpenFOAM [73]. The flux of the variables was limited by the extrema surrounding the computational cells.

4.3. Sparse matrix solver

The governing equations in chapter 3 are converted from partial differential equations to linear equations using the discretization method. Each linear equation includes one unknown variable for each computational cell. The linear equations for each governing equation are different from each other, but the general form can be expressed as

$$a_P \varphi_P + \sum_{nb} a_{nb} \varphi_{nb} = b \tag{4.9}$$

This can be rewritten in the matrix form as

$$\mathbf{A} \cdot \mathbf{\Phi} = \mathbf{b} \tag{4.10}$$

where the matrix $\mathbf{A}$ is a sparse matrix, including the diagonal coefficients a_P, the non-diagonal coefficients a_{nb}, the array of unknown variables $\mathbf{\Phi}$, and the array of source terms $\mathbf{b}$. Firstly, the variables are assumed to be initial values and then this matrix system is iteratively solved from surrounding variables. Finally, the iteration is stopped when the difference between solutions of two consecutive iterations satisfies a prescribed residual tolerance. There are several sparse matrix solvers for asymmetrical matrices or symmetric matrices in OpenFOAM and two kinds of matrix solvers were selected for this work.

First, the Gauss-Seidel solver was chosen for the majority of the matrix systems. This iterative method required a large number of iterations and therefore is computationally expensive. However, this is a very simple method and is numerically stable, compared to other iterative methods.

Second, the generalized geometric-algebraic multi-grid (GAMG) scheme was chosen for electro-magnetic equations because this iterative solver can increase computation speed. This method makes a coarse mesh from a group of fine mesh. First of all, iteration for a coarse mesh is conducted and then an iteration for a fine mesh is conducted using values of the coarse mesh. Generally, this method is useful for efficient computation, however, it requires more computational effort due to the complexity of this solver.

In addition to this selected matrix solver, the preconditioned conjugate gradient (PCG) with the diagonal-based incomplete Cholesky (DIC) preconditioner for symmetric matrices, the preconditioned bi-conjugate gradient (PBiCG) with the diagonal-based incomplete lower-upper (DILU) preconditioner for asymmetric matrices were included in the built-in sparse matrix solvers. These solvers can be found in [84]. However, there are unexpected numerical problems with this work; thus, these solvers are not used.

4.4. Solution procedure

4.4.1. PISO algorithm

In previous sections, the discretization method and matrix solver for each governing equation was explained. In addition, the CFD algorithm required in order to solve each governing equation is introduced. The SIMPLE (Semi-Implicit Method for Pressure Linked Equations) algorithm [85] for simulations of steady flow and the PISO (Partially Implicit Split Operator) algorithm [86] for simulations of transient flow are two popular algorithms that are widely used for fluid flow problems. In this thesis, the PISO algorithm was selected in order to describe the transient simulation of the cutting process. Also, for plasma flow, additional steps were included in the general PISO algorithm. These are the steps for solving the electro-magnetic equations, the step for updating the plasma properties, and the additional source terms for evaluating plasma characteristics, as shown in chapter 3. The PISO algorithm for the plasma cutting process is outlined in figure 4.2.

The PISO algorithm process for cutting process is as follows:

1. Solve the electro-magnetic equation, the Volume of Fluid equation, and the Energy equation
2. Update properties of computational cells by considering the volume fraction of plasma, molten metal, and the solid work piece
3. Solve the pressure correction equation
4. Correct pressure and velocity
5. Increase time step

As shown in the following flow chart.

Properties are updated after obtaining a new temperature field because the temperature greatly influences the plasma properties. Plasma properties depend on the temperature and the pressure field. In this simulation, the temperature gradient is much steeper than that of the pressure field changed; thus, the temperature greatly influences the plasma properties. Step 3 and 4 are the pressure-velocity coupling, which represent important steps in order to obtain a new pressure field and velocity field. These steps will be discussed in subsection 4.4.2.

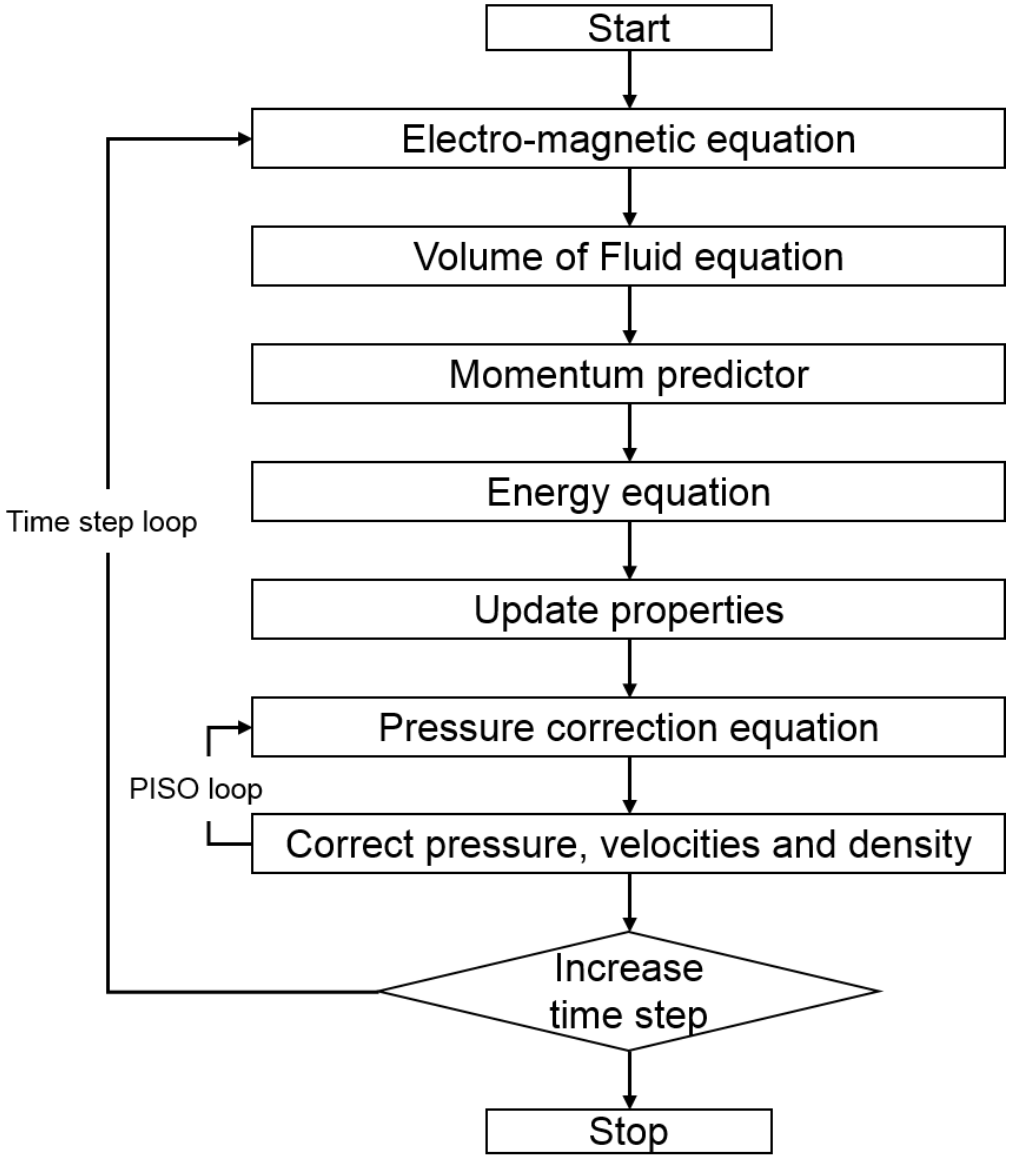

Figure 4.2. Flow chart of PISO algorithm

4.4.2. Pressure-velocity coupling (PISO loop)

The momentum equation has two unknown variables, pressure and velocity, and thus it is not easy to obtain the solutions simultaneously. The PISO algorithm has a pressure-velocity coupling to deal with the pressure and velocity from the momentum equation and the continuity equation, respectively. The first step is defining the momentum predictor. The velocity field is obtained from the previous pressure field. This velocity field is approximatively calculated and does not meet mass conservation. The second step is to solve the pressure correction equation. The pressure correction is a combination of the momentum equation and the continuity equation for each phase. For this step, the continuity equation for each phase is used instead of the general continuity equation due to the need for capturing the mass conservation of each phase correctly. This pressure correction equation is discretized to build the matrix for the pressure field. The last step is to correct the pressure field and the velocity field. Once the accurate pressure field is obtained using the pressure correction equation, then the conservative volumetric fluxes on the cell faces are calculated and the velocity at the cell center is reconstructed by using the new pressure field. The second and third steps are repeated to satisfy the prescribed number of iterations. Generally, a large number of iterations give better results, however it is computationally expensive. Thus, it is important to set up a reasonable number of iterations for the PISO loop.

4.5. Advantages of OpenFOAM

The plasma cutting process model was implemented in OpenFOAM (Open Source Field Operation and Manipulation) [73]. This is a free, open source CFD software package that can solve various numerical problems, including fluid flow with chemical reactions, turbulence, heat transfer, solid dynamics, and electromagnetics. It has several advantages for numerical simulations compared with other commercial packages or in-house codes.

First, it is easy to modify the solvers for partial differential equations. For example, the commercial code FLUENT provides powerful solvers for various physics problems, but is limited for developing a model for plasmas. Plasma modeling needs various governing equations and plasma properties; FLUENT requires additional data to describe such model correctly. Although User Defined Scalars (UDS) and User Defined Functions (UDF) can be used for adding data for the model is still limited in terms of the development of the plasma model, such as discussed in the two-temperature model in chapter 3. But OpenFOAM provides solvers based in C++. The syntax of solvers for governing equations is easy to understand, and the solvers are easily modified for the plasma model needed.

Second, OpenFOAM provides pre/postprocessing utilities, as well as numerical solvers, which save time. OpenFOAM, like commercial codes, provides a grid generator or allows importing grids made by other grid generation tools. This is suitable for generating complex geometries, including the three-dimensional geometries of the actual cutting process. Also, OpenFOAM doesn't require as much time as one would need to

develop one's own CFD-code made by C or FORTRAN. Developing a model requires describing several physical phenomena; such as various governing equations, properties, and components. For CFD calculations, the governing equations are discretized, which is an important but time consuming and difficult process. OpenFOAM, however, provides various built-in methods for discretization, making it easy to do complex modeling work. Therefore, work can focus on studying of the plasma cutting process, rather than on code debugging.

Lastly, complexities of the combined model such as fine grid or small time step require intensive computational calculations. That is, the calculation of combined models takes a long time on a single processor. Fortunately, OpenFOAM allows parallelizing the model and supercomputing resources for parallel computing can be provided by the University of Minnesota Supercomputing Institute (MSI), which greatly helps reduce the run time of the model.

As stated above, OpenFOAM has the advantages of both an open source code and a commercial code. Therefore, OpenFOAM was chosen to develop modeling of the plasma cutting process. OpenFOAM has many solvers for heat and fluid flow problems. However, it is impossible to apply them directly to this work. Thus, a built-in solver for compressible two-phase fluid flow was selected, and additional models for the cutting process were implemented in this solver.

Chapter 5

Plasma cutting process simulation set up

In chapter 3 and 4, mathematical formulation and numerical methods were presented for the plasma cutting process. In order to describe the actual cutting process, the computational domain and suitable simulation conditions, such as boundary and initial conditions, are required. These are quite significant for reasonable simulation results and numerical stability, and thus, they should be carefully considered in the simulations. In this chapter, the computational domain, boundary conditions, and initial treatment for the cutting process model will be discussed.

5.1. Computational domain

A plasma cutting process model was applied to the simulation of a cutting process based on a commercial mechanized cutting torch. As such, the computational domain includes both the plasma torch and the work piece. In other words, simulation was done for the geometry from the swirl ring in the upper part of the plasma torch to the bottom of the work piece (see figure 5.1). The computational domain is roughly broken down into the plasma torch, the standoff distance between the plasma torch and the work piece, and

the work piece with a kerf (cutout portion). The torch geometry was obtained from a Hypertherm HPR 260 torch. The upper part extended up to the swirl ring. The actual nozzle exit of the cutting torch is different from that of the computational domain due to the shield cap for the shield flow. In this simulation, shield flow is neglected; thus, the torch component geometry for shield flow was also not considered in the computational domain. The standoff distance was 3 mm, and was determined by experimental measurement. The thickness of the work piece was 1/2 inch (12.7 mm). The geometry of the work piece was also assumed to have initially on estabilished uniform kerf to avoid a piercing process with the kerf. The piercing process is, thus, slightly different from the general cutting process starting from the edge of the work piece. In the general cutting process, molten metal is blown upwards until the keyhole is made in the bottom of work piece by a piercing process. This is numerically very complex and requires more time steps to describe the process. Therefore, the kerf was taken into account in the initial geometry in order to observe the cutting process instead of the piercing process.

The simulation results of a quasi-steady state will be compared with experimental measurements under the same operating conditions. The measurement of kerf shape is shown in figure 5.2 and it has an asymmetric shape due to the swirl component of the plasma flow. It is noted that simulation of a two-dimensional computational domain can’t correctly capture the cutting process because of the non-symmetric nature of the cutting process. Thus, a three-dimensional computational domain is required in order to obtain reasonable simulation results. Also, a problem with a two-dimensional computational domain will be shown in chapter 7.

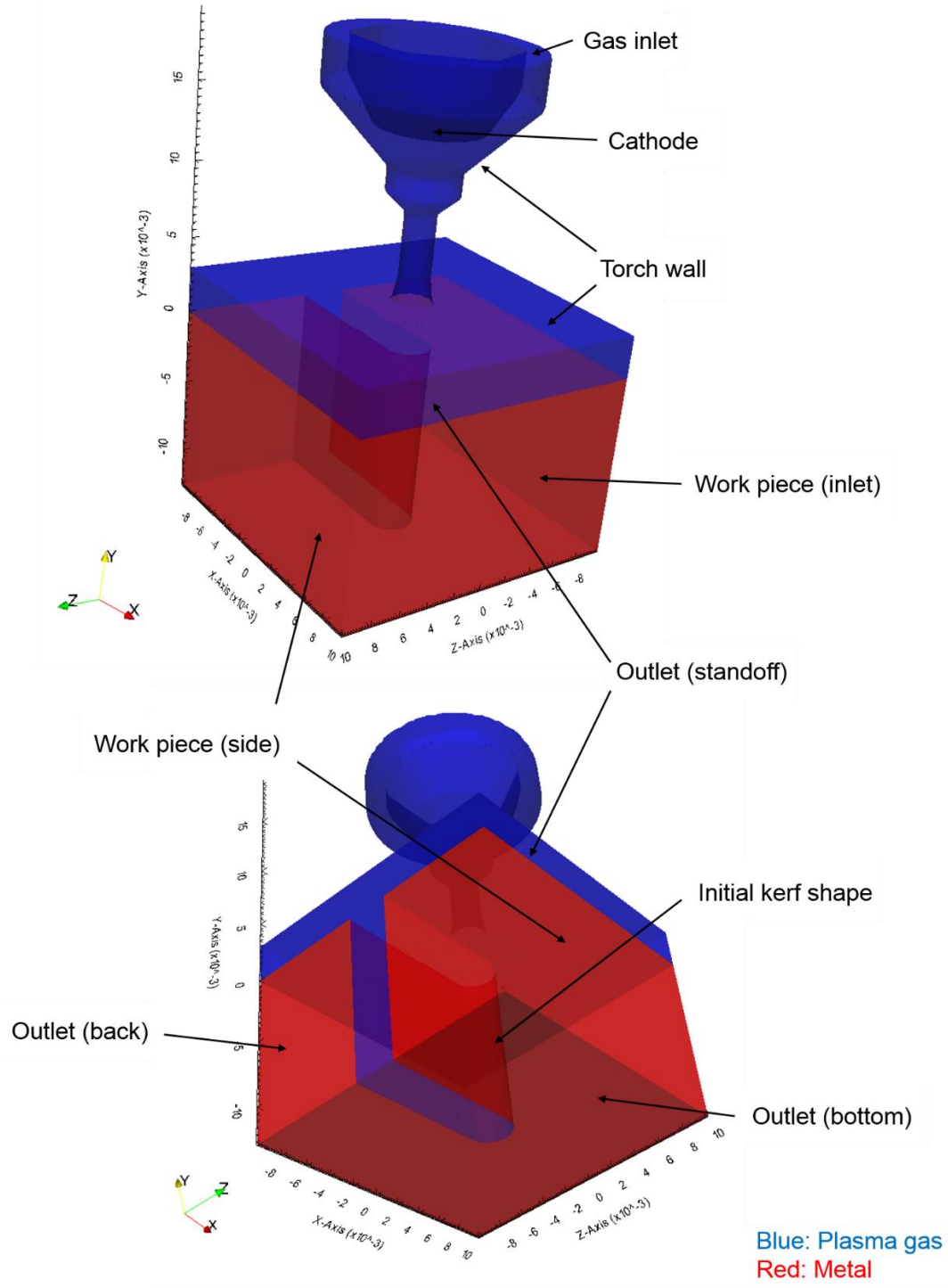

Figure 5.1. Computational domain of cutting process (axes in m×10^{-3})

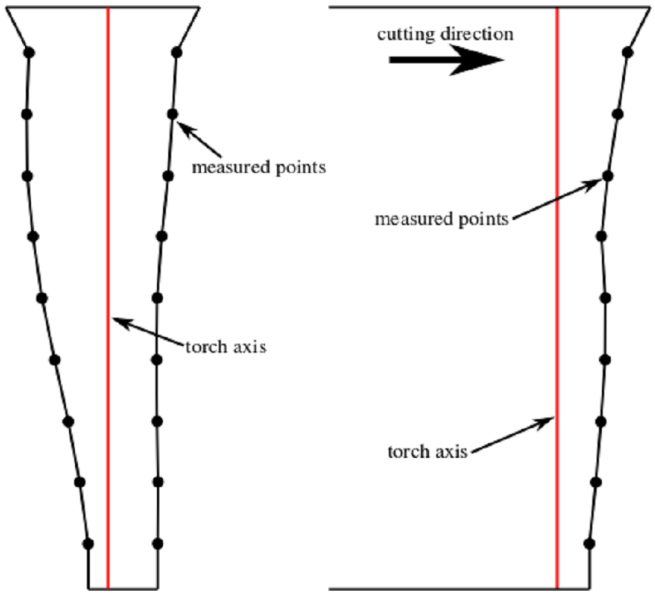

Figure 5.2. Measured kerf geometry under same operation condition [68] (a) view as seen looking down the keyhole of the cut (b) view as see normal to the view of (a)

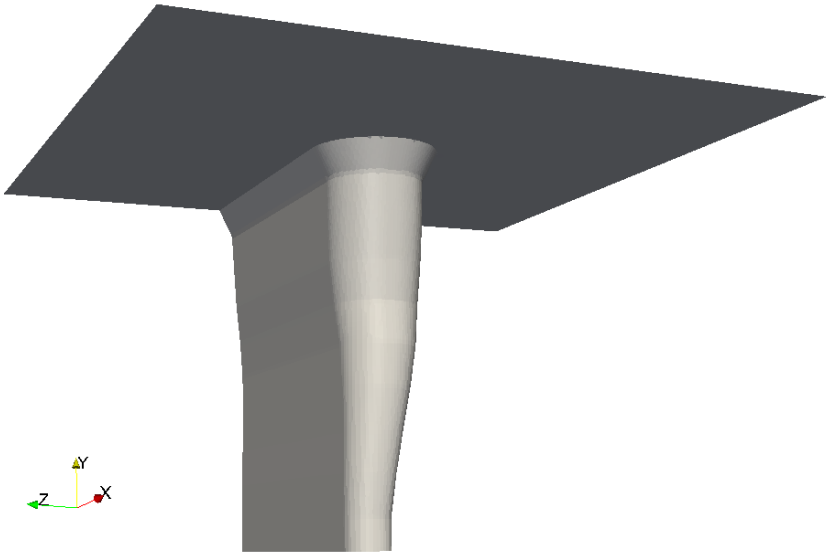

Figure 5.3. Three dimensional geometry of measured kerf

The mesh for the computational domain was generated with Snappyhexmesh [73]. It is a built-in mesh generator in OpenFOAM that generates the final mesh by chiseling into the background mesh made of hexahedra. The advantage of Snappyhexmesh is that refinement can be easily applied to a region of interest such as the interface between the plasma gas and the metal. A fine mesh should be strategically applied in order to prevent a numerical diffusion problem as will be discussed in chapter 7. However, the mesh for the center of the plasma flow is relatively larger than that near the interface because a fine mesh for the plasma flow is less important and it dramatically increases the computation time, according to the Courant number of the simulation. Thus, determining a suitable mesh size is very important for this work, considering the time step and the sharpness of the interface. The number of mesh elements for a fine mesh case was about 1.5 million, and the coarse mesh case is 0.5 million. A comparison between cases with different number ofmesh elements will be discussed in chapter 7.

5.2. Boundary conditions

Table 5.1. Boundary conditions for cutting process model

(locations in figure 5.1)	p	$\vec{u}$	T	ϕ	$\vec{A}$	α	γ
Gas inlet	$\frac{\partial p}{\partial n}=0$	$\vec{u}=\vec{u}_{in,gas}$	$T=T_{in,gas}$	$\frac{\partial \phi}{\partial n}=0$	$\vec{A}=0$	$\alpha=0$	$\gamma=1$
Cathode	$\frac{\partial p}{\partial n}=0$	$\vec{u}=0$	$T=T_{cathode}$ / $\frac{\partial T}{\partial n}=0$	$\frac{\partial \phi}{\partial n}=\frac{j(r)}{\sigma}$	$\vec{A}=0$	$\alpha=0$	$\gamma=1$
Torch wall	$\frac{\partial p}{\partial n}=0$	$\vec{u}=0$	$T=T_{wall}$	$\frac{\partial \phi}{\partial n}=0$	$\vec{A}=0$	$\alpha=0$	$\gamma=1$
Work piece(inlet)	$\frac{\partial p}{\partial n}=0$	$\vec{u}=\vec{u}_{in,wp}$	$T=T_{in,wp}$	$\phi=0$	$\vec{A}=0$	$\alpha=1$	$\gamma=0$
Work piece(side)	$\frac{\partial p}{\partial n}=0$	$\vec{u}=\vec{u}_{in,wp}$	$T=T_{in,wp}$	$\phi=0$	$\vec{A}=0$	$\alpha=1$	$\gamma=0$
Outlet(standoff)	Wave transmissive	Inlet outlet	$\frac{\partial T}{\partial n}=0$	$\phi=0$	$\vec{A}=0$	$\frac{\partial \alpha}{\partial n}=0$	$\frac{\partial \gamma}{\partial n}=0$
Outlet(back)	Wave transmissive	Inlet outlet	$\frac{\partial T}{\partial n}=0$	$\phi=0$	$\vec{A}=0$	$\frac{\partial \alpha}{\partial n}=0$	$\frac{\partial \gamma}{\partial n}=0$
Outlet(bottom)	Wave transmissive	Inlet outlet	$\frac{\partial T}{\partial n}=0$	$\phi=0$	$\vec{A}=0$	$\frac{\partial \alpha}{\partial n}=0$	$\frac{\partial \gamma}{\partial n}=0$

Table 5.1 shows boundary conditions. Boundary conditions for pressure p, velocity $\vec{u}$, temperature T, electric potential ϕ, magnetic vector potential $\vec{A}$, metal fraction α, and liquid fraction γ can be specified in the computational domain (see

figure 5.1). Accurate boundary conditions are required for the results to be close to the actual cutting process. Table 5.1 shows boundary conditions.

5.2.1. Pressure

Generally, pressure or velocity boundary conditions are imposed for inlet or outlet boundaries. For an inlet boundary, the pressure is not imposed. Instead, the mass flow rate is imposed for the inlet boundary and the pressure is calculated by pressure-velocity coupling. Thus, a zero gradient boundary condition is used for both the wall boundary and the inlet boundary.

Atmospheric pressure can be used for the outlets, including the bottom and the back of the work piece and the surrounding of the standoff distance. However, the constant pressure boundary condition for cases with the compressible flow might influence the accuracy of simulation due to wave reflection at the outlet. The wall boundaries are reflective, however the open space such as the outlet would not be reflective. When a constant value is imposed for pressure boundary condition for outlets, the pressure wave might be reflective at the outlets. This is physically unreasonable and, thus, for outlets, a "wave transmissive" boundary condition is used in order to prevent the reflection of waves by the constant pressure boundary condition [68,87]. This boundary condition having a constant pressure with small variation can allow the wave to pass the outlet boundary instead of reflecting from the outlet. The pressure of the outlet is determined by several parameters including the far-field pressure, the distance from the far-field condition, and gas properties.

5.2.2. Velocity

A constant mass flow rate taken from experimental data [88] is imposed for the gas inlet boundary condition. Also, the swirl component is considered for the gas inlet boundary. An angle, θ, of the swirl component is used to calculate the axial velocity and the radial velocity at the inlet boundary and is given by:

$$\mathrm{Tan}\left(\theta\right) = \frac{u_{radial}}{u_{axial}} \tag{5.1}$$

To describe the cutting speed of an actual process, two approaches can be considered. The first is for a moving cutting torch. The other is for a moving work piece. The first approach is closer to reality, however, it is numerically very difficult due to the complex torch geometry. Also, a moving mesh method would require capturing the moving plasma torch. Instead, the moving work piece approach is a very useful method and it doesn't violate the reality of the cutting process. The inlet boundary of a work piece includes the velocity, which corresponds to the cutting speed. The work piece inside a computational domain is also needed to include the cutting speed in the Darcy term in equation (3.32).

Additionally, an "inlet/outlet" boundary condition is imposed for the outlet boundaries. If the velocity vector at the outlet is pointed out of the domain, a zero boundary condition is imposed for the outlet. Moreover, if the velocity vector at the outlet is pointed into the domain, there is a no slip condition imposed for the outlet. Thus, this

boundary condition is very useful in order to prevent a reverse flow at the outlet boundary.

Lastly, for the wall boundaries such as the cathode or the torch wall, the no slip condition is used to capture the viscous flow at a solid boundary.

5.2.3. Temperature

The wall temperature of a plasma torch is usually below the melting temperature of copper in a water cooled system. Actual temperatures might vary along the wall, but this can't be easily applied to the temperature boundary conditions due to the extremely high temperature of the plasma flow. Instead, a constant temperature boundary condition is used at the wall of the plasma torch. Thus, 500 K is imposed for the wall temperature of a plasma torch, except for the hafnium surface in the cathode (see figure 3.1). For the hafnium surface temperature, imposing a melting temperature of 4,000 K is reasonable, however, the constant temperature boundary condition causes a numerical problem due to extremely high temperature gradients of the cell adjacent to the hafnium surface. This affects the energy transfer term of the energy equation due to electron flow in the energy equation. Then the temperature of an adjacent cell increases again due to high temperature gradients. To resolve this problem, an artificially high electrical conductivity is imposed on the cathode surface. Also, a zero gradient temperature boundary condition is imposed on the hafnium surface. These two approaches show very similar results except for the temperature distribution near the cathode. There is no difference in the results near the anode region, which is the region of interest for this study. Thus, either boundary condition can be used in the present model.

For the inlet of the work piece boundary, a constant temperature boundary of 300 K is also imposed. Moreover, a zero gradient boundary condition is imposed to the outlet boundaries (see figure 5.1) because the outflow is dominant, based on experimental research [43]. The outflow of the high temperature of plasma gas would pass through the outlet boundaries, and it is not easy to impose a constant temperature for the outlet boundaries. Instead, the temperature can be calculated using the cells adjacent to the outlet boundaries due to the zero gradient boundary condition. Also, a constant value of the outlet dramatically increases numerical instability, and, thus, it can't be used in the present work.

5.2.4. Electric potential

Electric potential modling is needed to calculate the current density, however, it is difficult to directly impose an electric potential at the cathode surface because the electric potential is not a constant value and depends on given cutting conditions. Instead, imposing a current density distribution at the cathode is an indirect way to easily determine the proper electric potential. The relationship of the electric potential and the current density is given by:

$$\frac{\partial \phi}{\partial n} = \frac{j(r)}{\sigma} \tag{5.2}$$

And, the current density distribution at the cathode is defined by [89]:

$$j(r) = j_0 \exp\left(-\left(\frac{cr}{R}\right)^3\right) \tag{5.3}$$

where j_0 is the maximum current density at the center of the cathode, c is a constant for the width of the profile, and R is the radius of the hafnium insert (see figure 3.1). This type of profile is derived from the assumed profile using experimental results for a tungsten cathode with argon-hydrogen plasma by Zhou and Heberlein [90]. In this work, the total current is 260A. It was obtained by integrating the current density profile from an operating cathode over the hafnium, which is shown in figure 5.4.

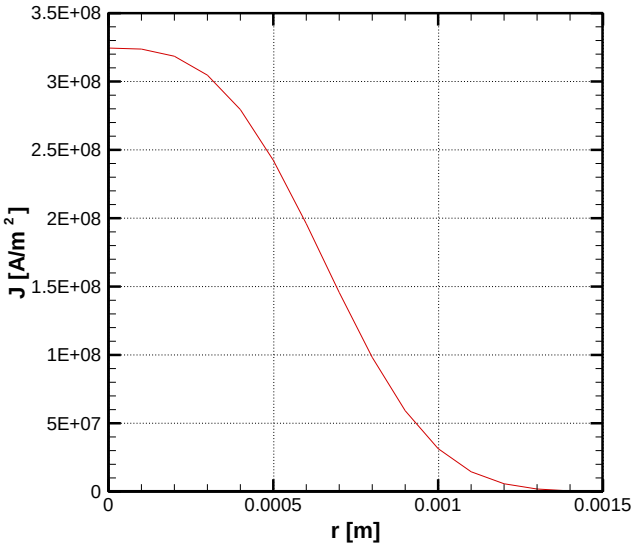

Figure 5.4. Current density profiles at the cathode

A value of zero for the electric potential boundary condition is imposed at the nozzle wall, except for the cathode, which means that the nozzle wall is electrically

insulated. Additionally, a zero gradient for the electric potential boundary condition is imposed at the work piece region that is connected to the ground.

5.2.5. Magnetic vector potential

In thermal plasma modeling, a zero gradient boundary condition is generally imposed for the magnetic vector potential with some boundaries having a value of zero for magnetic vector potential in order to produce the absolute value for magnetic vector potential. For this work, these boundary conditions lead to physically unreasonable results. Instead, a value of zero is imposed at all boundaries, as done in [68]. This approach is not well documented in the literature; however, reasonable results can be obtained using this method. Thus, a value of zero is imposed in this study for the magnetic vector potential.

5.3. Initial condition treatment for numerical stability

The boundary conditions in table 5.1 can't be applied as initial conditions due to a numerical problem related to the low temperature condition. If the initial temperature is low enough inside the nozzle, the pressure inside the torch becomes lower than the atmospheric pressure immediately after the start of the simulation. Subsequently, there is a strong reverse flow through the torch. This is a numerical problem due to the absence of actual physics for the initial processes, because modeling of the arc initiation is not included. Therefore, an artificially high temperature is applied for initial conditions, and initially high temperature is ramped to an actual temperature boundary condition over 1

millisecond. The temperature of the gas region is easily decreased by a ramp-down condition at the boundary. However, the temperature of the work piece region maintains the initially high temperature due to a relatively high thermal capacity. To resolve this problem, a sink term is applied to the work piece region during this period. Thus, the sink term for only the work piece region is included in the energy equation in order to reduce the initially high temperature of the work piece region.

Along with high temperatures for the initial condition, the velocity and electric potential boundary conditions are also increased from zero to the actual conditions during the ramp-up period. This initial treatment creates unreasonable results during the ramp-up period. However, when the simulation reaches a quasi-steady state, the effects of the initial conditions are finally washed out. This is required to resolve the numerical problems and the absence of physical processes at the initial state of simulation.

In conclusion, the numerical simulation was broken down into two separate steps to remove numerical problem brought about by the initial conditions, as shown in figure 5.5. The first step is a simulation with "warm-up" conditions for temperature, velocity, and electric potential to stabilize the plasma flow during the first millisecond. This step doesn't capture the melting process. The second step is simulation of the cutting process with actual boundary conditions after one millisecond. Thus, there is a time period needed to wash out the effect of the "warm-up" conditions and obtain the quasi-steady state results.

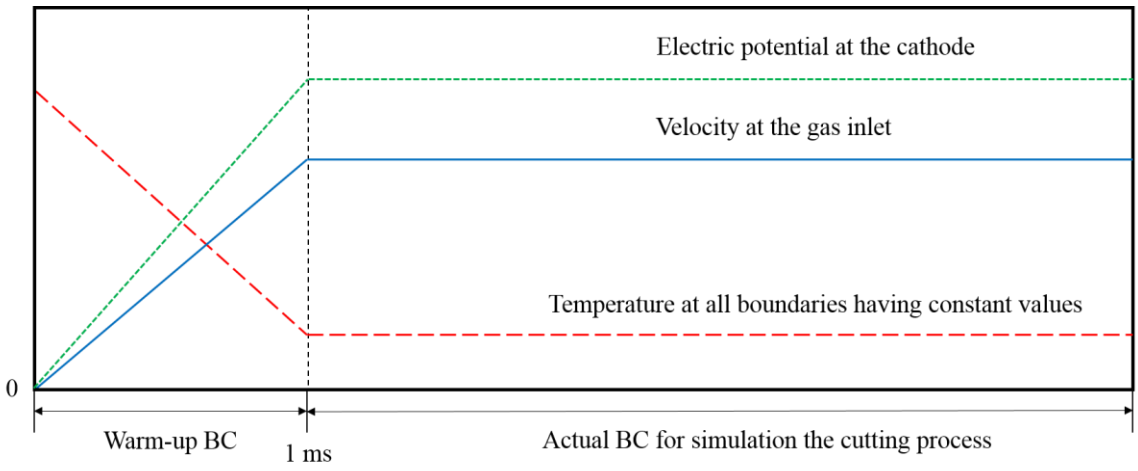

Figure 5.5. Brief description of warm-up and actual boundary condition for cutting process (x-axis)

Chapter 6

Validation of sub-models

The present model was developed to capture physical phenomena in the plasma cutting process, and relevant models were discussed in chapter 3. Previous mathematical models were implemented in OpenFOAM, however, OpenFOAM doesn't include a built-in solver for each phenomenon, such as for plasma flow or melting. Thus, a solver for relevant models should be developed using the syntax of OpenFOAM. As OpenFOAM is readily modifiable, the solvers are easily developed. However, these solvers should be validated.

In this chapter, two different cases were considered for validation. Firstly, a phase change case was considered. The solver for a phase change model is not included in OpenFOAM. The developed solver was validated using a well-known phase change case. Additionally, a compressible two-phase solver, including a plasma phase, is considered for validation. A compressible two-phase solver was already included in OpenFOAM; however, it is used for a general two-phase fluid. Thus, it is necessary to develop a two-phase solver that includes the plasma model to be validated. For this work, the simulation

results for plasma flow used a single-phase solver by Osterhouse [68] are applied. Validation of the cutting process model will be discussed in chapter 7.

6.1. Phase change model

In order to validate the phase change model, the results were compared to experimental or other numerical results for the melting of gallium. In this work, gallium was used as the material for validation because there are various papers with experimental or numerical results for phase change in gallium. Gallium melting simulations were done by Brent et al. [66]. The geometry and operation conditions are used for validation. The geometry descriptors for validation were given in figure 6.1. This is a two-dimensional geometry (88.9mm width and 63.6 mm height) and is a closed system. The temperature of the left wall (311.15 K) is higher than the melting temperature, and the temperature of the right wall (301.45 K) is lower than the melting temperature. The top and bottom walls are insulated, and thus, heat can be transferred through the side walls, but mass can't be transferred through the walls. Properties are given in table 6.1, and constant properties are used for the simulation. The same mesh size (42*32) was used for a comparison of results between the simulation and experimental data.

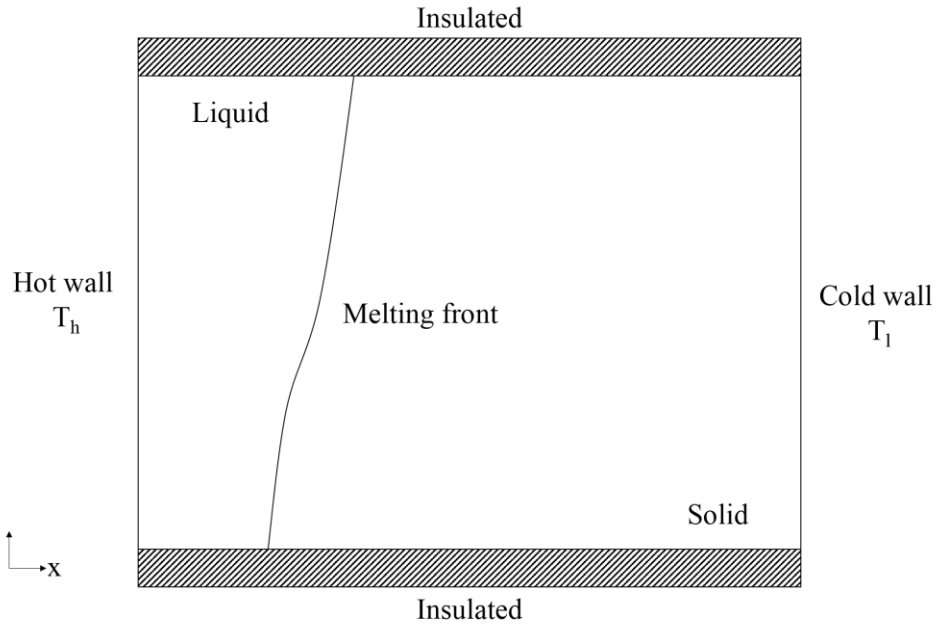

Figure 6.1. Schematic diagram of gallium melting

Table 6.1. Gallium melting properties

Properties	
Density	6093 kg/m^3
Specific heat	381.5 J/kgK
Thermal conductivity	32.0 W/mK
Dynamic viscosity	1.81×10^{-3} kg/ms
Melting temperature	302.93 K
Thermal-expansion coefficient	1.2×10^{-4} 1/K
Latent heat	80160 J/kg

For a gallium melting simulation, both a liquid fraction with a linear profile and liquid fraction with a continuous profile using an error function were considered [78]. The linear profile is required as an iteration to update the liquid fraction, however, a continuous profile would reduce the computation time by reducing iterations, as discussed in chapter 3.

Figure 6.2 shows the time sequence for a volume fraction of liquid gallium. The temperature distribution of the top part is somewhat higher than that of the bottom part. This is explained by natural convection; the heated liquid gallium is relatively light, and it moves to the top part. If it contacts the melting front, it melts the solid gallium. Finally, cooled liquid gallium moves to the bottom part. The velocity distribution clearly shows the direction of movement for the liquid metal.

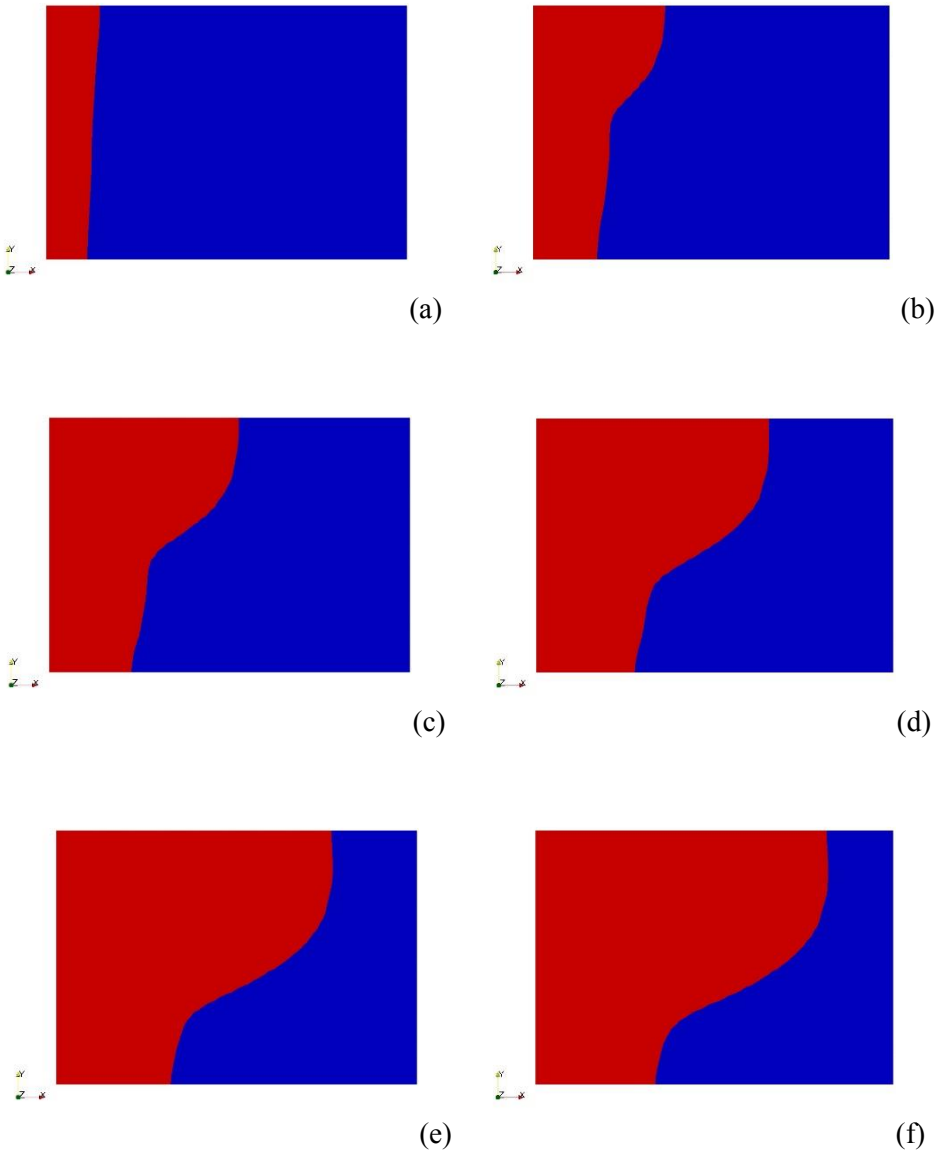

Figure 6.2. Time sequence of volume faction of liquid gallium (red: liquid, blue: solid) (a) 2 [min] (b) 6 [min] (c) 10 [min] (d) 14 [min] (e) 18 [min] (f) 20 [min]

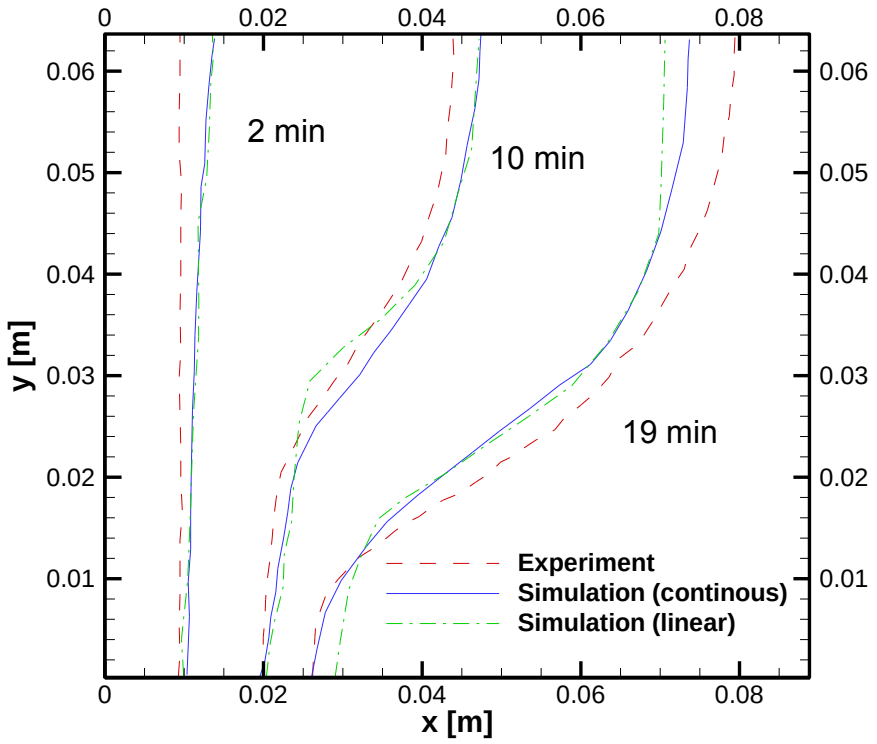

Figure 6.3. Comparison of results for gallium melting

Figure 6.3 shows the experimental results by Gau and Viskanta [91] and the numerical results for the change of liquid fraction with time. There is reasonable agreement between the experimental and numerical results for a continuous profile, which and linear profile demonstrates that the model developed by OpenFOAM describes the melting process well. The slight difference between results is related to the constant properties and the two-dimensional geometry assumed for simulation. Experimental

results were obtained for three-dimensional geometry and temperature-dependent properties.

Additionally, a comparison of results between a linear profile and a continuous profile shows that the continuous profile can be used for an enthalpy-porosity method, including convection. This is a potential advantage for the plasma cutting process. Even a case of only plasma flow is computationally very expensive due to the high velocity and temperature. If the melting process is included in the plasma simulation, it dramatically increases the computational cost by adding iterations for the energy equation. A continuous profile requires, however, fewer iterations than a linear profile. Thus, a continuous profile was selected as a profile for the plasma cutting simulation to reduce the iteration for the melting process.

6.2. Two-phase solver including plasma model

6.2.1. Single-phase and two-phase solver with plasma phase

A comparison of results between a single-phase and two-phase solver with a plasma phase was conducted to validate the two-phase solver for plasma modeling. Although the test case for the two-phase solver is included in OpenFOAM, but this test case only validates for a general fluid flow problem without the plasma model. Thus, a test case for plasma flow is required to validate a solver that includes plasma modeling. A plasma model is implemented in a compressible, two-phase solver called compressibleInterFoam. In order to capture the plasma flow, each momentum and energy equation in this method including, plasma related terms and lookup tables for plasma properties.

For this modified solver, it was not easy to find a relevant test case that included a plasma model. Thus, a modified single-phase solver using rhoPimpleFoam, which is built-in compressible single-phase solver in OpenFOAM, was the only case used to validate the present solver for plasma flow. The differences between the previous single-phase solver and present two-phase solver is that the single-phase solver can’t be used to simulate two-phase flow due to the absence of a model for an immiscible fluid. Thus, a single-phase solver (rhoPimpleFoam) was used only for a compressible single-phase flow. Unlike a single-phase flow solver, a two-phase flow solver can be used for both a compressible single-phase or two-phase flow. When simulation of a single-phase flow is needed, the two-phase solver can be used by simply turning off the second flow in the solver.

A test case for plasma flow in plasma arc cutting was considered for validation. The results of a single-phase flow is documented in [68]. They have already been compared to experimental data in terms of the arc voltage, arc attachment location, and pressure drop through the cutting torch [68]. Simulation results of a single-phase flow solver was in good agreement with the experimental results, and thus, the results of a two-phase flow solver are compared to the results of a single-phase flow solver. The computational domain for validation is given in Figure 6.4.

The cutting torch used in [68] is the same as that of the present work for the cutting process; however, the work piece regions are very different from each other. Due to limitations of the single-phase solver, the molten metal flow can't be captured in [68], and thus, the work piece region was excluded from the computation domain. Further in [68], the interface of the molten metal and plasma flow can't be described by the single-phase flow, and the measured kerf geometry was used to capture the boundary of the plasma flow. Thus, boundary conditions in [68] were slightly different from those of the cutting process model. A no-slip condition was used for velocity and a constant value for temperature was used on the kerf wall. Both Local Thermodynamic Equilibrium (LTE) and two-temperature plasma model are used for validation. In the case of two-temperature model, the electron temperature boundary condition as well as the heavy species temperature boundary condition are required.

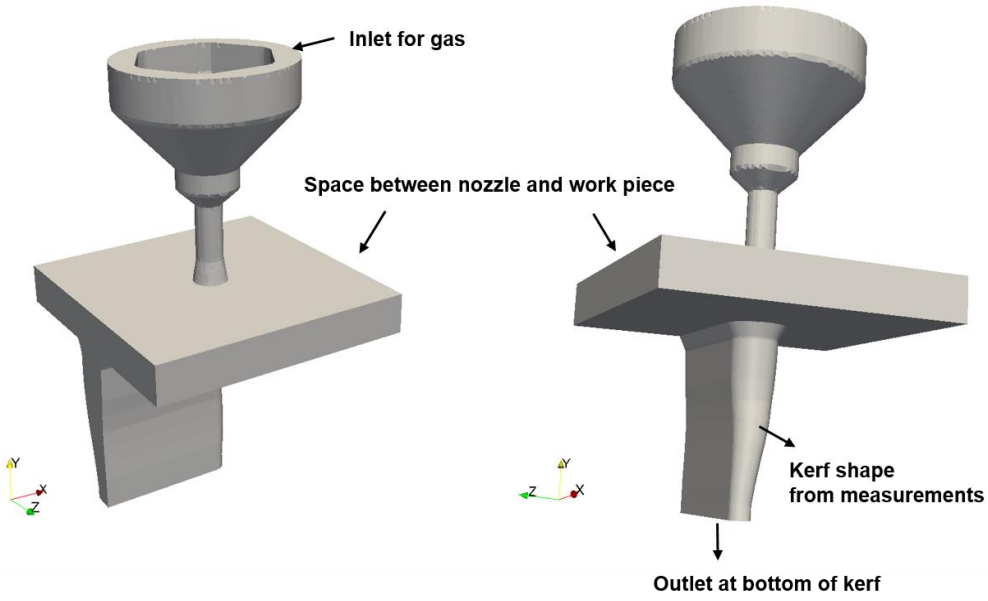

Figure 6.4. Computational domain for validation of two-phase solver

6.2.2. Comparison between the single-phase solver and two-phase solver

The figures 6.5, 6.6 and 6.7 show the simulation results of a two-temperature model between a single-phase solver and a two-phase solver. This time is 5 milliseconds. Although the dependent variables still have small changes with time, it was considered as having reached a quasi-steady state at this time. The results were very different from each other, and particularly, the plenum pressure of the two-phase solver was much higher than that of the single-phase solver or the experimental data. For the two-phase solver, the temperature and velocity near the nozzle wall were higher. Moreover, the electric arc in the two-phase solver was less constricted, which makes the arc attachment on a work piece more diffuse. All of the results that included the plasma torch and the work piece region were physically unreasonable in the two-phase solver. One finding from these simulation results is that unphysical plenum pressure affects other simulation results due to plasma properties that are dependent on pressure. Thus, the pressure correction equation should be modified because the pressure field is incorrectly determined by this equation in the solver.

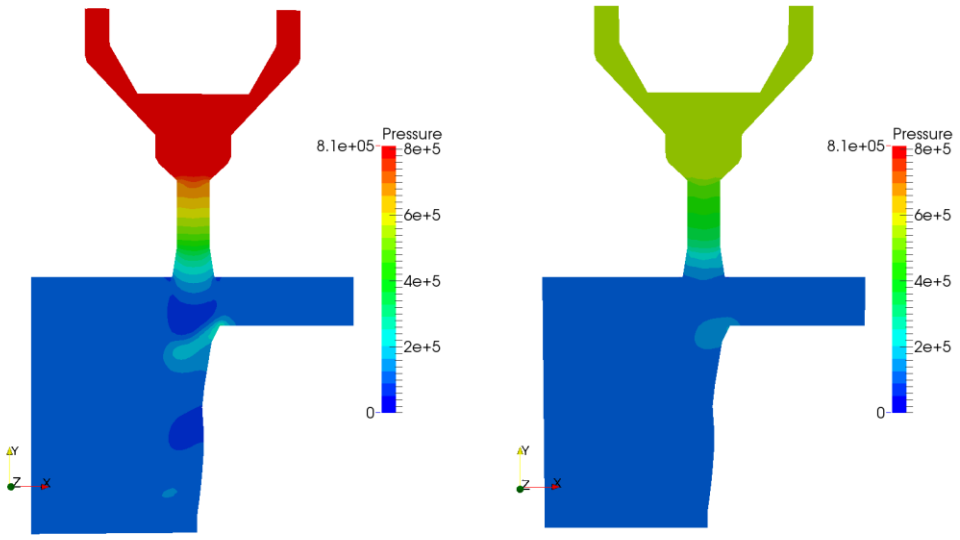

Figure 6.5. Comparison of pressure [Pa] plots between the two-phase solver (left) and the single-phase solver (right)

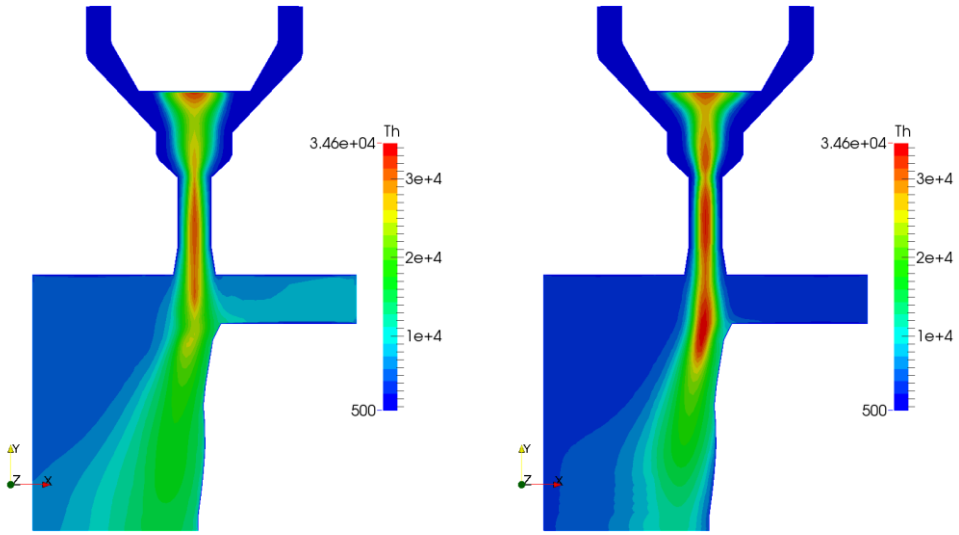

Figure 6.6. Comparison of heavy species temperature [K] plots between the two-phase solver (left) and the single-phase solver (right)

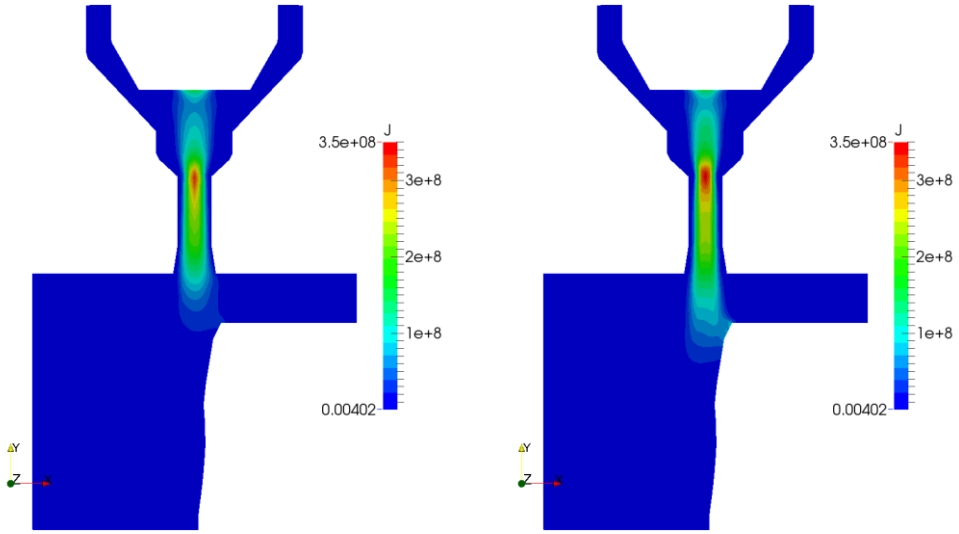

Figure 6.7. Comparison of current density [A/m^2] plots between the two-phase solver (left) and the single-phase solver (right)

6.2.3. Modified pressure equation in a two-phase solver

The single-phase solver and two-phase solver use the same algorithm for an unsteady compressible flow; however, the pressure equation of the two-phase solver is slightly different from that of the single-phase solver. In the two-phase solver, the continuity equation for each phase is combined with the momentum equation to consider the very large phase density differences of typical multi-phase fluid problems. The original pressure equation is solved explicitly with a correction term, given by:

$$\frac{\partial}{\partial t}(\rho_i)+\vec{u}\nabla\cdot(\rho_i)=\frac{\partial}{\partial t}(\rho_i)+\nabla\cdot(\vec{u}\rho_i)-\rho_i\nabla\cdot(\vec{u})+\text{correction term} \qquad (6.1)$$

However, in the single-phase solver, the pressure equation is solved using a fully implicit method. Thus, equation (6.1) of the two-phase solver has been modified as follows:

$$\begin{aligned}\frac{\partial}{\partial t}(\rho_i)+\vec{u}\nabla\cdot(\rho_i)&=\frac{\partial}{\partial t}(\rho_i)+\nabla\cdot(\vec{u}\rho_i)-\rho_i\nabla\cdot(\vec{u})\\&=\frac{\partial}{\partial t}(\psi_i p)+\nabla\cdot(\vec{u}\psi_i p)-(\nabla\cdot\vec{u})\psi_i p\end{aligned} \tag{6.2}$$

where ρ is the density, $\vec{u}$ is the velocity, ψ is the compressibility (ρ_1 / p), while subscript i stands for the phase of plasma gas or metal phase. Both equations (6.1) and (6.2) are the same mathematical formulation, but the density of equation (6.2) is replaced by pressure and compressibility in order to use the implicit method. The plenum pressure of a modified two-phase solver is computed to be 6.5 atm. Pressure is slightly higher than that of the single-phase solver. However, it can be considered reasonable due to the results of the temperature and current density. The improvement of the modified two-phase solver over the original two-phase solver is shown figure 6.8. The temperature distribution near the nozzle wall is reasonable and the arc attachment is narrow, as shown in figure 6.9.

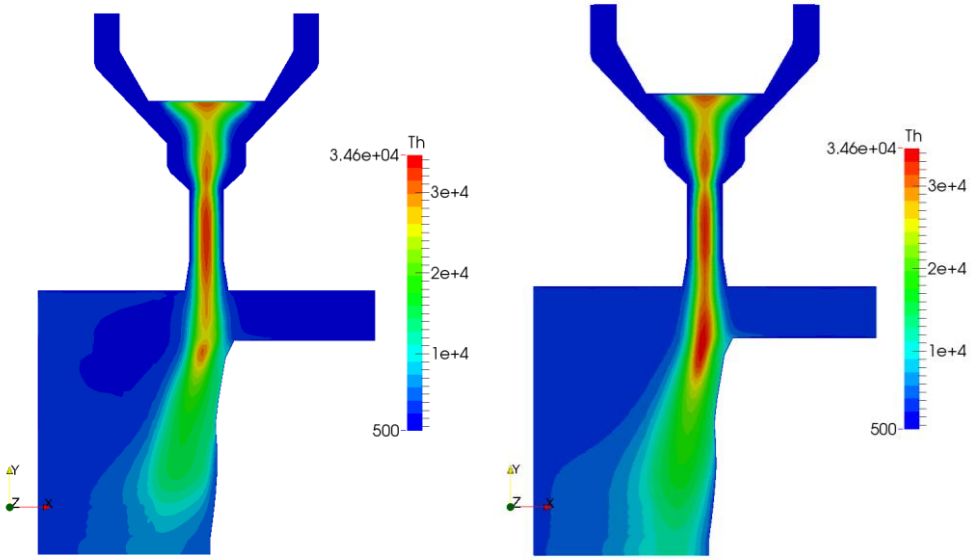

Figure 6.8. Comparison of heavy species temperature [K] plots between the modified two-phase solver (left) and the single-phase solver (right)

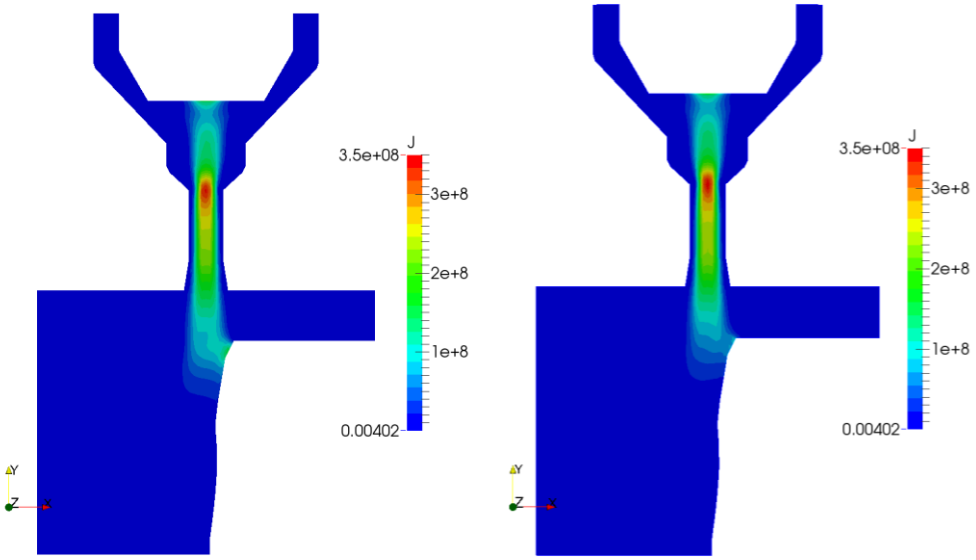

Figure 6.9. Comparison of current density [A/m^2] plots between the modified two-phase solver (left) and the single-phase solver (right)

The temperature in the nozzle bore is plotted in figure 6.10. The temperature near the nozzle wall of the modified two-phase solver is lower than that from the original two-phase solver. Also, the temperature plot of modified two-phase solver is similar to that of a single-phase solver. From these results, we see that the simulation results of the modified two-phase solver are more accurate and they are in good agreement with the results of the single-phase solver.

One limitation of the modified two-phase solver is that a problem exists in parallel computing with the previous version of OpenFOAM. The discontinuity of variables is observed at the interface of the sub-domains. However, this problem was fixed in OpenFOAM 2.4.0.

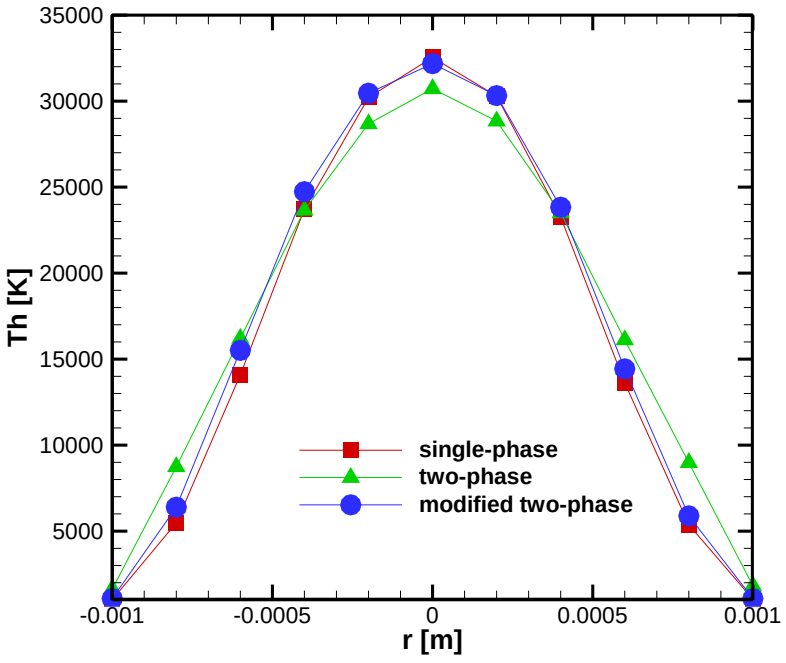

Figure 6.10. Plot of temperature [K] in nozzle bore

Chapter 7

Results

7.1. Validation

7.1.1. Comparison with experimental data

The simulation results of the cutting process were compared with experimental data under approximately the same operation conditions in order to validate the simulation. It is very difficult to directly compare simulation results and experimental data due to the extremely high temperature and enclosed geometry of plasma arc cutting. Thus, dependent variables such as temperature and velocity can't be easily measured. Instead, plenum pressure, arc voltage, and kerf shape were used for comparison.

When a cutting torch is set up, a proper mass flow rate for the plasma gas is selected and the plenum pressure is determined by selecting a mass flow rate. In order to create the same conditions, the mass flow rate was selected for a velocity boundary condition at the plasma gas inlet and plenum pressure was calculated according to the mass flow rate in the simulation. The plenum pressure of the plasma gas only simulation with a two-phase solver was already discussed in Chapter 6. The simulation, including a work piece region, is also similar to the plasma-gas-only case (see figure 6.6.)

The arc voltage measured experimentally was 145 V, and the simulation results show an unsteady arc voltage of about 160 V. First of all, the unstable plasma arc in the simulation affects the arc voltage. Further, the radiation model is very significant for the arc voltage [68,89]. The effective radius of the net emission coefficient affects temperature and other temperature dependent properties (see figure 3.4). Lastly, the electrode sheath (~ 10 V) was not modeled in the simulation [30], and this can also make a difference. Arc voltage is affected by a combination of several factors. The arc voltage in the simulation discussed above, was considered to be in reasonable agreement with the experimental data.

The simulation results show a transient melting process, and it reaches a quasi-steady state with, small variations, at 13 ms. Thus, the kerf shape at 13 ms was compared with the experimentally measured kerf shape (see figure 7.1). The upper region of the kerf shape showed a huge difference between the simulation and the experimental results. However, the bottom region of kerf shape had only a small difference. The kerf shape in the simulation is affected by the plasma model, the phase change model, and the Volume of Fluid (VoF) method in chapter 3. Among them, the absence of metal vapor in the simulation significantly affects the melting rate. This will be discussed in Section 7.4.

Three different results were compared with experiments in order to validate the present plasma cutting simulation. Although all the simulation results were not exactly equal to the experimental results, due to assumptions in the plasma cutting process model, the results can still be considered reasonable. The model is very useful for

improving the cutting process and for understanding plasma physics through parametric study.

The simulation is affected by operation conditions (including initial or boundary condition in the model), and simplification in the modeling. If the trends or relative values are found in the simulation under different conditions, these can be used to improve the simulation results. Therefore, the rest of the chapter is reserved to discuss different operation conditions of the modeling.

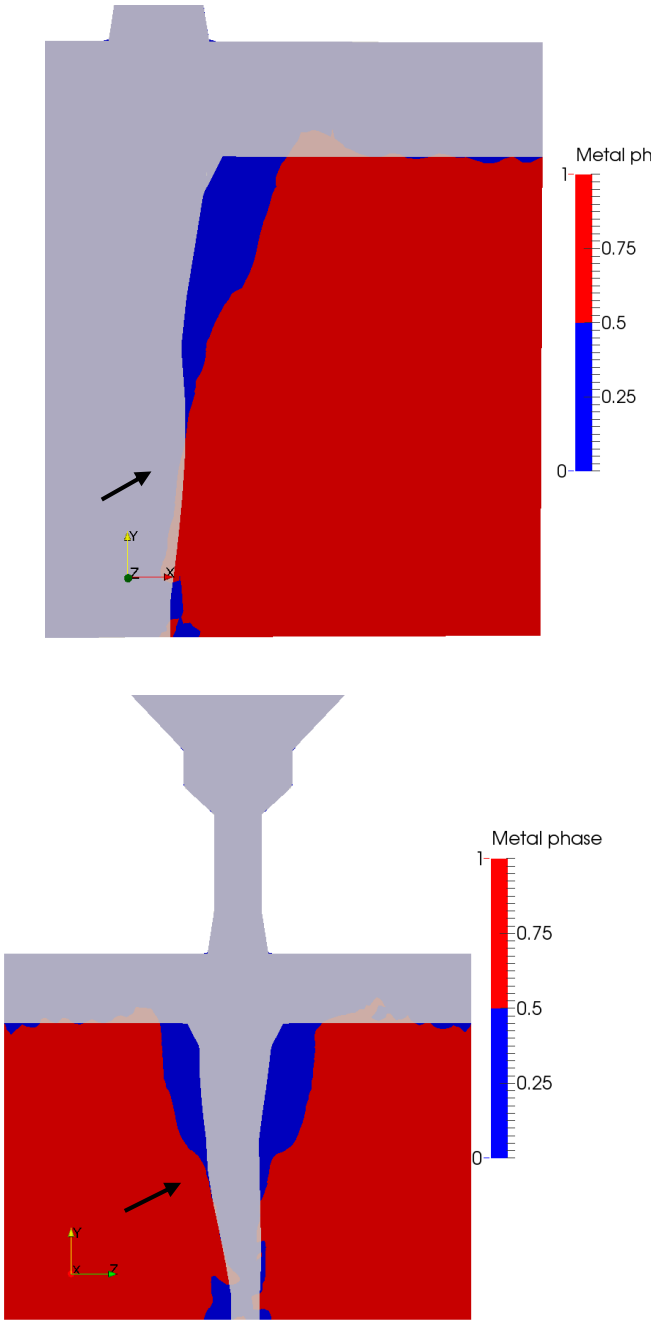

Figure 7.1. Comparison of the kerf front (top) and kerf width (bottom) for simulation results and measurement, simulated kerf (red: metal, blue: plasma gas), measured kerf (gray)

7.1.2. Mesh sensitivity test

A mesh dependency test was also done to study the sensitivity of the simulation to mesh size. Figure 7.2 shows two different results at the same time, and the simulation was performed under the same conditions, except for the mesh size. The number of cells for a fine mesh case is ~ 1,500,000, and the coarse mesh case consists of ~ 500,000 cells. Finer cells are located near the interface between the plasma gas and melt, and the computational cells of the plasma torch are not changed. A slightly higher melting rate is found in the results with a coarse mesh because of the results due to numerical diffusion. In other words, the results with a coarse mesh become more diffuse. Thus, the smearing of the interface between the plasma gas and melt is shown, and the melting rate is also influenced. Additionally, for a coarse mesh, unreasonable waviness on the surface is observed, as shown in figure 7.2, and the interface for a fine mesh case seems to be more reasonable. Although the finer mesh case gives more reasonable simulation results, but the finer mesh case leads to the numerical problem with unsteady plasma flow. Otherwise, the coarser mesh would resolve this problem by the numerical diffusion. Thus, the simulation results with a coarser mesh will be used for the simulation results in this thesis. However, in order to obtain a mesh independent solution, a much finer mesh case is required.

In the present work, the smallest mesh size for the interface is 62.5 μm. This is a very small length scale, but is still not small enough to capture the layer of the molten metal. If the thickness of molten metal is assumed to be of the same order of magnitude as the molten metal droplet size, the layer thickness of molten metal is ~ 100 μm, from

the droplet size measurement [88]. And, calculated molten metal thickness is 40-80 μm [6]. Thus, only one or two cells can be used to capture the molten metal. Thus, mesh size should be decreased to capture the molten metal layer accurately. However, when the plasma gas with high velocity is located in the region with a finer mesh, this dramatically increases the computation time determined by the Courant number. For example, if the cell size is 10 μm and the velocity magnitude of the cell is 5,000 m/s, and required time step for the simulation is 2×10^{-9} s. It is a very small time step and is computationally very expensive. Therefore, additional mesh refining was not tested due to limitations in computation resources.

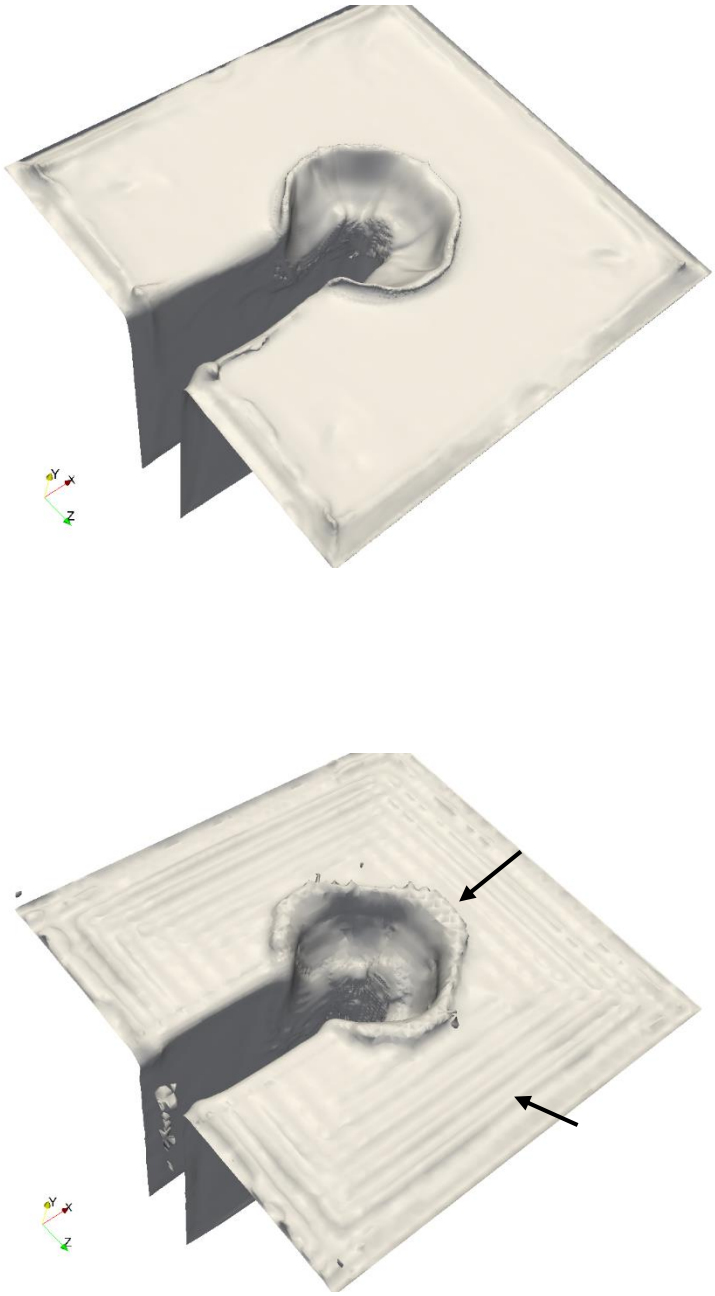

Figure 7.2. Comparison of the kerf shape for fine mesh (top) and coarse mesh (bottom).

The arrow indicates unreasonable waviness and high melting rate.

7.1.3. 2-D and 3-D simulation

Simulation of a two-dimensional axisymmetric coordinate system was also studied with a three-dimensional full geometry. A two-dimensional simulation is beneficial for code development as it reduces the number of mesh elements. However, the measured kerf has an asymmetric shape and not an axisymmetric shape, and it thus can't be captured by the two-dimensional geometry (see figure 5.2). Further, the pressure distribution in a two-dimensional simulation near the kerf region is very unstable due to the narrow passage for the plasma flow, making the computation numerically unstable (see figure 7.3). For the three-dimensional simulation, the open space behind the kerf (keyhole channel) prevents the choked flow problem. Thus, it was necessary to utilize a three-dimensional geometry for the simulation.

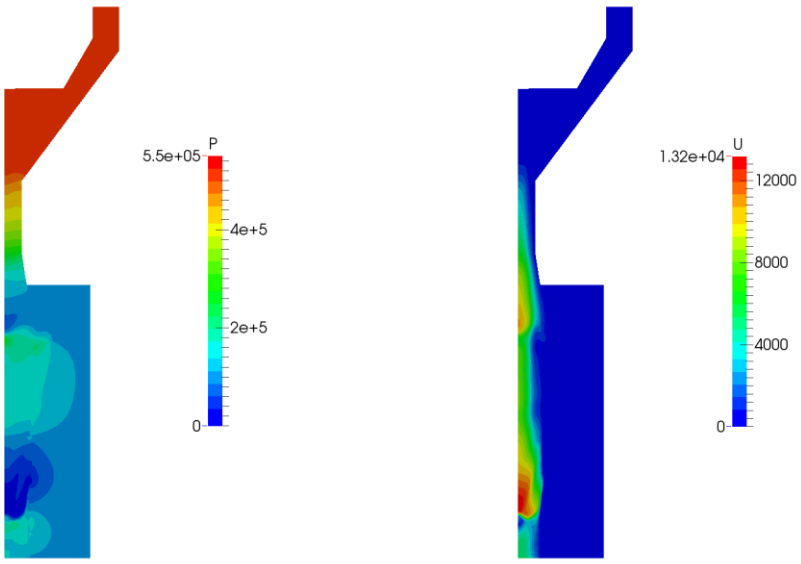

Figure 7.3 Instantaneous distribution of pressure [Pa] (left) and velocity [m/s^2] (right) of the two-dimensional computational domain

7.2. Local Thermodynamic Equilibrium (LTE) results

7.2.1. Melting process

The metal phase distributions in the cross section perpendicular to the y-axis and z-axis, respectively, at t = 1 ms, 4 ms, 7 ms, 10 ms, 13 ms are shown in figure 7.4 and figure 7.5, respectively. The change of inclination of the kerf front is observed in figure 7.4, and the change of kerf width on the top of the work piece is observed in figure 7.5. The melting starts from the upper region due to high Joule heating from the electric arc and conduction, convection and radiation from the plasma flow, and, thus, the kerf surface that is near the arc attachment location receives a huge heat flux. The melting of the lower region is also due to the superheated molten metal from the upper region, and the influence of plasma flow on melting becomes weaker in the lower region.

The kerf shape continuously changes from the start of the simulation. The initial kerf shape is vertical at 1 ms. However, an inclination was observed on the cut front because the high heat flux from the plasma gas is focused onto the upper region of the work piece. The rate of change for melting is very high, between 4 ms and 7 ms, however, the kerf shape was maintained with little variation between 10 ms and 13 ms. These results indicates that the simulation has reached quasi-steady state.

Using the plasma flow cutting model developed, the melting and deformation of the work piece has been successfully simulated. The results show that the upper region of the kerf is much wider than the measured kerf. However, the lower region of the kerf is slightly different from the measured kerf, and the kerf front given by the simulation nearly matches that of the experiment. This indicates the heat flux from the plasma gas is

overestimated in the present work because the melting of the upper region is strongly influenced by the plasma flow and the electric arc. Therefore, improvement of the present plasma model is required for achieving a reasonable melting rate in the upper region.

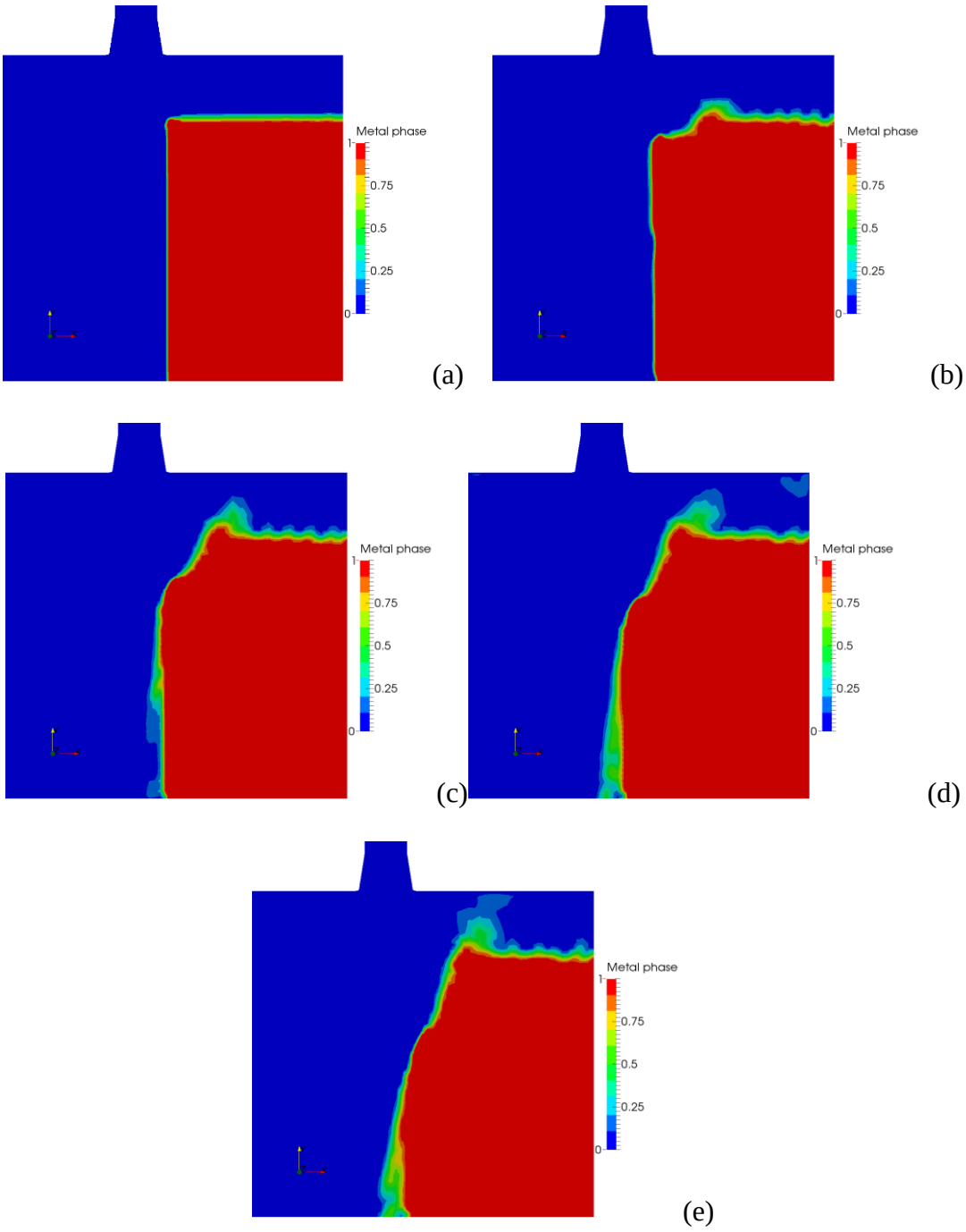

Figure 7.4. Instantaneous distribution of the metal phase through a cross section that is perpendicular to the z axis (a) 1 [ms], (b) 4 [ms], (c) 7 [ms], (d) 10 [ms] (e) 13 [ms]

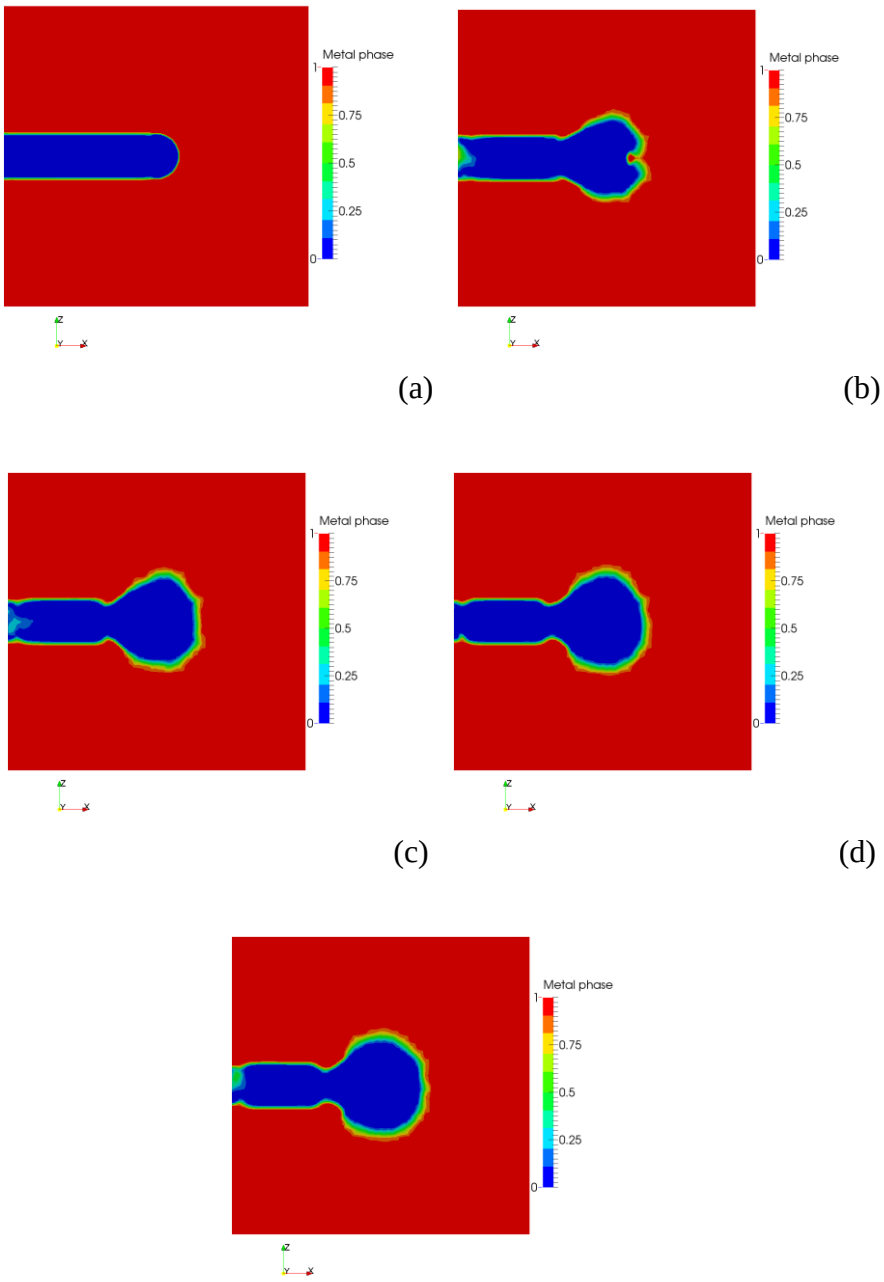

Figure 7.5. Instantaneous distribution of the metal phase through a cross section that is perpendicular to the y axis (a) 1 [ms], (b) 4 [ms], (c) 7 [ms], (d) 10 [ms] (e) 13 [ms]

7.2.2. Energy transfer to the melt

The approximate amount of energy transfer to the melt can be calculated from the simulation by the rate of change of volume fraction of the molten metal.

$$\dot{Q}_{melt} = \rho A_k U_c \left(\int_{300}^{1800} C_p dT + L \right) \tag{7.1}$$

where ρ is the density of the metal, A_k is the area of the melt front, U_c is the cutting speed , C_p is the specific heat of the metal, and L is the latent heat of fusion. A power requirement for melting is 34.3 kW in the simulation, a power for melting is 21 kW, found by using the measured geometry. The required power in the simulation is higher than the power from the measured geometry due to the larger area of the melt front. From these results, more energy is transferred to the melt front, resulting in a wider kerf shape. The total power from the plasma torch is approximately 42 kW from multiplying arc voltage and total current, neglecting the extra energy from by the oxidation reaction. Thus, at least 81.6% of the total power is transferred to the melt front. This efficiency is higher than the efficiency (50%) found by using the measured geometry or the efficiency in the literature of the plasma arc cutting [35]. In conclusion, energy transfer calculated from the simulation, also shows a melting rate that is higher than that for typical plasma cutting.

7.2.3. Temperature and velocity

The temperature fields on a cross section perpendicular to the z-axis at t = 4 ms, 7 ms, 10 ms, 13 ms are shown in figure 7.6. The peak temperature was about 33,000 K and was found at the center of the nozzle due to the highly constricted arc traveling through the narrow nozzle bore. The arc temperature near the top of the work piece drops to 25,000 K. The temperature below the arc attachment region drops significantly to 10,000 K. The temperature distribution indicates that as time goes on, the arc moves counter-clockwise within the nozzle. This is in the opposite direction as the swirl component of the flow in the torch. This unstable temperature distribution may be related to an electro-magnetic kink instability. If so, it depends on the electric current and the induced magnetic field. The kink instability will be discussed in detail in subsection 7.2.4. Further, the change of the kerf shape can affect the temperature field; however, it just creates a wider temperature distribution near the upper region of the work piece. Thus, the unstable arc near the cathode may influence the arc near the kerf.

The velocity fields on the cross section perpendicular to the z-axis at t = 4 ms, 7 ms, 10 ms, 13 ms are shown in figure 7.7. The velocity distribution moves counter-clockwise, and shows similar trends with the temperature distribution. The plasma flow is accelerated by passing through a narrow nozzle bore and by the increased temperature. The peak velocity reaches more than 12,000 m/s near the nozzle exit. When the plasma flow reaches the kerf region, drag forces from the plasma flow blow out the molten metal from the surface and at the same time the plasma flow velocity decreases.

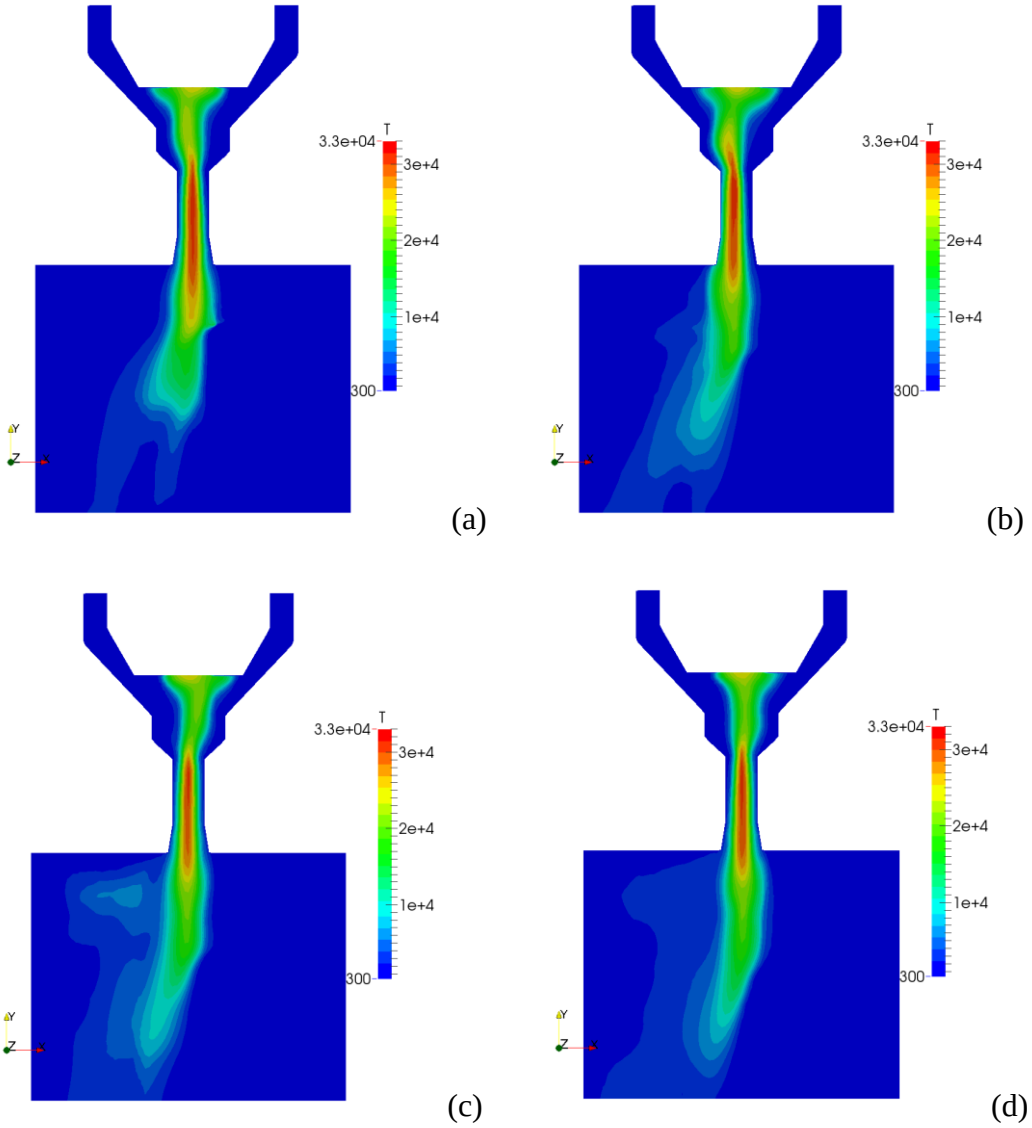

Figure 7.6. Instantaneous distribution of temperature through the cross section perpendicular to the z axis (a) 4 [ms], (b) 7 [ms], (c) 10 [ms], (d) 13 [ms]

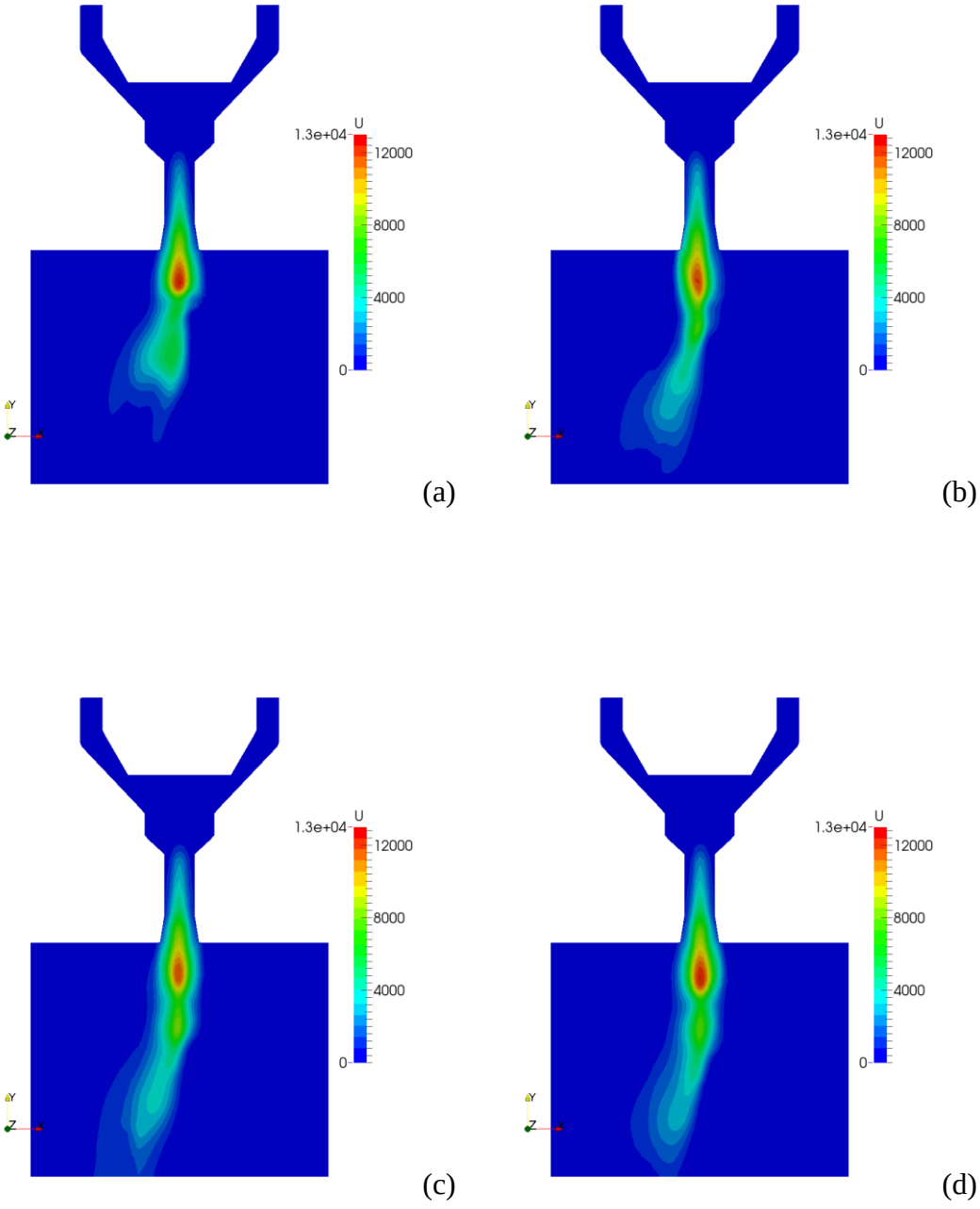

Figure 7.7. Instantaneous distribution of velocity [m/s^2] through the cross section perpendicular to the z axis (a) 4 [ms], (b) 7 [ms], (c) 10 [ms], (d) 13 [ms]

7.2.4. Current density

Current densities plots on the cross section perpendicular to the y-axis between the plasma torch and the work piece at t = 4 ms, 7 ms, 10 ms, 13 ms are shown in figure 7.8. The electrical current density is directly influenced by the temperature because the electrical conductivity of the plasma is determined by the temperature of the plasma. Thus, plasmas with high temperatures have high electrical conductivity and high electrical current density. The current density plots show the formation of an electric arc between the cathode and anode, and high current densities in the arc attachment region on the work piece, which becomes the anode region. At the initial time step, the arc attachment location is near the top edge of the melt front on the work piece. This was considered reasonable. However, as time goes on, an unstable electric arc which is observed near the cathode inside the torch, makes the arc attachment location move around on the work piece. As shown in figure 7.9, arc attachment location is on the kerf front at t = 3 ms, 4 ms however, arc attachment location isn't on the kerf front at t= 7 ms, 13 ms due to the unstable arc inside torch. Although, a narrow nozzle bore with a swirl component of the plasma gas are expected to stabilize the electric arc, an unstable arc is still observed in the narrow nozzle bore region, as shown in figure 7.10. The direction of the arc attachment rotation on the work piece is in the same direction as the arc movement inside the nozzle bore.

As already mentioned in subsection 7.2.3, this unsteady motion may be influenced by the kink instability, which occurs due to a curved plasma column. An induced magnetic field is generated by the arc. Once the arc or a plasma column is curved, the

induced magnetic field on the concave side of the curve is stronger than that on the convex side. This means that a net magnetic pressure is applied to the concave side, and the plasma column curvature increases due to positive feedback.

Arc instability, which was found in the simulation, would be physically reasonable, but the moving arc attachment does not appear to be physically reasonable because the experimental data demonstrate a rather stable arc attachment with small variations [88]. Therefore, improvement of modeling is required to capture the actual arc attachment on the work piece.

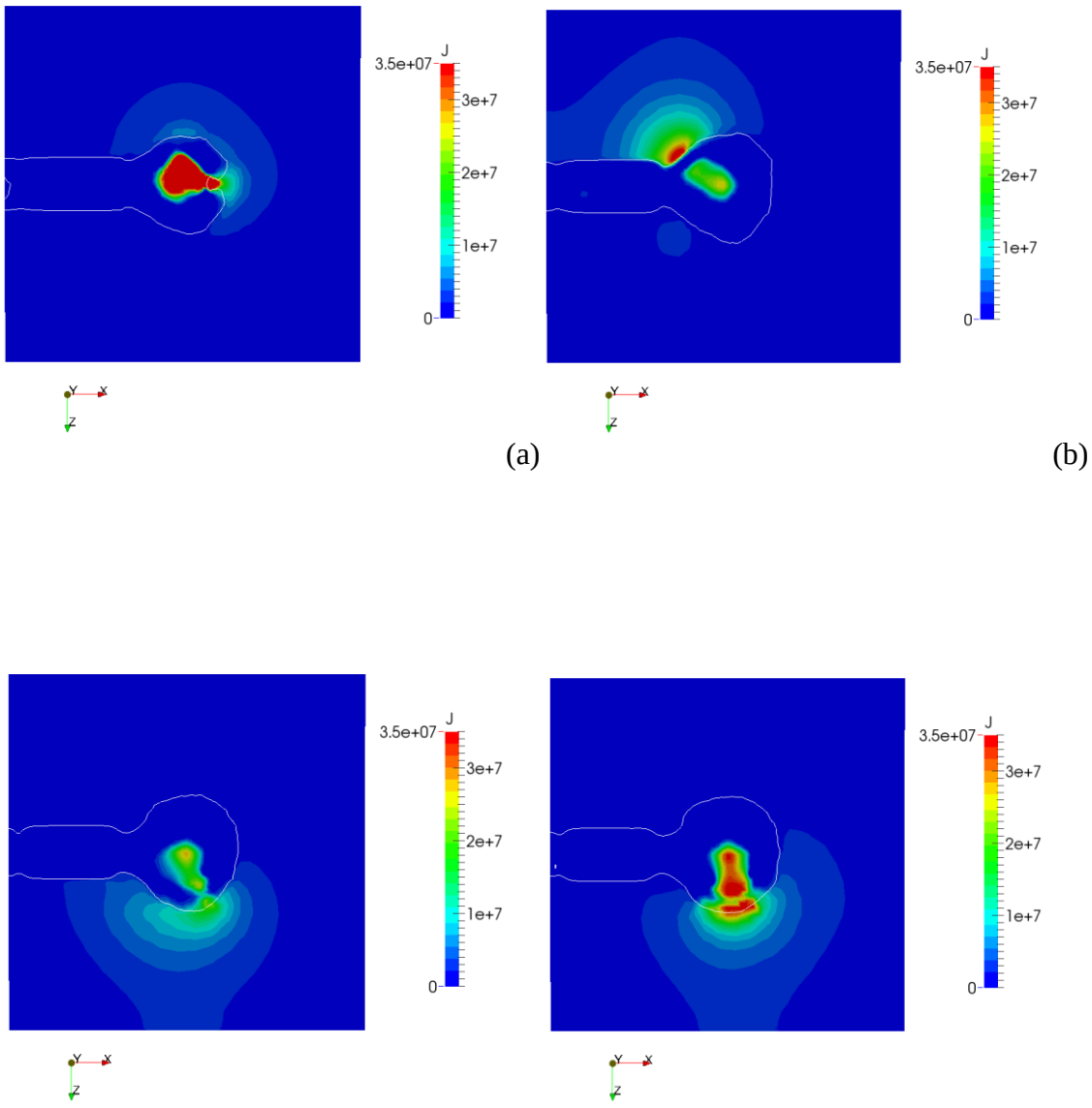

Figure 7.8. Instantaneous distribution of current density [A/m^2] through the cross section perpendicular to the y axis (a) 4 [ms], (b) 7 [ms], (c) 10 [ms], (d) 13 [ms]

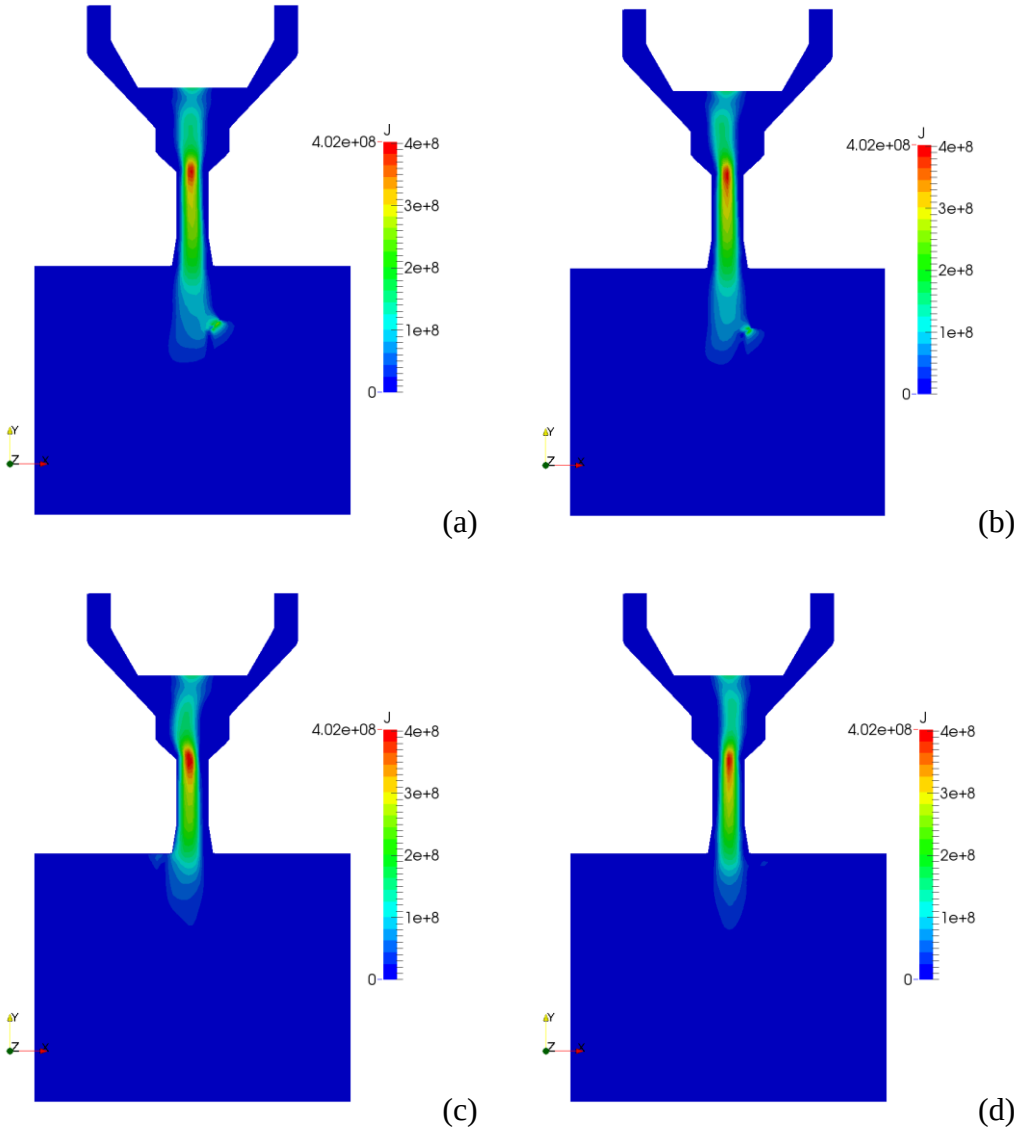

Figure 7.9. Instantaneous distribution of current density [A/m^2] through the cross section perpendicular to the z axis (a) 3 [ms], (b) 4 [ms], (c) 7 [ms], (d) 13 [ms] Arc attachment location is on the kerf front at t = 3 ms, 4 ms however, arc attachment location isn't on the kerf front due to the unstable arc inside torch.

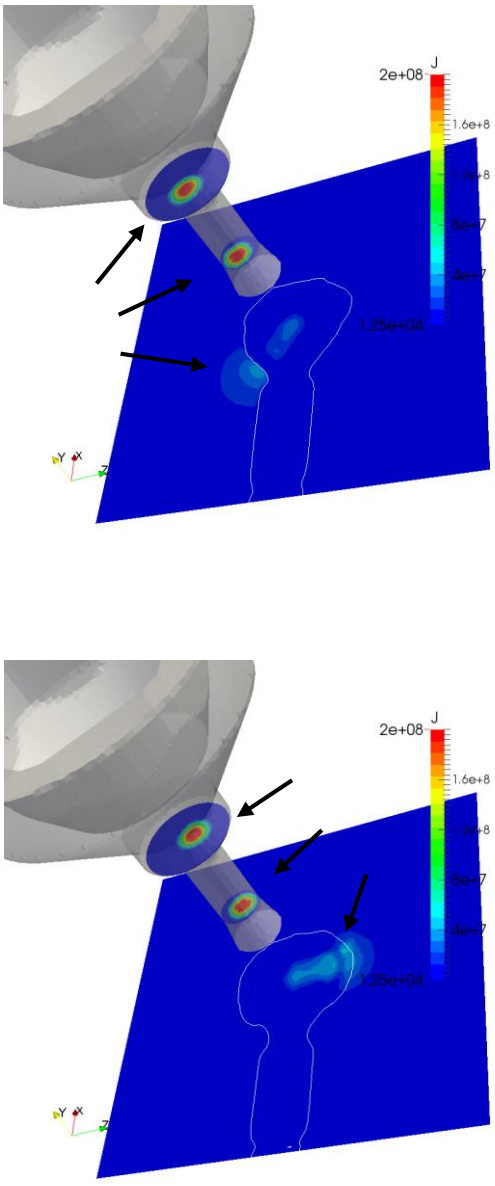

Figure 7.10. Instantaneous distribution of current density [A/m^2] through the nozzle bore at t = 7ms (top), t= 13 ms (bottom) The direction of the arc attachment rotation on the work piece is in the same direction as the arc movement inside the nozzle bore.

7.3. Influence of swirl component

The swirl component for the gas flow is required to constrict the electric arc. A high swirl angle increases the peak temperature, peak current density, and peak velocity, as is shown in [51,52]. In order to investigate the effect of the swirl component on arc stability, simulation was done for a comparison case with gas flows with a high swirl component. The swirl angle of previous simulation results in section 7.2. was 20 degrees, and a simulation with a swirl angle of 60 degrees was done to compare and look for any improvements in arc stability. The high swirl component improves arc stability at 5 ms; however, a moving arc attachment as seen previously was also found for the 60 degrees case. Arc stability is slightly improved using a high swirl component, but the problem wasn't permanently resolved. The unstable arc is observed also for the 60 degrees case, as shown in figure 7.11.

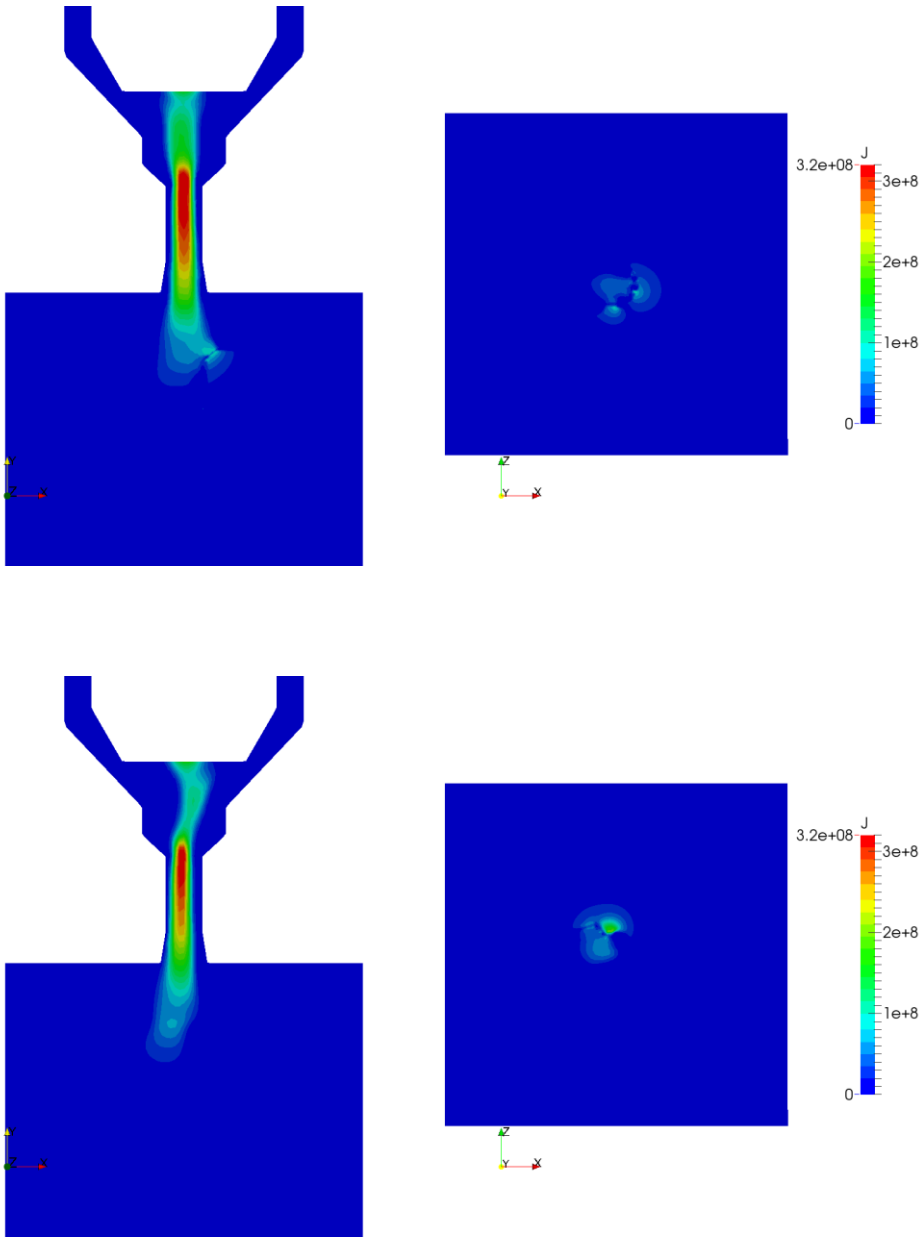

Figure 7.11. Current density plots of cross sections perpendicular to the z axis and to the y axis for 60 degrees swirl angle at 5 ms (top), 6 ms (bottom) Unstable arc is observed at 6 ms.

7.4. Absence of iron vapor

As shown in figure 7.4 and 7.5, melting of the work piece is faster than expected by comparison with a measured kerf shape. In particular, the upper end of the work piece melts much faster, and this melting rate leads to a wide kerf for the upper part of the work piece. In the simulation, the kerf shape is affected by some difficult modeling assumptions. The assumptions were considered in order to achieve numerical stability, but they occasionally violated physical reality. When the work piece melts, most of the solid metal is converted into a liquid phase, as assumed in the present model. Furthermore, although little iron vapor is generated in the actual cutting process, and this was assumed to be a very small amount (~ 1%) [92], and its inventory would be negligible if it were included in the model. However, metal vapor dramatically changes the simulation results, as shown in welding simulation work [61]. Different sizes of the weld pool are shown when including or neglecting metal vapor in the welding process simulation (see figure 7.12). In simulation without metal vapor, the weld pool is much deeper and the size of the weld pool is different from the measured weld pool. Thus, there are other effects than just the mass effect.

The inclusion of metal vapor changes plasma properties near the arc attachment region, and this causes different results. First, the temperature near the kerf is decreased due to the increase in radiation heat loss. Radiation loss is influenced by the net emission coefficient, which is dramatically changed by metal vapor [92]. Furthermore, the metal vapor elongates the arc by increasing the electrical conductivity of the plasma gas near the melt region, and this arc elongation reduces the peak current density, and creates

lower temperatures in this region. The net is a reduction of the amount of heat transfer to the melt front, and the melting rate. Thus, a metal vapor model should be considered to improve the simulation results in the cutting process.

The literature of arc welding indicates that the inclusion of metal vapor dramatically changes the temperature distribution (see figure 7.13); however, the inclusion of vapor has less of an influence in the plasma arc cutting [68]. The metal vapor emitted from the kerf front is confined to a relatively thin boundary layer near the kerf due to the relatively strong advection of the plasma flow because the velocity of plasma flow for cutting is an order of magnitude larger than the velocity of the gas flow in the arc welding. Despite the metal vapor with thin boundary layer, it would influence the distribution of temperature and current density near the kerf front. Additionally, the metal vapor reduces the heat flux by changing the heavy species thermal conductivity in the plasma flow as shown in figure 7.14. This indicates that the inclusion of metal vapor still has the possibility of reducing the melting rate in the cutting process.

The present simulation results indicate that the computed melting rate of the upper region of the kerf is much higher than the actual melting rate. The upper melting region is mainly affected by Joule heating from the electric arc and by conduction, convection and radiation from the plasma flow. Therefore, the change in the plasma flow can affect the melting rate of the upper region of the kerf. In conclusion, the metal vapor should be considered to give a more accurate melting rate as the next step beyond the present work.

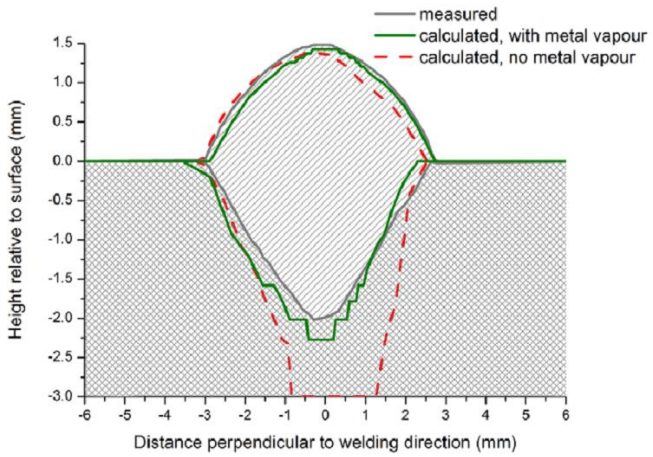

Figure 7.12. Cross section of weld pool computed by including, then neglecting metal vapor [61]

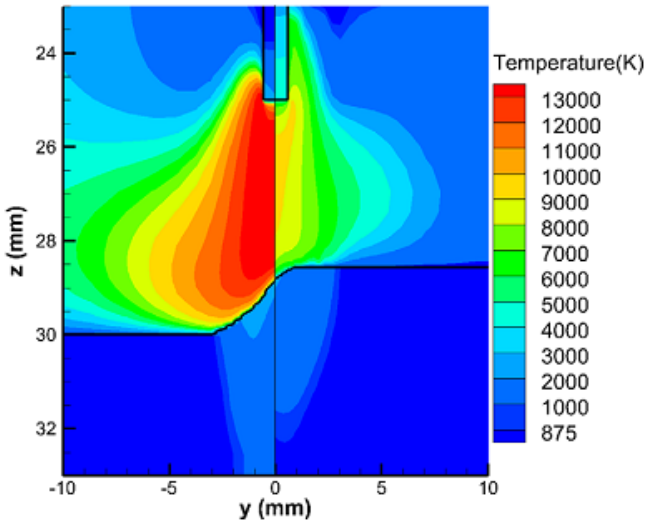

Figure 7.13. Comparison of temperature profile for including (right) and neglecting(left) metal vapor (left) [61] This is a composite picture. Note that the problem is not symmetric about the jet center.

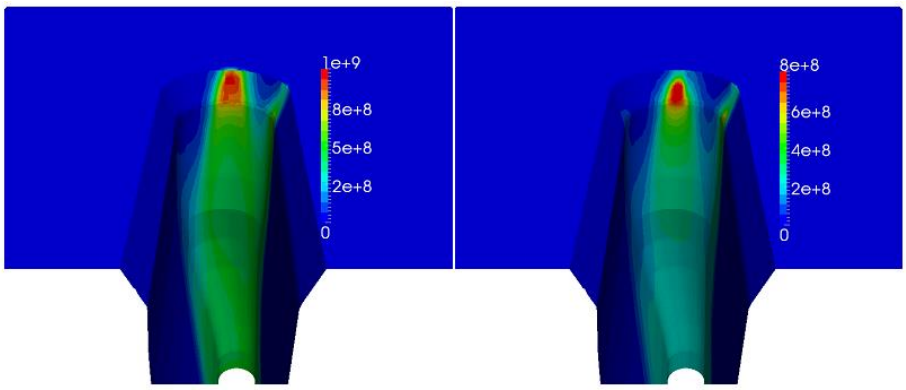

Figure 7.14. Calculated heat flux [W/m^2] on the kerf front for pure oxygen (left) and iron vapor included (right) in the plasma arc cutting [68]

7.5. Influence of oxidation reaction

7.5.1. Influence on surface tension

When oxygen is used with the plasma gas, an oxidation reaction occurs between oxygen and iron. This generates iron oxide with a very thin layer between the plasma gas and the molten metal (iron). This is shown in laser cutting with oxygen [93] (see figure 7.15). The iron oxide has a smaller value for surface tension and viscosity than pure iron; thus, this allows the molten metal to be more easily detached to flow from the work piece. Then, iron oxide is placed between the iron and the plasma gas, and, as such, the surface tension of the iron oxide should be considered in modeling. In order to consider the influence of surface tension, the surface tension of the iron oxide and that of pure iron was compared. The surface tension coefficient of the iron oxide is obtained from [79].

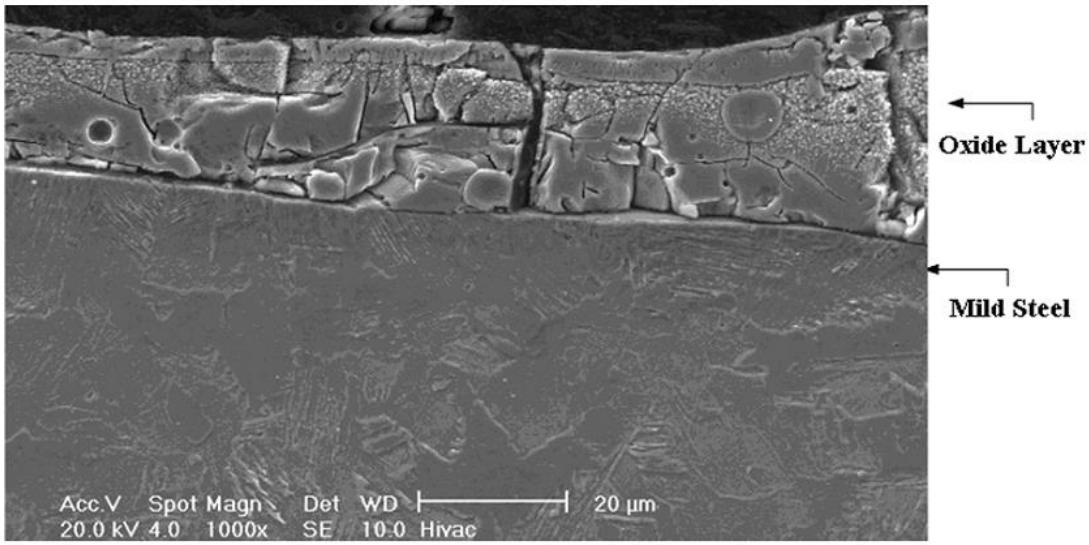

Figure 7.15. Thin oxide layer in Laser-oxygen cutting [93]

Viscosity was not considered because the iron oxide layer is relative thinner than the iron layer in the molten metal region. Figure 7.16 shows the metal fraction under the same conditions except for a change in surface tension. For the present mesh size, it is not easy to capture molten droplets, but the figures definitely show a difference in the melt flow. For the case with surface tension of iron oxide, the surface of the work piece is more complex because the molten metal can more easily detach from the work piece. However, the surface of pure molten metal is relatively smooth, and this means that it is relatively more difficult to remove the molten metal from the surface of the work piece. Though there are noticeable differences of the surface shapes on the molten metal surface, but the overall kerf shape is very similar for the two cases.

The Marangoni effect is another important factor to consider regarding surface tension. A surface tension gradient is generated due to temperature and composition gradients. In arc welding or plasma cutting, a thermal Marangoni effect influences surface tension gradient due to high temperature gradients along the interface near the work piece. Thus, the Marangoni effect is widely mentioned in the literature related to arc welding. It allows the weld pool to have a wider shape. However, it is not well documented for the case of plasma cutting. The melt layer of plasma arc cutting is a few orders of magnitude thinner (~100 μm) than the thickness of a welding pool (3-12 mm) [29], and it is numerically very expensive to capture the thermal Marangoni effect. Thus, though the effect is recognized, it was neglected in the present model.

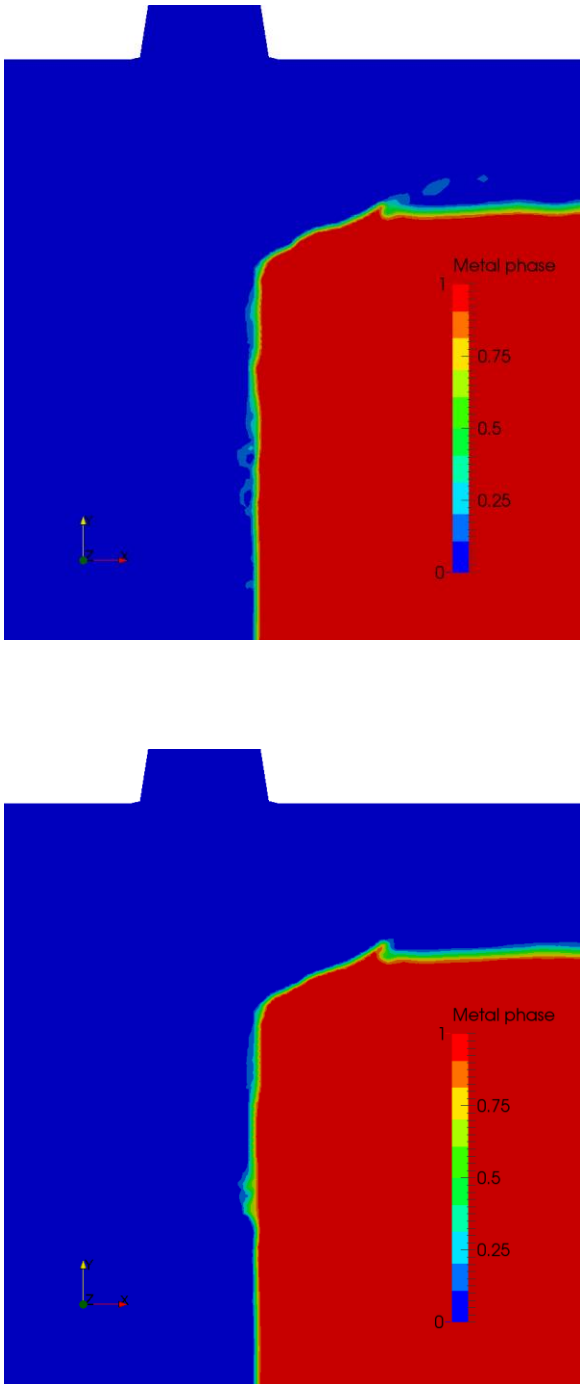

Figure 7.16. Comparison of the effect of surface tension for iron oxide, 0.585 N/m surface tension (top) and iron, 1.2 N/m surface tension (bottom)

7.5.2. Exothermic reaction

In the cutting process, heat conduction from the plasma gas is the dominant mode of heat transfer, but the oxidation reaction produces additional heat to melt the work piece (~20% of total thermal energy) [35,94]. As such, heat generation from oxidation should be considered when oxygen is used as a plasma gas. However, the present model neglects oxidation since it is considered to be a secondary effect and not including it simplifies the model. In order to include an oxidation reaction, the following approach is necessary.

Firstly, the total power released from oxidation is approximately calculated as in [35]. This is given as:

$$\dot{Q}_{oxy} = \frac{0.45 \times D_{O_2}}{M_{O_2}} \times \Delta H \tag{7.2}$$

where M_{O_2} is the molar mass of oxygen, D_{O_2} is the mass flow rate, ΔH is the heat of reaction for $2\mathrm{Fe}+\mathrm{O}_2 \rightarrow 2\mathrm{FeO}$, and the factor 0.45 indicates that only 45% of the oxygen will react because plasma gas with a lower temperature (T < 3500 K) is in contact with the melt and half of the plasma is involved in melting of the kerf front. Although the total power of the oxidation reaction can be calculated by this approximation, the local power released from the oxidation must be implemented in the simulation. This reaction isn't uniform at every interface between the plasma gas and work piece. The chemical reaction calculation depends on the temperature and mass density of oxygen at each location on

the melt face. Thus, an accurate estimation of the heat flux for the mass density of oxygen and the temperature is needed to capture the heat released from the oxidation reaction.

7.6. Influence of the phase change model

In order to describe the solid phase of metal, a Darcy force with a large constant value C was used in equation (3.33) to regulate the flow of the solid portion of the work piece. This is like forcing the metal through a porous membrane. Generally, a number from 10^4 to 10^8 for C was used for the phase change model [66,95,96], but the explanation for choosing a particular number is not well documented in the literature. Especially, a specific value of this number is not shown in the arc welding or laser cutting literature that includes a phase change model. Some papers in the literature indicate that 10^4 to 10^6 can be used [54,55,97].

This large constant number isn't considered important, except for its influence on the melting process. A comparison of different constant values was done by Shmueli et al. [98]. Simulation of the melting process for a Phase Change Material (PCM) with different constant values were investigated, and the optimum number for the PCM was determined by a comparison with experimental results. However, their work can't be directly applied to plasma cutting because the material is entirely different from that of the PCM simulation. Since this number may not be used for this work, several values of C were selected used to test the simulation. Figure 7.17 shows simulation results for 10^6 and 10^8.

This result indicates that the melting rate is reduced for the higher Darcy number, but melting of the upper region is still physically unreasonable, because simulation of the melting process is influenced by multiple factors, such as metal vapor and oxidation. Additionally, a large constant value in the Darcy force is an important factor to determine

the kerf shape. Thus, optimum values are required to improve the cutting model. This is a topic for continued investigation.

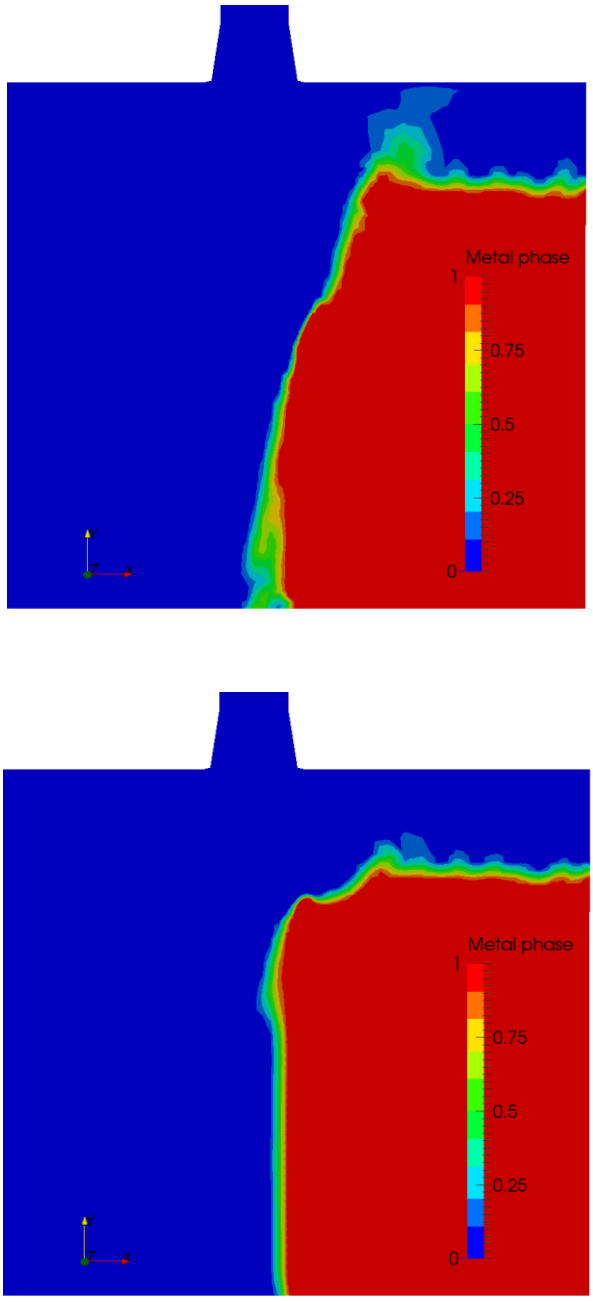

Figure 7.17. Comparison of the large constant value in the Darcy term, 1×10^{6} (top) and 1×10^{8} (bottom)

7.7. Possibility of using the two-temperature model

All simulation results of the cutting process plotted in the thesis were from the LTE model. A cutting process model using a two-temperature model was also attempted with additional terms in an energy equation (3.7) and (3.8) . A two-temperature model has two separate energy equations to capture the thermal non-equilibrium behavior at the arc fringes. This difference in temperature is not present in the liquid metal or solid metal. Although a two-temperature model isn't needed in the metal phase, this two-temperature model must also be applied to the metal phase because the same energy equation should be solved for all the computation domains. That includes the metal phase region. Thus, assumptions were needed to solve the electron energy equation for the metal phase.

Figure 7.18 shows the temperature profile of the two-temperature model near the interface of molten metal and plasma gas. The electron temperature is definitely higher than heavy species temperatures due to a zero gradient boundary condition for the electron temperature at the wall. The temperature in the metal phase is a continuation of the heavy species temperature. However, the electron temperature doesn't physically exist there. Therefore, the electron temperature was assumed to have a zero gradient in the metal phase, as shown in figure 7.18.

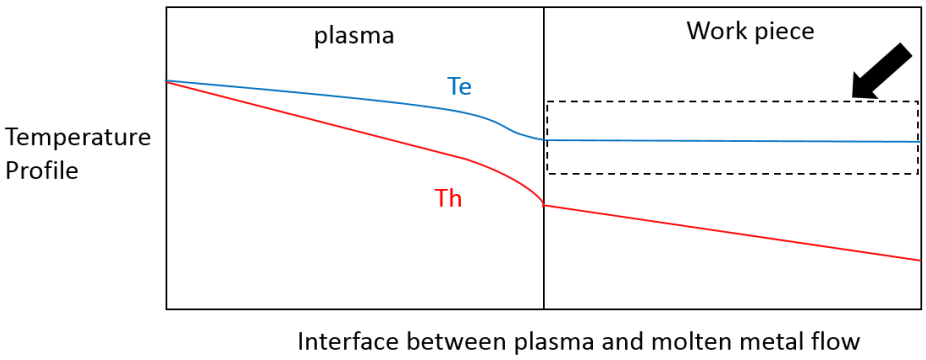

Figure 7.18. Assumed temperature profile in the work piece

In order to make a zero gradient for the electron temperature, the energy transfer term between heavy species and electrons was neglected in the metal phase. Moreover, the boundary condition at the surrounding of the work piece should be a zero gradient. Further, artificially high electrical conductivity was considered to make a flat profile for the electron temperature.

The cutting process model, using the two-temperature assumption was developed. When this model is used to simulate a plasma-gas-only case, it works without a problem, as shown in sub-model validations in chapter 6. An uncertain numerical problem is observed when the metal phase is included in the computational domain. This indicates that this problem is related to the assumed electron temperature equation for the metal phase. Although the results are not discussed in the thesis, this model is worth developing due to its advantages toward computing the arc fringe region, as shown in the literature using a two-temperature model [16,68]. Once this model is successfully used for a cutting process without numerical instability, a simulation can be developed that will be more reasonable with regard to the plasma region modeling.

Chapter 8

Conclusions

8.1. Summary

Due to its various advantages, plasma arc cutting is widely used, and considerable research has been done on it. The two very important parts of plasma arc cutting are the plasma nozzle and the cut slot (kerf), and research has focused on these two areas through experimental and numerical work. From an industrial point of view, the kerf is an especially important region to explore in order to improve cut quality and cut speed. Additionally, the physical phenomena near the anode region on the kerf are still not well understood. Therefore, the need for kerf research has been emphasized, but previous studies have been limited. Because of the complex physical phenomena and closed geometry involved in a kerf, it is very hard to conduct experimental research. Existing numerical research is also limited for analyzing plasma arc cutting due to the relative lack of research on the kerf. The complexity of the physical phenomena of this region requires an alternative method that can compensate for the limitations of previous research. Computational Fluid Dynamics and Heat Transfer (CFDHT) methods are one possible solution for study of the kerf region.

It is necessary to analyze physical phenomena to develop a model by CFDHT methods. The plasma arc cutting process melts the work piece and blows away the molten metal by using a high temperature thermal plasma and the drag force of the high speed gas. This process consists of a complex system of three phases: plasma gas, molten metal, and solid metal. Therefore, it is necessary to simplify specific physical phenomena in order to build a model. To be simple, the physical phenomena are broken down into three phenomena. The first phenomenon is the phase change of solid metal that is melted by heat from the plasma arc. The second one is the two-phase flow between plasma and molten metal. The third phenomenon is the plasma flow.

First, in order to develop a model for the cutting process near the kerf, an enthalpy-porosity method for melting and a Volume of Fluid (VoF) method for capturing the interface between plasma flow and molten metal are used, and LTE and two-temperature plasma models were considered for the plasma flow. After each sub-model was developed and validated, a cutting process model was obtained by a combination of models.

The plasma properties for the working gas, oxygen, were calculated using gas kinetics and statistical mechanics that considered LTE and a two-temperature assumption [68]. For the metal phase, constant properties were considered for the model simplification. The combined properties in the computational cell were calculated based on the volume fraction of each phase (plasma gas, molten metal, and solid metal).

In addition, the cutting process modeling was implemented in open-source CFD software, OpenFOAM (Open Source Field Operation and Manipulation) to run the

cutting process simulation. The governing equations for the cutting process were easily included in the solver for fluid flow due to a relatively easy code structure based on C++. Additionally, OpenFOAM has several pre/post-processing functions and solvers, and thus, this allows one to accelerate solver development. Lastly, parallelization can be used for the simulation. This is a great advantage for the present work because the plasma flow requires extremely small time steps, ten to the negative eighth power in seconds, and this is computationally very expensive.

Simulation was conducted for the geometry and included from the plasma torch to the bottom of the work piece. A simulation with a fine mesh was selected to examine the results for dependent variables. In order to create a more reasonable simulation that is closer to reality, different operation conditions and models for plasma physics were investigated. These included: 1) mesh size, 2) swirl component, 3) inclusion of metal vapor, 4) chemistry in melt (exothermic reaction and change in metal properties), and 5) the Darcy term in a phase change model. Not all were addressed by computation in this thesis.

8.2. Conclusion

The simulation of the plasma cutting process from the plasma torch to the bottom of the work piece was successfully conducted. The simulation results include the physical phenomena for melting of the work piece as well as the plasma flow, the model can be very useful to understand the physics involved with the cutting process. The results of the kerf shape show that the melting is too fast at the upper portion of the work piece and the kerf is relatively wider than the measured kerf under the same operational conditions.

Also, the ratio of the required power to the total power is higher than values in the literature. These results indicate that more energy is transferred to the work piece compared to the actual cutting process. With a fast melting rate, the unstable electric arc near the anode region is another issue in the simulation. Due to the unstable arc inside the torch, presumed to be by kink instability, there is a moving arc attachment on the work piece, which is not physically correct. Temperature, velocity, and current density distributions are influenced by the unstable arc.

In order to produce a more reasonable kerf shape, firstly, the swirl component of the plasma gas is studied. High swirl components result in high circumferential velocities for the same mass flow rate, making it possible to constrict the electric arc and the plasma flow. A swirl angle of 60 degrees is chosen as a comparison case to one with 20 degrees. Initially, a high swirl component seemed to improve arc stability. However, it did not entirely resolve the arc instability problem, and an unstable arc has still been observed.

The oxidation model isn't applied in the present work due to the complexity of oxidation modeling, but the surface tension force affected by oxidation has been investigated. Oxidation reaction releases heat by exothermic reaction, and generates iron oxide. This iron oxide has different properties from the iron. It helps to remove the molten metal by its effect on surface tension. The surface tension coefficient of iron oxide has been used to compare to the surface tension coefficient of the iron. The results of the surface tension coefficient of the iron oxide show that small particles of molten metal are observed near the work piece for cases with low surface tension coefficients. This indicates that the iron oxide has the advantage to detach the molten metal from the

surface of the work piece. However, the low surface tension coefficient can't significantly change the kerf shape. Results show the same trend for low and high surface tension coefficients.

Lastly, a large constant value of C (Darcy coefficient) to regulate the flow of the solid fraction has been studied. It represents control over the resistance to flow. The result using higher constant values shows that the melting rate is reduced compared to cases with lower constant values. However, enhanced melting of the upper region is still physically unreasonable. This indicates that the high melting rate of the upper region is mainly affected by the plasma model. However, the influence of the Darcy term can't be neglected, and thus, it is important to choose optimum values for the continued work.

Although the kerf shape doesn't match the measured kerf shape, this work is a first attempt at simulation including plasma flow, melting, and molten metal flow in the plasma arc cutting process. As the model approaches physical reality, it gives increasingly stronger insight into the physical relationships among operating conditions, providing very helpful directions to improve the performance of plasma arc cutting, and providing useful data in designing the plasma arc cutting process.

8.3. Recommendations for Future work

8.3.1. Metal vapor

As discussed in Chapter 7, the inclusion of metal vapor influences the simulation results by decreasing the heat flux to the work piece. In order to include metal vapor in the present model, this model needs the species transport equation for metal vapor. For

this equation, proper diffusion coefficients are required to consider the diffusion of the plasma gas and metal vapor. Additionally, the source term of emitted metal vapor is also needed. Metal vapor is generated in the anode region by the electric arc and, thus, the generation of metal vapor in this region should be captured in the model. This is quite difficult, however, because the region of emitted metal vapor is placed in the middle of the computational domain of the present analysis. The gradient of volume fraction between plasma gas and metal phase should be used for this model. Including metal vapor in the cutting model should provide a more accurate computation of the kerf shape.

8.3.2. Oxidation reaction

Oxidation is an important physical phenomena in plasma cutting using oxygen as the working gas. This gives additional heat to the melt front, and it changes the metal properties on the surface of the work piece, and the cut results. Several considerations are necessary in order to include oxidation reactions. First of all, a heat source should be included on the surface of the work piece. In addition, properties used in all aspects of the oxidation model need also to be considered. In the present work, the influence of the surface tension coefficient of the iron oxide was investigated, and the results are quite similar, except for slight differences in the molten metal behavior on the surface. However, in order to develop a more accurate model, the simulation should be run for longer periods of time than the runs presented in this thesis, with the gradient of surface tension driving the flow as described by the thermal Marangoni effect.

8.3.3. Two-temperature model

Due to problems related to the assumed electron temperature equation of the metal phase, completed simulation results for the cutting process model with the two-temperature model were not discussed in this thesis. However, the two-temperautre model has advantages for the arc fringe region, as shown in the literature. In order to use the two-temperature model, it is important to apply the assumptions related to electron flow in the work piece. This is an artificial construct that is required to run the simulation with the two-temperature model. It is expected that the simulation would be more true to the actual cutting process is successfully implemented.

8.3.4. Improved boundary conditions and sheath effects

The reality of thermal plasma physics is quite difficult, and thus, simplifying assumptions have been applied to the model in order to numerically stabilize the simulation of the plasma process. In the present work, an unstable arc was observed in the plasma torch, which also influences the arc attachment region on the work piece. It is thought that this is a sort of kink instability affected by the induced-magnetic field surrounding the electric arc. Therefore, exact boundary conditions would be required to obtain more realistic arc modeling. Moreover, simplifying assumptions for the sheath effects should be applied to the electrode regions. Sheath regions are thin layers with extremely high temperature gradients, and quasi-neutrality is not applied inside sheath regions. Thus, it is very difficult to capture their accurate physics without assumptions due to the very thin region. These assumptions may affect arc stability. Therefore, for

implementation of the two-temperature model, it is necessary to include a realistic model for the sheath effects.

References

[1] Boulos M I, Fauchais P and Pfender E 2013 *Thermal plasmas: fundamentals and applications* (New York: Plenum Press)

[2] Hypertherm Inc. http://www.hypertherm.com

[3] Peters J, Bartlett B, Lindsay J and Heberlein J 2008 Relating Spectroscopic Measurements in a Plasma Cutting Torch to Cutting Performance *Plasma Chem. Plasma Process.* **28** 331–52

[4] Ramakrishnan S, Shrinet V, Polivka F B, Kearney T N and Koltun P 2000 Influence of gas composition on plasma arc cutting of mild steel *J. Phys. D. Appl. Phys.* **33** 2288–99

[5] Freton P, Gonzalez J J, Peyret F C and Gleizes A 2003 Complementary experimental and theoretical approaches to the determination of the plasma characteristics in a cutting plasma torch *J. Phys. D. Appl. Phys.* **36** 1269–83

[6] Nemchinsky V a and Severance W S 2009 Plasma arc cutting: speed and cut quality *J. Phys. D. Appl. Phys.* **42** 195204

[7] Gage R M 1957 Patent No. 2806124.

[8] Nemchinsky V A and Severance W S 2006 What we know and what we do not know about plasma arc cutting *J. Phys. D. Appl. Phys.* **39** R423

[9] Gleizes A, Gonzalez J J and Freton P 2005 Thermal plasma modelling *J. Phys. D. Appl. Phys.* **38** R153–83

[10] Ferziger J H and Peric M 2012 *Computational methods for fluid dynamics* (Springer Science & Business Media)

[11] Devoto R S 1966 Transport Properties of Ionized Monatomic Gases *Phys. Fluids* **9** 1230

[12] Devoto R S 1967 Transport Coefficients of Partially Ionized Argon *Phys. Fluids* **10** 354

[13] Devoto R S 1967 Simplified Expressions for the Transport Properties of Ionized Monatomic Gases *Phys. Fluids* **10** 2105

[14] Hsu K C, Etemadi K and Pfender E 1983 Study of the free-burning high-intensity argon arc *J. Appl. Phys.* **54** 1293

[15] Hsu K C and Pfender E 1983 Two-temperature modeling of the free-burning, high-intensity arc *J. Appl. Phys.* **54** 4359

[16] Trelles J P, Heberlein J V R and Pfender E 2007 Non-equilibrium modelling of arc plasma torches *J. Phys. D. Appl. Phys.* **40** 5937–52

[17] Heberlein J and Murphy A B 2008 Thermal plasma waste treatment *J. Phys. D. Appl. Phys.* **41** 053001

[18] Trelles J P and Modirkhazeni S M 2014 Variational multiscale method for nonequilibrium plasma flows *Comput. Methods Appl. Mech. Eng.* **282** 87–131

[19] Trelles J P 2013 Computational study of flow dynamics from a dc arc plasma jet *J. Phys. D. Appl. Phys.* **46** 255201

[20] Freton P, Gonzalez J J, Ranarijaona Z and Mougenot J 2012 Energy equation formulations for two-temperature modelling of "thermal" plasmas *J. Phys. D. Appl. Phys.* **45** 465206

[21] Boselli M, Colombo V, Ghedini E, Gherardi M and Sanibondi P 2013 Two-temperature modelling and optical emission spectroscopy of a constant current plasma arc welding process *J. Phys. D. Appl. Phys.* **46** 224009

[22] Baeva M, Kozakov R, Gorchakov S and Uhrlandt D 2012 Two-temperature chemically non-equilibrium modelling of transferred arcs *Plasma Sources Sci. Technol.* **21** 055027

[23] Ghorui S, Heberlein J V R and Pfender E 2007 Thermodynamic and Transport Properties of Two-temperature Oxygen Plasmas *Plasma Chem. Plasma Process.* **27** 267–91

[24] Park J, Heberlein J, Pfender E, Candler G and Chang C H 2008 Two-dimensional numerical modeling of direct-current electric arcs in nonequilibrium *Plasma Chem. Plasma Process.* **28** 213–31

[25] Ghorui S, Heberlein J V R and Pfender E 2007 Non-equilibrium modelling of an oxygen-plasma cutting torch *J. Phys. D. Appl. Phys.* **40** 1966–76

[26] Lowke J J, Morrow R and Haidar J 1997 A simplified unified theory of arcs and their electrodes *J. Phys. D. Appl. Phys.* **30** 2033–42

[27] Sansonnens L, Haidar J and Lowke J J 2000 Prediction of properties of free burning arcs including effects of ambipolar diffusion *J. Phys. D. Appl. Phys.* **33** 148–57

[28] Tanaka M, Terasaki H, Ushio M and Lowke J J 2002 A unified numerical modeling of stationary tungsten-inert-gas welding process *Metall. Mater. Trans. A* **33** 2043–52

[29] Tanaka M and Lowke J J 2007 Predictions of weld pool profiles using plasma physics *J. Phys. D. Appl. Phys.* **40** R1–23

[30] Lowke J J and Tanaka M 2006 "LTE-diffusion approximation" for arc calculations *J. Phys. D. Appl. Phys.* **39** 3634–43

[31] Trelles J P, Heberlein J V R and Pfender E 2008 The Reattachment Process in Nonequilibrium Arc Simulations *IEEE Trans. Plasma Sci.* **36** 1024–5

[32] Lago F, Gonzalez J J, Freton P and Gleizes a 2004 A numerical modelling of an electric arc and its interaction with the anode: Part I. The two-dimensional model *J. Phys. D. Appl. Phys.* **37** 883–97

[33] Nemchinsky V a and Severance W S 2006 What we know and what we do not know about plasma arc cutting *J. Phys. D. Appl. Phys.* **39** R423–38

[34] Nemchinsky V A 1997 Dross formation and heat transfer during plasma arc cutting *J. Phys. D. Appl. Phys.* **30** 2566–72

[35] Teulet P, Girard L, Razafinimanana M, Gleizes a, Bertrand P, Camy-Peyret F, Baillot E and Richard F 2006 Experimental study of an oxygen plasma cutting torch: II. Arc–material interaction, energy transfer and anode attachment *J. Phys. D. Appl. Phys.* **39** 1557–73

[36] Ramakrishnan S, Gershenzon M, Polivka F, Kearney T N and Rogozinski M W 1997 Plasma generation for the plasma cutting process *IEEE Trans. Plasma Sci.* **25** 937–46

[37] Ramakrishnan S and Rogozinski M W 1997 Properties of electric arc plasma for metal cutting *J. Phys. D. Appl. Phys.* **30** 636–44

[38] Pardo C, González-Aguilar J, Rodríguez-Yunta A and Calderón M A G 1999 Spectroscopic analysis of an air plasma cutting torch *J. Phys. D. Appl. Phys.* **32** 2181–9

[39] Girard L, Teulet P, Razafinimanana M, Gleizes A, Camy-Peyret F, Baillot E and Richard F 2006 Experimental study of an oxygen plasma cutting torch: I. Spectroscopic analysis of the plasma jet *J. Phys. D. Appl. Phys.* **39** 1543–56

[40] Peters J, Heberlein J and Lindsay J 2007 Spectroscopic diagnostics in a highly constricted oxygen arc *J. Phys. D. Appl. Phys.* **40** 3960–71

[41] Colombo V, Concetti A, Ghedini E, Dallavalle S and Vancini M 2009 High-speed imaging in plasma arc cutting: a review and new developments *Plasma Sources Sci. Technol.* **18** 023001

[42] Boselli M, Colombo V, Ghedini E, Gherardi M, Rotundo F and Sanibondi P 2013 High-speed imaging investigation of transient phenomena impacting plasma arc cutting process optimization *J. Phys. D. Appl. Phys.* **46** 224010

[43] Bemis B L and Settles G S 1998 Visualization of Liquid Metal , Arc , and Jet Interactions in Plasma Cutting of Steel Sheet 1–9

[44] Bemis B L and Settles G S 1999 Ultraviolet imaging of the anode attachment in transferred-arc plasma cutting *IEEE Trans. Plasma Sci.* **27** 44–5

[45] Colombo V, Concetti A, Ghedini E, Rotundo F, Sanibondi P, Boselli M, Dallavalle S, Gherardi M, Nemchinsky V and Vancini M 2012 Advances in plasma arc cutting technology: The experimental part of an integrated approach *Plasma Chemistry and Plasma Processing* vol 32 pp 411–26

[46] André P, Bussière W and Rochette D 2007 Transport Coefficients of Ag–SiO2 Plasmas *Plasma Chem. Plasma Process.* **27** 381–403

[47] Kim S, Heberlein J, Lindsay J and Peters J 2011 Torch Design Modification Using Micro-jets to Suppress Fluid Dynamic Instabilities in Plasma Arc Cutting *Plasma Chem. Plasma Process.* **32** 45–63

[48] Gonzalez-Aguilar J, Sanjurjo C P, Rodriguez-Yunta a. and Calderon M a. G 1999 A theoretical study of a cutting air plasma torch *IEEE Trans. Plasma Sci.* **27**

[49] Freton P, Gonzalez J J, Gleizes A, Peyret F C, Caillibotte G and Delzenne M 2002 Numerical and experimental study of a plasma cutting torch *J. Phys. D. Appl. Phys.* **35** 115–31

[50] Colombo V, Concetti A, Ghedini E, Dallavalle S and Vancini M 2008 Understanding Plasma Fluid Dynamics Inside Plasma Torches Through Advanced Modeling *IEEE Trans. Plasma Sci.* **36** 389–402

[51] Zhou Q, Yin H, Li H, Xu X, Liu F, Guo S, Chang X, Guo W and Xu P 2009 The effect of plasma-gas swirl flow on a highly constricted plasma cutting arc *J. Phys. D. Appl. Phys.* **42** 095208

[52] Nguyen Phi Long, Tanaka Y and Uesugi Y 2012 Numerical investigation of the swirl gas angle and arc current dependence on evaporation of hafnium cathode in a plasma cutting arc *IEEE Trans. Plasma Sci.* **40** 497–504

[53] Long N P, Tanaka Y, Uesugi Y and Yamaguchi Y 2013 Numerical investigation of the effect of cathode holder shape on hafnium cathode evaporation for an oxygen plasma cutting arc *J. Phys. D. Appl. Phys.* **46** 224012

[54] Kheloufi K, Hachemi Amara E and Benzaoui A 2015 Numerical Simulation of Transient Three-Dimensional Temperature and Kerf Formation in Laser Fusion Cutting *J. Heat Transfer* **137** 112101

[55] Hu J and Tsai H L 2007 Heat and mass transfer in gas metal arc welding. Part I: The arc *Int. J. Heat Mass Transf.* **50** 833–46

[56] Cho J-H and Na S-J 2006 Implementation of real-time multiple reflection and Fresnel absorption of laser beam in keyhole *J. Phys. D. Appl. Phys.* **39** 5372–8

[57] Bachmann M, Avilov V, Gumenyuk A and Rethmeier M 2012 Numerical simulation of full-penetration laser beam welding of thick aluminium plates with inductive support *J. Phys. D. Appl. Phys.* **45** 035201

[58] Voller V R and Prakash C 1987 A fixed grid numerical modelling methodology for convection-diffusion mushy region phase-change problems *Int. J. Heat Mass Transf.* **30** 1709–19

[59] Voller V R, Swaminathan C R and Thomas B G 1990 Fixed grid techniques for phase change problems: A review *Int. J. Numer. Methods Eng.* **30** 875–98

[60] Murphy A B 2011 A self-consistent three-dimensional model of the arc, electrode and weld pool in gas–metal arc welding *J. Phys. D. Appl. Phys.* **44** 194009

[61] Murphy A B 2013 Influence of metal vapour on arc temperatures in gas–metal arc welding: convection versus radiation *J. Phys. D. Appl. Phys.* **46** 224004

[62] Hirt C . and Nichols B . 1981 Volume of fluid (VOF) method for the dynamics of free boundaries *J. Comput. Phys.* **39** 201–25

[63] Kim J W and Na S J 1995 A study on the effect of contract tube-to-workpiece distance on weld pool shape in gas metal arc welding *Weld. J.* **74**

[64] Wu C S, Chen J and Zhang Y M 2007 Numerical analysis of both front- and back-side deformation of fully-penetrated GTAW weld pool surfaces *Comput. Mater. Sci.* **39** 635–42

[65] Otto A, Koch H, Leitz K-H and Schmidt M 2011 Numerical Simulations - A Versatile Approach for Better Understanding Dynamics in Laser Material Processing *Phys. Procedia* **12** 11–20

[66] Brent A D, Voller V R and Reid K J 1988 ENTHALPY-POROSITY TECHNIQUE FOR MODELING CONVECTION-DIFFUSION PHASE CHANGE: APPLICATION TO THE MELTING OF A PURE METAL *Numer. Heat Transf.* **13** 297–318

[67] Jenista J, Takana H, Nishiyama H, Krenek P, Bartlova M and Aubrecht V 2014 Quasi-Laminar Flow Characteristics in Hybrid-Stabilized Argon–Water Arc Discharge for Subsonic-Supersonic Regimes *IEEE Trans. Plasma Sci.* **42** 2632–3

[68] Osterhouse D 2014 *Numerical Modeling of the Work Piece Region in the Plasma Arc Cutting Process* (University of Minnesota)

[69] Lowke J J 1974 Predictions of arc temperature profiles using approximate emission coefficients for radiation losses *J. Quant. Spectrosc. Radiat. Transf.* **14** 111–22

[70] Naghizadeh-Kashani Y, Cressault Y and Gleizes A 2002 Net emission coefficient of air thermal plasmas *J. Phys. D. Appl. Phys.* **35** 2925–34

[71] Rusche H 2002 *Computational Fluid Dynamics of Dispersed Two-Phase Flows at High Phase Fractions* (Imperial College, University of London)

[72] Osher S, Fedkiw R and Piechor K 2004 Level Set Methods and Dynamic Implicit Surfaces *Appl. Mech. Rev.* **57** B15

[73] OpenFoam 2015 User Guide http://www.openfoam.org/docs/

[74] Berberović E, Van Hinsberg N P, Jakirlić S, Roisman I V. and Tropea C 2009 Drop impact onto a liquid layer of finite thickness: Dynamics of the cavity evolution *Phys. Rev. E - Stat. Nonlinear, Soft Matter Phys.* **79**

[75] Deshpande S S, Anumolu L and Trujillo M F 2012 Evaluating the performance of the two-phase flow solver interFoam *Comput. Sci. Discov.* **5** 014016

[76] Brackbill J ., Kothe D . and Zemach C 1992 A continuum method for modeling surface tension *J. Comput. Phys.* **100** 335–54

[77] Voller V R, Cross M and Markatos N C 1987 An enthalpy method for convection/diffusion phase change *Int. J. Numer. Methods Eng.* **24** 271–84

[78] Rösler F and Brüggemann D 2011 Shell-and-tube type latent heat thermal energy storage: numerical analysis and comparison with experiments *Heat Mass Transf.* **47** 1027–33

[79] Ivarson a., Powell J, Kamalu J and Magnusson C 1994 The oxidation dynamics of laser cutting of mild steel and the generation of striations on the cut edge *J. Mater. Process. Technol.* **40** 359–74

[80] White F M 2006 *Viscous fluid flow* vol 3 (McGraw-Hill New York)

[81] Versteeg H K and Malalasekera W 2007 *An introduction to computational fluid dynamics: the finite volume method* (Pearson Education)

[82] Jasak H 1996 *Error Analysis and Estimation for the Finite Volume Method with Applications to Fluid Flows* (Imperial College, University of London)

[83] Sweby P K 1984 High Resolution Schemes Using Flux Limiters for Hyperbolic Conservation Laws *SIAM J. Numer. Anal.* **21** 995–1011

[84] Saad Y 2011 *Numerical Methods for Large Eigenvalue Problems: Revised Edition* vol 66 (Siam)

[85] Patankar S 1980 *Numerical heat transfer and fluid flow* (CRC Press)

[86] Issa R . 1986 Solution of the implicitly discretised fluid flow equations by operator-splitting *J. Comput. Phys.* **62** 40–65

[87] Poinsot T . and Lelef S . 1992 Boundary conditions for direct simulations of compressible viscous flows *J. Comput. Phys.* **101** 104–29

[88] Osterhouse D J, Lindsay J W and Heberlein J V R 2013 Using arc voltage to locate the anode attachment in plasma arc cutting *J. Phys. D. Appl. Phys.* **46** 224013

[89] Mahajan M S 2010 *Numerical modeling of plasma cutting torches.* (University of Minnesota)

[90] Zhou X and Heberlein J 1998 An experimental investigation of factors affecting arc-cathode erosion *J. Phys. D. Appl. Phys.* **31** 2577–90

[91] Gau C and Viskanta R 1986 Melting and Solidification of a Pure Metal on a Vertical Wall *J. Heat Transfer* **108** 174

[92] Murphy A B 2010 The effects of metal vapour in arc welding *J. Phys. D. Appl. Phys.* **43** 434001

[93] Powell J, Petring D, Kumar R V., Al-Mashikhi S O, Kaplan A F H and Voisey K T 2009 Laser–oxygen cutting of mild steel: the thermodynamics of the oxidation reaction *J. Phys. D. Appl. Phys.* **42** 015504

[94] Martin C, Nemchinsky V A and Severance W S 2013 Measurements of power of oxidation reaction during plasma arc cutting of steel with an oxygen plasma *J. Phys. D. Appl. Phys.* **46** 224014

[95] Pal D and Joshi Y K 2001 Melting in a side heated tall enclosure by a uniformly dissipating heat source *Int. J. Heat Mass Transf.* **44** 375–87

[96] Shatikian V, Ziskind G and Letan R 2005 Numerical investigation of a PCM-based heat sink with internal fins *Int. J. Heat Mass Transf.* **48** 3689–706

[97] He X, Fuerschbach P W and DebRoy T 2003 Heat transfer and fluid flow during laser spot welding of 304 stainless steel *J. Phys. D. Appl. Phys.* **36** 1388–98

[98] Shmueli H, Ziskind G and Letan R 2010 Melting in a vertical cylindrical tube: Numerical investigation and comparison with experiments *Int. J. Heat Mass Transf.* **53** 4082–91